Structural and Field Emission Properties of Ion Beam Synthesized Metal-dielectric Nano-composite Thin Films

YUEN, Ying Kit

A Thesis Submitted in Partial Fulfillment

of the Requirements for the Degree of

Master of Philosophy

in

Electronic Engineering

Sept 2007

Abstract

In this work, Fe-SiO_2 and Co-SiO_2 nano-composite thin films were prepared by ion implantation using a metal vapor vacuum arc (MEVVA) ion source. Various doses of Fe and Co were implanted into 100nm-thick SiO_2 films at an extraction voltage of 30kV. The extraction voltage was chosen after TRIM simulation so that the implanted ions could penetrate the SiO_2 films to the Si substrate. Rapid thermal annealing (RTA) was performed at different temperatures. The samples were characterized by atomic force microscopy (AFM), conducting atomic force microscopy (C-AFM), Rutherford backscattering spectrometry (RBS). And field emission measurement which was carried out in the high vacuum with base pressure better than $2x10^{-8}$ Torr.

An ultra low turn-on field which was 0.17 V/μm and extremely large field enhancement was recorded in one of the annealed samples. The TEM micrographs of the Fe-SiO_2 samples showed that there were nano-size Fe clusters embedded inside the SiO_2 layer under the sample surface and a tranisition layer between the nano-composite thin film and the Si substrate. The micrographs also showed a surface morphology which was consistent with the AFM images. Furthermore, the Fe atoms moved towards to the surface of the samples and the transistion layer was widened as the annealing temperature increased.

Moreover, some unrepeatable step-like and jump-like features in *J-E* plots were found in both Fe and Co as-implanted as well as the annealed samples. On the other hand, the field emission projection intensity was photographically observed. It was found that the emission sites were highly localized and incoherent over the sample

surface. These implied that the field emission properties were modified during the field emission measurement. Two models were proposed, namely, the local-self-annealing and the formation of new conducting paths due to joule heating of field emission current during the field emission.

摘要

在此研究項目中，我們用金屬真空弧(MEVVA)離子注入技術並以三萬伏電壓把不同劑量的鈷或鐵原子注入到一百納米厚的二氧化硅膜，產生鈷—二氧化硅與鐵—二氧化硅，藉此研究金屬注入的電介質-金屬納米複合薄膜。TRIM 模擬計算顯示三萬伏電壓足以把鈷或鐵原子打穿並透入一百納米厚的二氧化硅膜，以確保樣品表面的金屬原子連接到二氧化硅下的硅晶襯底上。部份樣品在不同溫度的氬氣環境下進行了快速熱退火(RTA)以改變它們的場發射特性。這些樣品的場發射特性的研究結果則配合各種表徵技術，進而分析和研究，當中包括原子力顯微鏡(AFM)、導電原子力顯微鏡(C-AFM)及盧瑟福背向散射術(RBS)。而場發射實驗則在真空度不低於 $2x10^{-8}$ 毛的高真空環境下測量。

在其中一個經過退火的樣品中，我們發現它具有 0.17V/μm 的超低開啓電場(turn-on field)和極高的電場增強效應(field enhancement)。利用透射電子顯微鏡技術(TEM)，我們在鐵—二氧化硅的樣品中可以找到納米尺度的鐵類團簇和一層夾在納米複合薄膜與硅襯底中間的過渡層。從 TEM 相片中，發現樣品的表面形態與原子力顯微鏡圖片(AFM)所看見吻合。此外，這些鐵原子團簇會隨著退火的溫度增加而向上遷移，擴大了中間過渡層的厚度，從而導致場發射特性減弱。

而在所有樣品的 *J-E* 關系中發現了一些不重複的臺階和跳躍特性。另外，從場發射的電子束斑圖片中，我們發現在樣品的表面存在很多細小的場發射點，這些場發射點會隨著時間在不同的位置出現或消失。這暗示了樣品的場發射特性會隨著場發射測量的時間而不斷改變。爲此，我們提出了兩個模型，分別是區域性的自我退火(local self-annealing)及新導電通道的形成(formation of new conducting paths)，而它們的成因可能與場發射電流造成的焦耳熱有關。

Acknowledgment

This is a thesis that is dedicated to Prof. S. P. Wong.

All the ideas and experiments presented in this thesis were completed under the guidance of my supervisors, Professor S. P. Wong. I would like to express my deep, sincerest gratitude to him for his patient guidance, generous encouragement, encyclopedic ideas and suggestions throughout my study period.

Moreover, I would like to thanks Professor J. B. Xu for his support and guidance in my study period.

In addition, I would like to thank Dr. W. Y. Cheung, Dr. N. Ke and Mr. W. K. Chan of the Solid State Laboratory, the Department of Electronic Engineering, CUHK, for their valuable advices, suggestions and technical support in this project. Besides, I would like to thank Mr. Wang Hui and Dr. N. Ke for their assistance in preparation of the TEM samples, Mr. C. M. Yuen for the preparation of the pure cobalt film. I would also like to thank my labmates in the Solid State Laboratory for their help and discussion during these two years.

Table of Contents

List of Figure Captions

List of Table Captions

1.1 Introduction to Electron Field Emission

Electron field emission is a phenomenon of liberation of free electrons from a material surface under the presence of an electric field. These materials are usually metals which are rich of free electrons.

There are many kinds of electron emission mechanisms including thermionic emission, secondary emission, photoelectric emission and field emission which is also known as Fowler-Nordheim emission and all of them required an external energy source supplying energy for the liberation of free electrons. Among all the above mechanisms, only field emission could emit electrons without overcoming the material work function which is an energy barrier binding the electrons to the material surface.

Emission mechanism	**External energy source**
Thermionic emission	Heat (Thermal energy)
Secondary emission	Electron/Ionic bombardment
Photoelectric emission	Photons Absorption (Photoelectric Effect)
Field emission	Electric field

Table 1.1 Different electron emission mechanisms

The earliest electron emission device was the cathode ray tube (CRT) and these cathode rays were produced in vacuum glass tubes. In 1897, J. J. Thomson proposed these rays were composed of tiny particles which were negatively charged and those

particles were the fundamental parts inside in the atoms. The discovery of electrons made him be the Nobel Prize winner in 1906. The working principle of TV is similar to that of CRT.

Since CRT displays are so bulky and heavy, people would like to replace the CRT by other technologies in order to overcome the shortness in size and weight in traditional CRT displays. Therefore, in recent years, new display technologies such as liquid crystal displays (LCD), plasma displays as well as field emission displays (FED) have been invented. Both FED and CRT produce light by the bombardment of electrons onto the screen which is coated with phosphor for colourful display but instead of a single electron gun with scanning plates, the FED make use of an array structure and each colour pixel has its own field emitters. The array structure greatly reduces the size of FED compared with the traditional CRT as well as the FED has fewer dead pixels compared with LCD since the pixel works well even if 20% of the few emitters of that pixel fail.

Another application of field emission is the fabrication of high speed and high frequency vacuum microelectronic devices [1]. Because of the lattice scattering in solid, the maximum velocity of electrons is limited to ~$10^5 ms^{-1}$. This is far behind the speed of light which is equal to $3x10^8 ms^{-1}$. The limitation of the speed of electrons hinders the operation speed of an electronic device. On the contrary, the electrons emitted by electron field emission would travel through vacuum without lattice scattering. Therefore, the velocity of the emitted electrons could approach to speed of light. This raise the operation speed of the device and high frequency application would be possible. Electron field emission materials would be a potential candidate in these devices [2]. Either thermionic emission or field emission, which are regarded

as hot cathode and cold cathode, could apply to the vacuum devices but the versatility of cold cathode is better than that of hot cathode for two reasons. First, hot cathode is usually larger compared with cold cathode due to the presence of hot filament. Second, much energy is lost in the form of heat in hot cathode while cold cathode could operate at room temperature. Hence, cold cathode technology could boot the power efficiency and cut the size of the devices.

Because of the above applications, researchers made a lot of efforts in searching for new cold cathode materials which possessed better field emission properties such as lower turn on voltage and larger field enhancement factor. Apart from the emission performance, researchers were also looking for new substances which could be susceptible for intensive electron emission such that the life of the emission devices could be lengthened. Diamond and diamond film [3-4], amorphous carbon layers [5-11], nanotubes [12-13], silicon carbide layers [14-18] and nano-composite dielectric films [19-20] are all possible candidates for the next generation of FEDs and high speed microelectronic devices. Intensive works are made on FEDs in order to fulfill the potential market of flat panel displays. In 1999, the estimated value of the global market for flat panel displays was $18.5 billions U.S. dollars [21] and it is predicted that the market would expand to about $70 billions dollars in the year of 2010.

1.2 Theory of Electron Field Emission

Electron field emission is a phenomenon of quantum mechanics. It is the emission of electrons from a material surface due to the presence of an intensive electric field. The emitted electrons obtain energy from the external applied electric field and tunnel through the potential barrier near the material surface and reach the anode.

The early research on electron field emission was done by Fowler and Nordheim in 1928 [22]. They derived an equation known as Fowler Nordheim Equation which successfully connected the field emission current density and the applied electric field strength for planar field emission of metals. This model is named as Fowler Nordheim model for electron field emission in metals and will be discussed in the next section.

1.3 Fowler Nordheim Model for Electron Field Emission in Metals

Three assumptions are made in the Fowler Nordheim model (F-N model) [22].

- The electrons tunnel through a triangular potential barrier at a constant energy E
- The metal surface is perfectly smooth
- The emission occurs at absolute zero (temperature = 0K)

The following picture describes the band energy diagram of electron field emission.

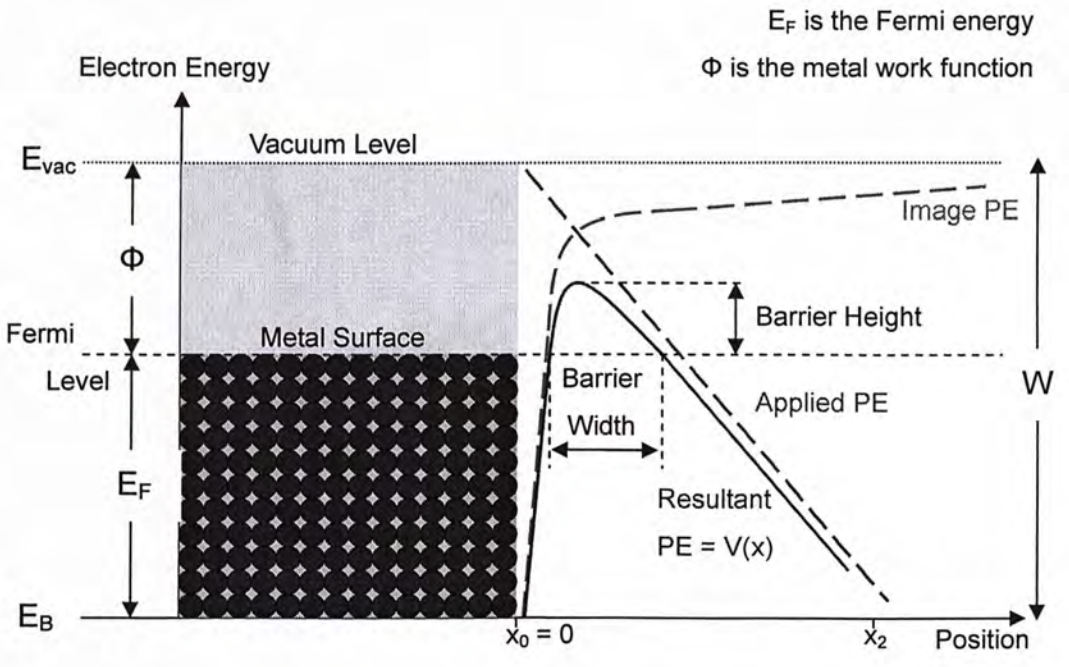

Figure 1.1 Band diagram of electron field emission

The resultant Potential Energy (PE) seen by the electrons inside the metal is the sum of the applied PE, which comes from the external applied electric field, and the image PE. In classical theory, electrons should not come out from the metal surface because none of them have enough energy to overcome the potential barrier while in

quantum theory, electrons could penetrate the potential barrier and it is known as electron tunneling. Therefore, Fowler and Nordheim manipulated the Schrödinger equation in the derivation of Fowler Nordheim equation (F-N equation). More details can be found in Appendix.

Before the electron field emission occurs, the sample behaves like a diode and the measured current is the leakage current which slightly increases with the applied voltage. The following picture is a typical *F-N* plot. Only the high field region represents the electron field emission.

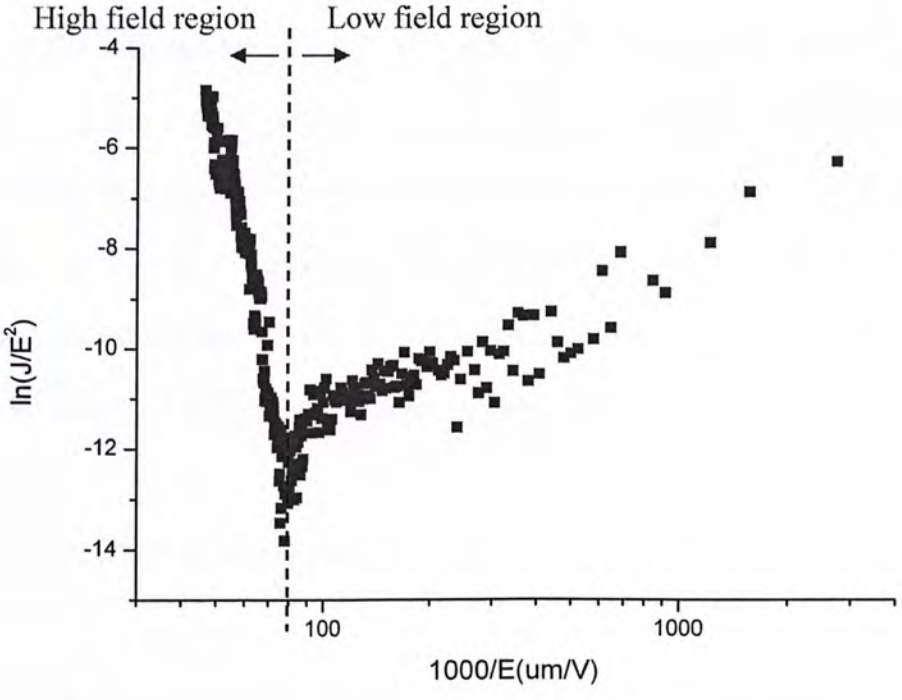

Figure 1.2 A typical *F-N* plot showing the low field and high field electron current

1.4 Factors Affecting the Field Emission Properties

In the field emission properties of metal dielectric composite, it is slightly different from the electron emission of metal described in the F-N model. There are two mechanisms which play important roles and contribute to the field enhancement. They are the surface morphology and the electrical inhomogeneity [17-20].

1.4.1 Surface Morphology

Surface morphology is a key factor affecting the field emission performance. One of the assumptions in the F-N model required a perfectly smooth surface, but introducing many small protrusions to the emission surface could possibly lead to a field emission enhancement. This is because the charge density is much higher at the abrupt regions and this gives a higher probability in electron emission at the small protrusions on the emission surface. The surface morphology could be modified by thermal treatment such as rapid thermal annealing (RTA).

1.4.2 Electrical Inhomogeneity

After ion implantation, the implanted atoms would be embedded in the dielectric layer and this embedded conducting metal clusters are responsible for the second field enhancement which is known as electrical inhomogeneity. After applying an external electric field on the emission surface, the electric field lines would concentrate on those conducting area and results in a local field enhancement as shown in Figure 1.3.

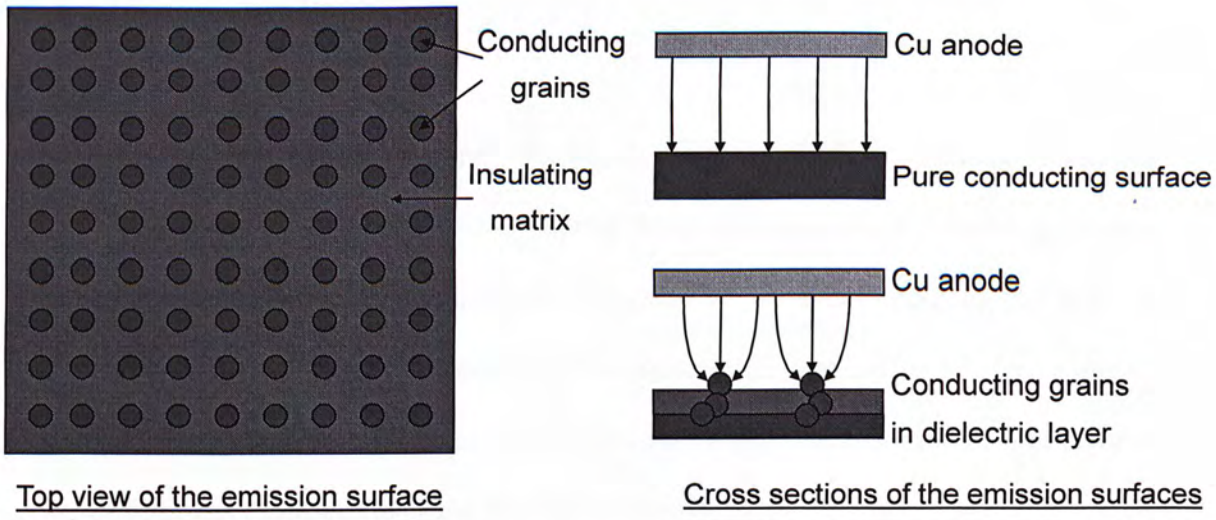

Figure 1.3 Local field enhancement by electrical inhomogeneity

1.5 Goal of this Project

In the past few years, the investigations on cold field emission materials including carbon containing thin films, nanotubes as well as metal dielectric nanocomposite thin films have been continuing to be a hot topic in the field of material science. Despite of searching for a materials system which has a lower turn-on field, the field enhancement mechanisms behind the emission of electrons in these different kinds of materials are still debatable.

In electron field emission, the field enhancement factor β is not only governed by only surface morphology. Instead, it also depends on the internal structure such as micro-inclusions, changes in chemical bonding and grain boundary structures [27]. Therefore, there are many studies on different kinds of materials. In 1980s, the majority focused on amorphous carbon films. It is found that the hybridization of the carbon film would affect the turn-on field and the field emission properties [28-30]. Therefore, researchers moved on to study the diamond like carbon films [31] and more complex alloys such as some metal doped hydrogenated amorphous carbon film [32-33].

After the mid-90s, the discovery of carbon nanotubes (CNTs) brought a new scenario on cold cathode materials [34-36] CNTs posses a very high aspect ratio and this gives rise to a low turn-on electric field and high field enhancement factor. A detailed investigation of the field emission properties of carbon nanotubes can be found in ref. [56]. In this paper, the field emission measurement was carried out using a 4mm spherical anode. The emission area was estimated to be about 250μm in diameter. A 1.75V/μm turn-on field was recorded for 1nA emission current. However,

mass production of carbon nanotubes with similar size and similar microstructure is still a major challenge in device application. This is because the hairy like nanotubes which is prepared by arc discharge techniques into triode structure will cause electrical short circuits between the cathode back contact and the gate electrode. In order to solve this problem, some researchers tried to grow the nanotubes with catalytic methods. Unfortunately, this approach required a high temperature and was not compatible with glass substrate for display application.

In our lab's previous work, the good field emission properties of tungsten implanted silicon carbide (W-SiC) [24] were attributed to the surface morphology, the electrical inhomogeneity and the formation of tungsten carbide. An embedded conducting grains (EGS) model was proposed in order to explain the local field enhancement the SiC system.

The goal of this project is to investigate the field emission properties of Fe and Co implanted SiO_2 thin films and study the events associated with the metal clusters inside the dielectric material. High quality SiO_2 thin film with controllable thickness can be easily prepared in laboratory. Moreover, SiO_2 is a versatile substrate material for ion implantation to create metal clustered thin films and their fabrication process is fully compatible with existing integrated circuit technology which is an advantage for device application. RTA was performed in order to modify the metal grain size and the surface morphology of the samples. It is believed that these two factors would have an important influence on the field emission performance. The last but not least, the field enhancement mechanisms of this kind of metal dielectric nano-composite structure was studied.

Chapter 2 Sample Preparation and Characterization Methods

2.1 Sample Preparation

In this project, n-type (100) 0.01-0.02Ωcm silicon wafers were used as substrates. These wafers were firstly cleaned by hydrofluoric acid (HF) which has a HF:H_2O ratio equaled to 1:50 in order to remove the native oxide on the surface of the wafers. The cleaned wafers then underwent dry oxidation at a temperature 1100°C for about 30mins with an oxygen flow rate equaled to 10cm^3/min. After the oxidation, a 100nm silicon dioxide (SiO_2) was grown on both sides of the silicon wafer. Next, the top surface of each wafer was coated with photo-resist using the spin coater and baked. They were then etched by HF solution again such the oxide layer on the back side of the wafer were removed. The photo-resist was then removed.

After the above preparation, the wafers could be placed into the chamber of the MEVVA ion implanter. Different doses of Fe or Co ions were implanted in to the SiO_2 layer at an extraction voltage of 30kV with a fixed beam current of 0.5mA. SRIM simulation was carried out to make sure this extraction voltage was high enough such that the implanted ions could penetrate through the SiO_2 layer. This was important for the field emission measurement so that the voltage could be applied to the sample surface by connecting the electrode to the Si substrate.

Moreover, some samples underwent rapid thermal annealing (RTA). Three annealing temperatures, 300°C, 400°C and 500°C, were chosen and the process was carried out in Ar ambient for 30sec.

The following section would describe the MEVVA ion implantation system and the implantation condition used in the project.

2.1.1 MEVVA Ion Implantation System

The technique of metal vapour vacuum arc (MEVVA) ion source was developed by Brown et al. [37] in 1985 at the Lawrence Berkeley Laboratory. Compared with the conventional ion implanter, the MEVVA ion source greatly increases the beam current from μA (10^{-6}A) order to mA (10^{-3}A) order. This shortens the implantation time a lot making the synthesis of thin films by ion implantation more practical. Figure 2.1 shows the schematic diagram of the MEVVA ion implantation system.

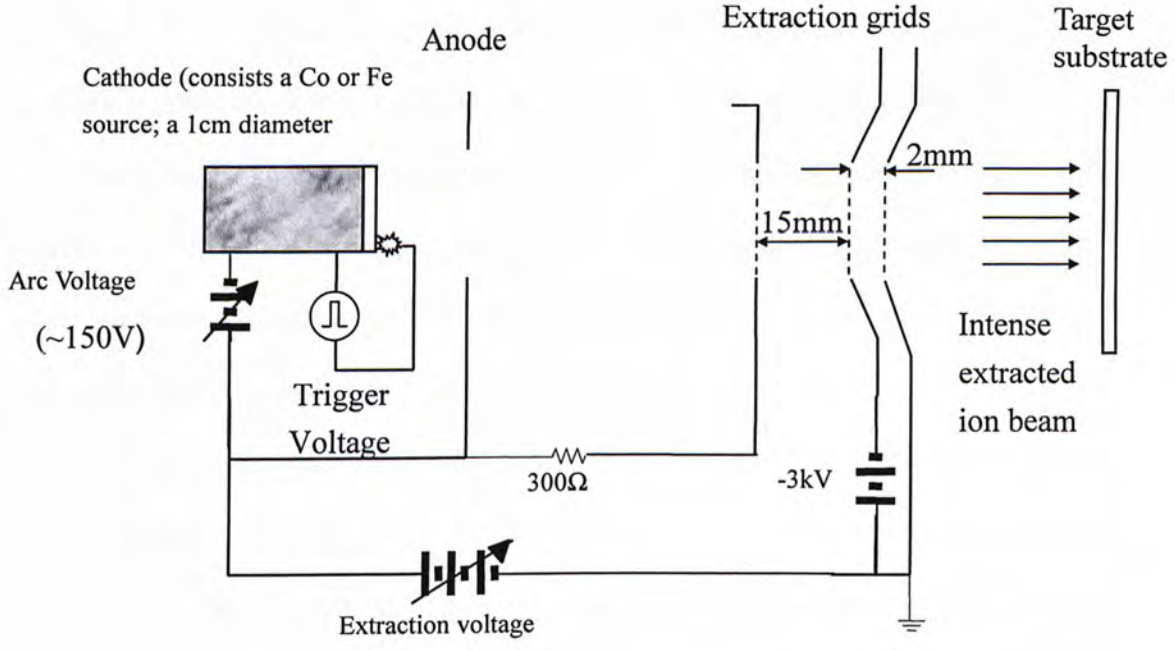

Figure 2.1 Schematic diagram of the MEVVA ion implantation system

There are three main basic components presents in an ion implantation system.

It includes an ion source, an acceleration system and a target station. The ion source is operated in a pulse mode with a pulse length fixed at 1.2 ms at a frequency of 1 to 25 Hz. During the ion implantation, a high voltage pulse of about 10 kV is applied between the trigger electrode and the cathode. This can induce a spark discharge and create a very high temperature. The cathode material is then vaporized and ionized. Dense plasma is thus formed at the surface of the cathode material. The formation of plasma is continued in the working triggering frequency. This quasi-neutral plasma traverses from the cathode towards the anode. This allows the arc current of 70 to 200 A to flow between the cathode and the anode at the arc voltage of 60 to 160 V. The quasi-neutral plasma then traverses to the extraction grids. In the acceleration system, a high voltage typically in the range of 35 to 80 kV is applied to the extraction grids in order to build up a high electric field for accelerating the positive ions inside the plasma. An intense ion beam including multiple charge states can be extracted. It should be noted that the extraction grids has many apertures to ensure a more uniform ion distribution of the intense ion beam. A negative suppression voltage of about –3kV relative to the target is supplied to the intermediate extraction grid for suppressing secondary electrons to avoid miscounting to the beam current. The outermost grid has ground potential. Furthermore, at the cathode source, there is a step motor which could push the source material forward at the trigger surface to replace those consumed. This feature allows a long and high dose implantation of the same type of source material without either replacing the cathode source or breaking the vacuum.

The generation of the intense ion beam mentioned above must proceed in a vacuum during the implantation. The vacuum system is composed of a molecular turbo pump and a mechanical pump. The base pressure is about 2 to 6×10^{-4}Pa. The

vacuum will be deteriorated after the formation of arc discharge. Upon the high averaged beam current and extraction voltage, heating effect on the target substrate will be observed. This provides a substrate heating effect with sharply rises and drops of temperature with the change in triggering pulse frequency. The substrate can be cooled by flowing liquid nitrogen to the substrate holder. Therefore, a range of working temperature from -200K to 800K can be provided for different implantation requirements.

MEVVA ion source is a versatile technique because it has several advantages over the traditional ion source. One of the favourite features is that almost all the metal elements in the periodic table can be manipulated by the MEVVA ion source. Non-metals which are conductive like carbon and silicon are also available for implantation [38-39]. This plasma generated by the sparking of the high trigger voltage contains ions with different charge states. For example, there exists Fe^{+} (25%), Fe^{2+} (68%) and Fe^{3+} (7%) in the Fe plasma and the average charge state is 1.82 [40]. These values are used for calculating the implanted dose and determine the desired extraction voltage by TRIM simulation.

There are other important features of the MEVVA ion implantation system. First of all, the ion beam is much broader compared with the conventional one. It can cover the whole four inches wafer directly and large uniformity can be achieved by the multi-aperture extraction grid. Moreover, the distance between the sample stage and the cathode source is about 80cm. The uniformity under this situation is determined to be within ±5%. Second, unlike conventional implanter, there is no mass analyzer inside the MEVVA system for selecting particular ion species with desired charge stage. Finally, the instantaneous input power density of the MEVVA system is very high for triggering the ion source.

2.1.2 TRIM Simulation

Before the implantation, TRIM simulation has to be carried out so as to get a rough idea on the distribution of the implanted ions as well as deciding the suitable accelerating voltage for a desirable implantation depth. The ion distribution inside an amorphous substrate C(z) is approximated by a symmetrical Gaussian distribution according to the LSS theory [41].

$$C(z) = \frac{D}{\sigma\sqrt{2\pi}} \exp\left[-\frac{(z-z_p)^2}{2\sigma^2}\right] \qquad (2.1)$$

D is the dose

z is the depth under the substrate surface

σ is the standard deviation from the mean

z_p is the projected range

The simulation program is called SRIM2000 [42] which employ the Monte Carlo Algorithm for the simulation of the ion distribution profile. Apart from the ion distribution, the program could also calculate the range and damage distribution as well as angular and energy distribution of those backscattered and transmitted ions in amorphous substrates.

The following two graphs (Figure 2.2 and 2.3) show the simulation results of Fe and Co implantation at an extraction voltage of 30kV. Assume the implanted dose is $1\times10^{17}cm^{-2}$. The results ensure that the implanted ions could penetrate the SiO_2 layer which is 100nm. The thickness of the SiO_2 layer is proven by ellipsometry. In fact, the remaining SiO_2 layer after the implantation would be less than 100nm due to sputtering.

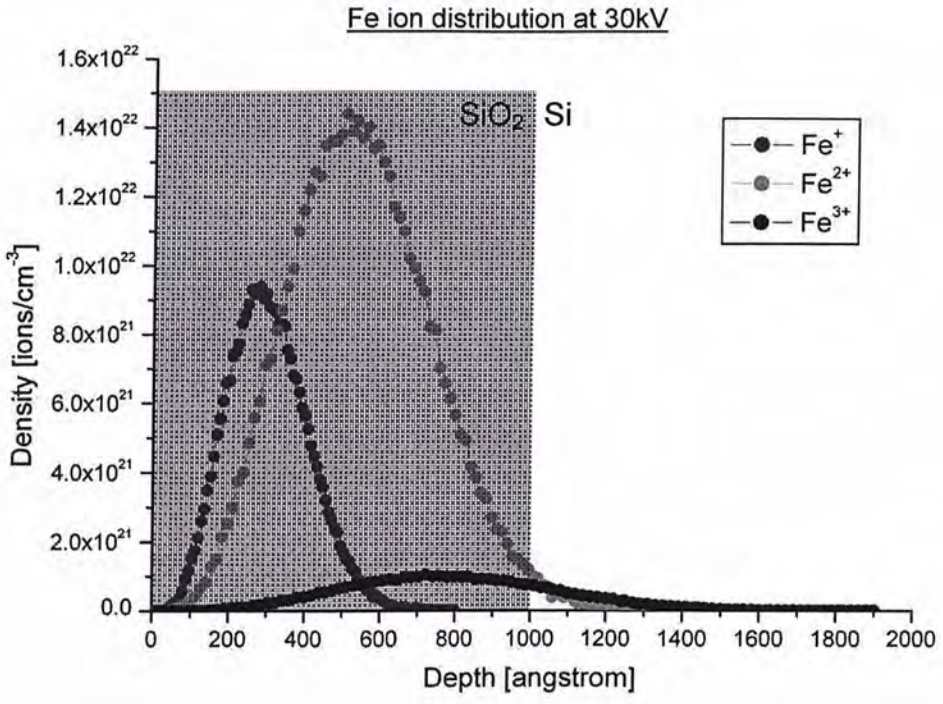

Figure 2.2 Ion distribution of Fe inside the substrate at 30kV implantation

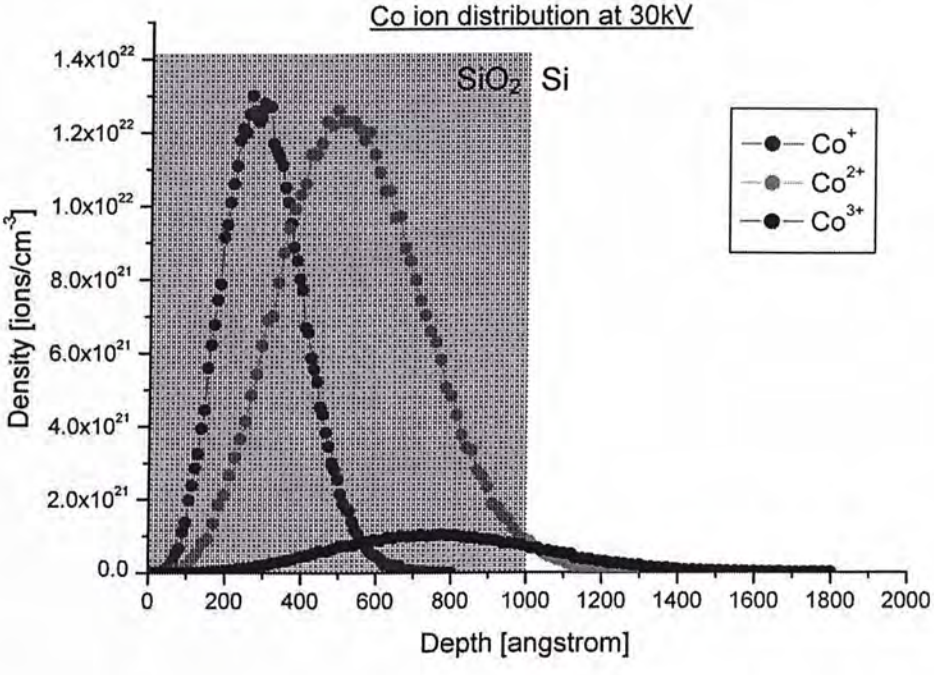

Figure 2.3 Ion distribution of Co inside the substrate at 30kV implantation

2.1.3 Implantation Conditions

There are several parameters determine the implantation result. These parameters are:

1. extraction voltage
2. total implanted dose
3. trigger voltage
4. trigger frequency
5. arc voltage

Adjusting the first two parameters, extraction voltage and total implanted dose, are intuitive. The trigger voltage, trigger frequency and arc voltage determine the beam current density. This beam current density also depends on the surface status of the cathode source. The table below shows the implantation conditions in this project.

Sample code	Dose (ions/cm^2)	Beam current (mA)	Extraction voltage (kV)	SiO_2 thickness
LD-Co	$1x10^{17}$	0.5	30	100nm
MD-Co	$2x10^{17}$	0.5	30	100nm
HD-Co	$3x10^{17}$	0.5	30	100nm
LD-Fe	$1x10^{17}$	0.5	30	100nm
MD-Fe	$2x10^{17}$	0.5	30	100nm
HD-Fe	$3x10^{17}$	0.5	30	100nm

Table 2.1 Summary of the implantation conditions

The implanted dose could be calculated from the total accumulated charge of ions (Q_{total}) which is counted by the charge integrator present in the MEVVA implantation system. The formula is [43]:

$$D = \frac{Q_{total}}{(1.6\times10^{-9})\bar{q}A} \qquad (2.2)$$

Q_{total} is the total accumulated charge of ions

A is the area of the ion beam which equals to $49\pi cm^2$

$\bar{q}$ is the average fractional charge state

2.2 Characterization Methods

There are two main factors controlling the field enhancement mechanism. They are the surface morphology and the electrical inhomogeneity which were studied by the atomic force microscopy (AFM) and conducting atomic force microscopy (CAFM) respectively. The retained dose after the implantation was determined by Rutherford backscattering spectrometry (RBS). The structure and phase of the nanocomposite were studied by x-ray diffraction (XRD) and transmission electron microscopy (TEM). The field emission properties of the samples were measured by a Hewlett Packard HP4339A high resistance meter at an high vacuum system with a base pressure better than 2×10^{-8}Torr.

2.2.1 AFM – Atomic Force Microscopy

Atomic force microscopy (AFM) is one of the extensions of scanning tunneling microscopy (STM) which was invented by Binning *et al.* in early 80's [44]. One of the weaknesses of STM is that it could only apply to conductive samples. Therefore, the Binning *et al.* developed the AFM in 1986 [45]. It overcomes the limitation of traditional STM as it can be applied to any types of materials including non-conducting materials.

The principle of AFM is based on the measurement between the interaction force between the surface atoms of sample and the atoms of the probe tip. More details can be found in reference [46]. Figure 2.4 shows the schematic of the AFM.

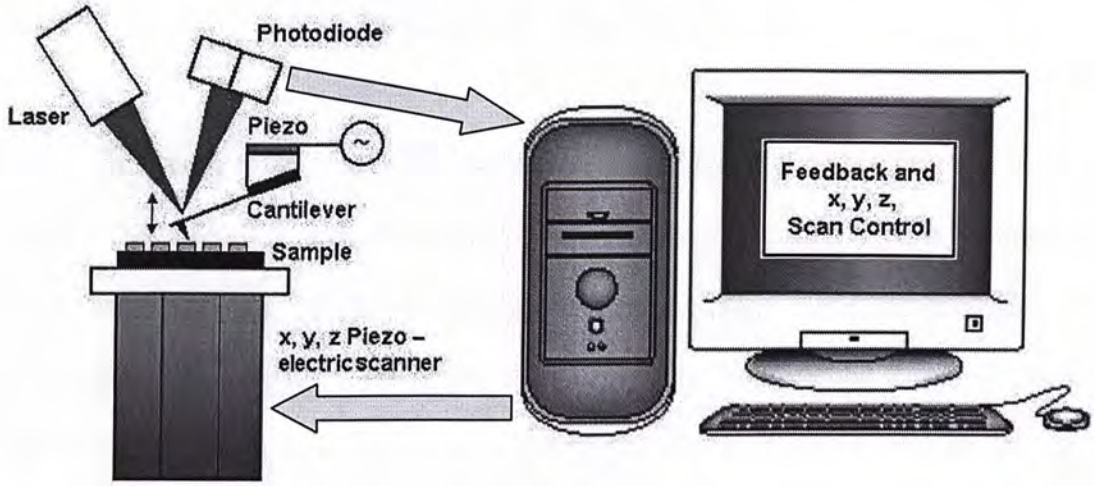

Figure 2.4 Schematic diagram of atomic force microscopy

The sample is mounted on an x, y, z piezoelectric scanner which is used to move the mounted sample in the x and y directions with a lateral resolution of about 1Å. A flexible cantilever which has a spring constant of about 0.1 – 10Nm^{-1} and a sharp tip at the end is fixed above the sample surface. On top of the cantilever, there is a laser diode emitting a laser beam. The beam is first reflected by the back side of the cantilever into a mirror and finally arrives at a position sensitive photodiode (PSPD) detector, as the tip is scanned over the sample surface. When there is any movement of the cantilever on the z-direction, the position of the laser beam at the PSPD detector will be shifted such that a vertical movement as small as 1Å could be detected. All the signals detected by the PSPD detector is transmitted to the computer and with further analysis, a surface morphologic image could be constructed.

2.2.2 C-AFM – Conducting Atomic Force Microscopy

In this project, the study of the electrical inhomogeneity of the samples is done by conducting atomic force microscopy (C-AFM). It is modified from a commercial AFM (Nanoscope III, Digital Instrument Inc.) with a home made preamplifier. The noise level of the preamplifier is less than 1.5pA. A commercial Si_3N_4 cantilever coated with 50nm TiN is used as a conducting probe. In C-AFM, a fixed DC bias voltage is applied across the tip of the probe and the sample. The separation between the tip and the sample surface is fixed by the feedback control of the computer and the currents flowing between the tip and the local regions of the sample are measured. A larger current will be measured at region with higher conductivity and vice versa. Finally, an image showing the local conductivity of the samples could be obtained.

2.2.3 RBS – Rutherford Backscattering Spectrometry

Rutherford backscattering spectrometry (RBS) is based on collisions between atomic nuclei and derives its name from Lord Ernest Rutherford, who in 1911 was the first to present the concept of atoms having nuclei. It involves measuring the number and energy of ions in a beam which backscattered after colliding with atoms in the near-surface region of a sample at which the beam has been targeted. By counting the scattering events between the incident ions and the atoms in the sample, it is possible to determine atomic composition and the thickness of the thin film layers under the sample surface. RBS is ideally suited for determining the concentration of trace elements heavier than the major constituents of the substrate. Its sensitivity for light masses, and for the makeup of samples well below the surface, is poor.

When a sample is bombarded with a beam of high energy particles (He ions), the vast majority of particles are implanted into the material and do not escape. This is because the diameter of an atomic nucleus is on the order of 1×10^{-15}m while the spacing between nuclei is on the order of 2×10^{-10}m. A small fraction of the incident particles do undergo a direct collision with a nucleus of one of the atoms in the upper few micrometers of the sample. This "collision" does not actually involve direct contact between the projectile ion and target atom. Energy exchange occurs because of Coulombic forces between nuclei in the close proximity to each other. However, the interaction can be accurately modeled as an elastic collision using classical physics. The detailed principle of RBS can be found in reference [47] [48]. Figure 2.5 shows the travel of the He ions during a RBS measurement.

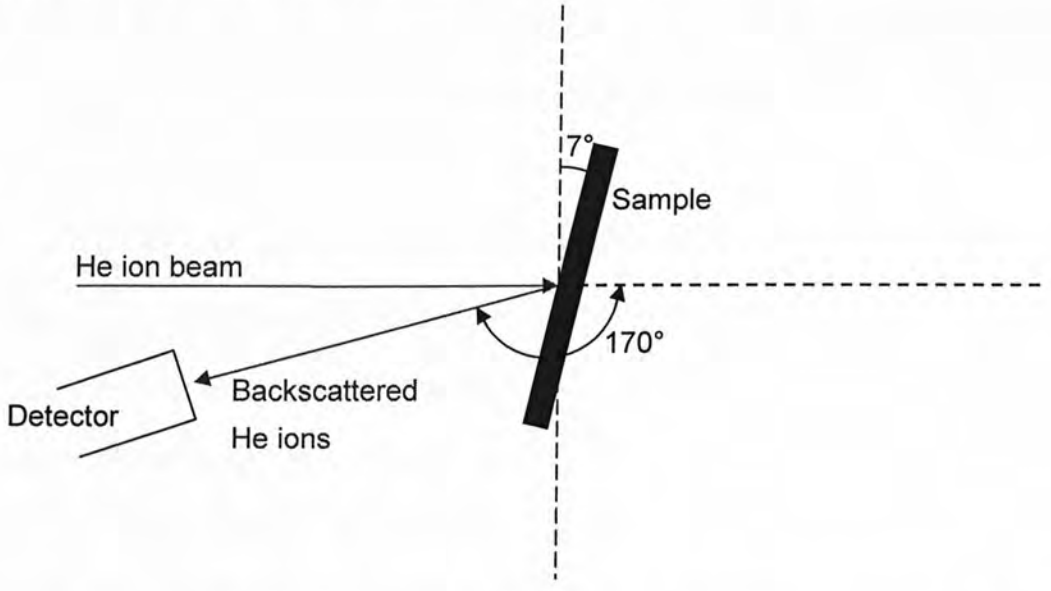

Figure 2.5 The movement of the He ions during the RBS measurement

There are four basic factors which are involved in the ion and solid interaction in the RBS measurement

1. The energy of the projectile after collision can be related to its energy before the collision by means of kinematics factor.

2. The interaction between the projectile and the target atom could be described as an elastic collision between two isolated particles and expressed in terms of scattering cross section.
3. The energy loss of the energetic projectile as it traverses the path due to the coulumbic electrical potential on the target atoms leads to the concept of the stopping cross section.
4. The energy loss process is a statistic process. Thus the mono-energetic projectiles assume an energy distribution after penetrating a given depth of the target. This is known as straggling.

The scattering cross section provides RBS with a quantitative capability, the stopping cross section results in the capability for the depth analysis and the energy straggling sets the limit on the mass and depth resolution.

The RBS spectra of all the implanted samples in the project were taken with a 2MeV He^+ incident beam inside a 2MV tandem accelerator in our lab. The backscattering ions were collected by a surface barrier detector with a resolution of 15keV placed at an angle of 170°. A simulation program called SIMNRA [49] was used to fit the RBS spectra in order to obtain the dose information and the depth profile of the implanted ions inside the substrate.

2.2.4 TEM – Transmission Electron Microscopy

TEM is one of the most powerful techniques in material characterization. It is widely used to study the microstructure, morphology, cross section profile as well as local chemical composition of materials. To take a TEM image, the specimen has to be thinner than the penetration depth of the probe electrons and this is similar to the light is transmitted through materials in conventional optical microscope. Because the wavelength of electrons is much smaller than that of visible light, the optical resolution attainable for TEM images is many orders of magnitude better that of an optical microscope. Typically, the resolution of a TEM image could be in the order of 0.2nm. Moreover, additional functions like transmission electron diffraction (TED) could also provide phase analysis. The detailed principles of TEM could be found in reference [50] [51].

However, unlike RBS and XRD, TEM is a destructive technique and the sample preparation is time consuming and difficult since the samples have to be milled to less than 30-40nm. The details on the sample preparation of plan view and cross-sectioned TEM could be found in the reference [52] [53].

2.2.5 Field Emission Measurement

The measurement of the field emission properties of all the implanted samples were taken at room temperature inside an ultra-high vacuum chamber with a base pressure better than 2×10^{-8}Torr. Figure 2.6 shows the schematic of the field emission measurement system.

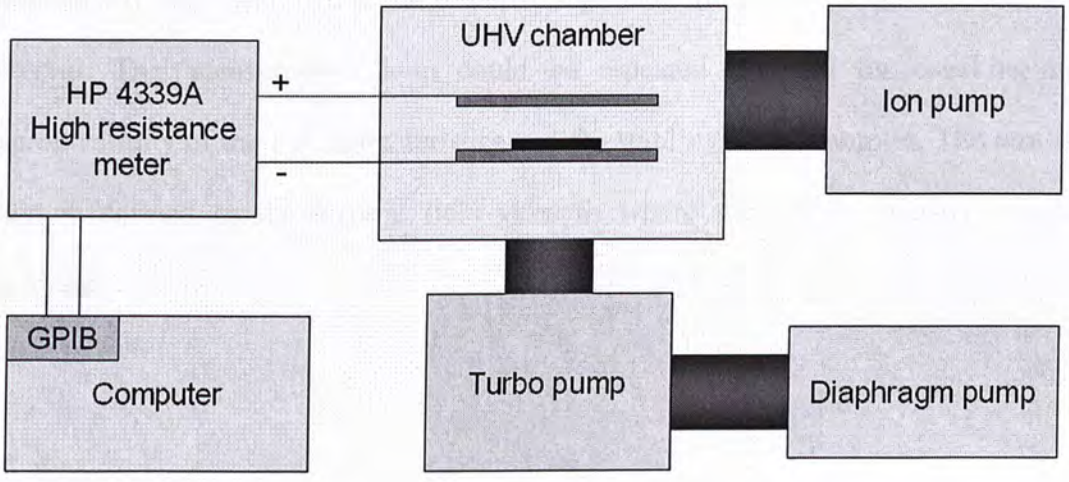

Figure 2.6 Schematic of the field emission measurement system

The voltage versus current plot is obtained in each measurement. The samples are placed between two copper electrodes and the distance between the sample surface and the copper anode is fixed by a mica spacer at about 20μm. Then a current density (J) and applied electric field (E) could be obtained after the mica thickness and the emitted area is determined.

In this work, Hewlett Packard HP4339A high resistance meter is used for the measurement of I-V characteristics. It is computer controlled and the measurement could be repeated four times with fixed voltage step. The leakage current of the HP4339A meter is less than 10^{-9}A and the maximum output current is 0.01mA. The maximum voltage is limited to 1000V. In each measurement, the sample is subjected to an applied voltage from an initial voltage with a fixed voltage step and time interval until the emission current reaches a preset value. After that, the applied voltage will decrease down to the initial voltage with the same voltage step and time interval. This measurement loop could be repeated 4 times for checking the reproducibility of the I-V characteristics and the stability of the samples. The turn-on field is defined as the electric field strength where the current density reaches $1\mu A/cm^2$.

3.1Introduction

In recent years, the investigation of new cold electron field emission materials has been drawing lots of attention in the material world because of their possible application on high speed and high frequency vacuum microelectronic devices as well we field emission displays. Diamond and diamond film [3-4], amorphous carbon layers [5-11], nanotubes [12-13], silicon carbide layers [14-18] and nano-composite dielectric films [19-20] have been studied by many research groups. In the research in nano-composite dielectric films, it is suggested that the surface morphology and the electrical inhomogeneity of the samples could lead to a local field enhancement [24]. One of the goals in our project is to verify these field enhancement mechanisms by studying the field emission properties of the Co-SiO_2 and Fe-SiO_2 samples.

In this chapter, the field emission properties of as-implanted Co-SiO_2 samples were studied. These samples were prepared by or Co implantation on a 100nm SiO_2 films which were thermally grown by dry oxidation and the oxide thickness was verified by ellipsometry. Samples with three different doses were named with prefix LD (low dose = $1x10^{17}cm^{-2}$), MD (middle dose = $2x10^{17}cm^{-2}$) and HD (high dose = $3x10^{17}cm^{-2}$) respectively. In the following parts, the RBS results as well as the relationship between the implanted dose and the field emission properties are shown. The AFM images were taken for the studied for the surface morphology. Furthermore, the field emission properties such as the turn-on field and the field enhancement factor β are determined from the *J-E* plots and the Fowler-Nordheim plots (*F-N* plot).

3.2 RBS results

RBS is a versatile technique for the determination of the retained dose presence in the thin films after implantation. Moreover, it could be used to estimate the thickness of the films if the densities of the films are known.

In the simulation, a three layer model instead of one layer is used for more accurate result. Each layer is composed of different composition of Co, Si and O. This is similar to the real situation because, after implantation, the distribution of the implanted ions will follow the Gaussian model rather than an even distribution inside the substrate.

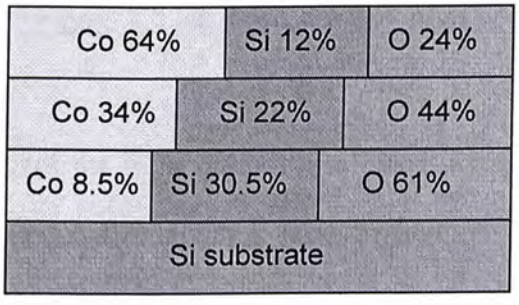

Figure 3.1 The simulation parameters for the HD-Co sample

The following figure shows the RBS spectrum of and the HD-Co sample. The red curve is the experimental data and the blue curve is the simulation result.

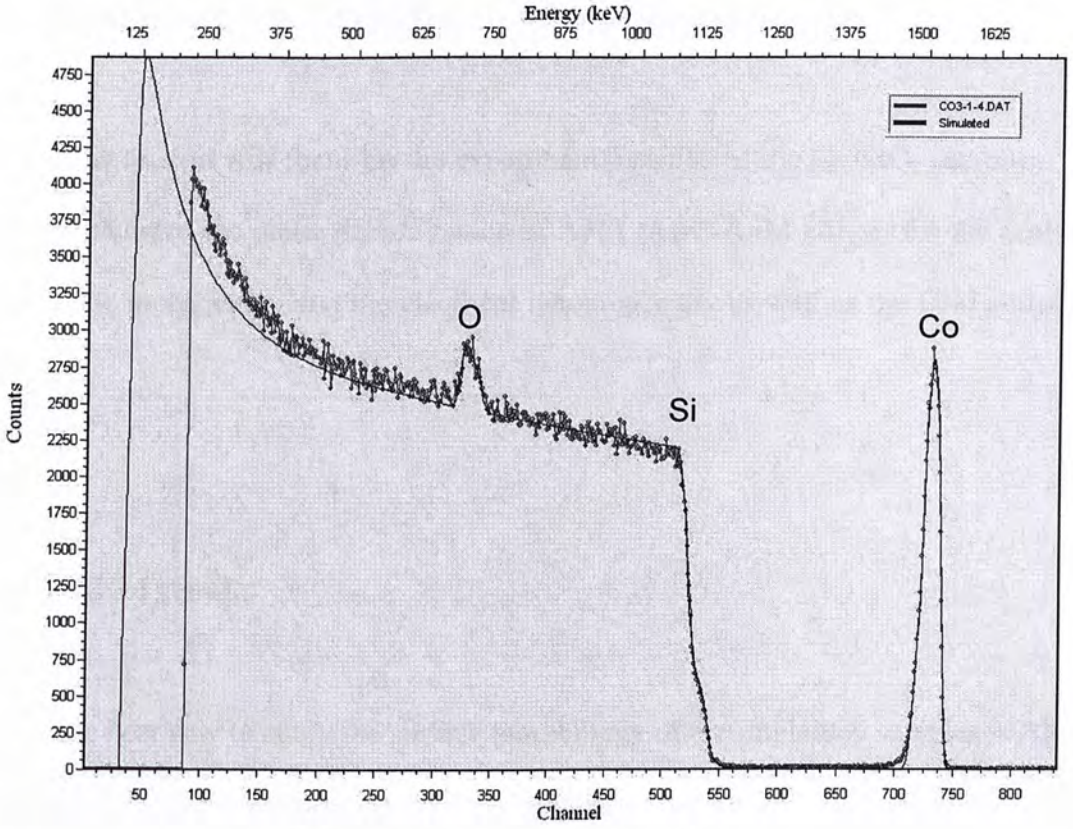

Figure 3.2 RBS spectrum of HD-Co

Table 3.1 summarizes the RBS results of all the Co implanted samples. As the implantation dose increases, the thickness of the remained films decreases. This is because the implanted ions kicked out the host atoms at the surface of the sample. This effect is known as sputtering effect.

Sample code	Nominal dose (cm^{-2})	Retained dose (cm^{-2})	Thickness (10^{15} atoms/cm^2)
LD-Co	$1x10^{17}$	$7.28x10^{16}$	620
MD-Co	$2x10^{17}$	$1.60x10^{17}$	605
HD-Co	$3x10^{17}$	$1.32x10^{17}$	510

Table 3.1 Summary on RBS results

3.3 Experimental results of Co-SiO_2 as-implanted samples

This section will focus on the experimental results of the Co-SiO_2 samples. The results included the phase determination of AFM and C-AFM images for the analysis in surface morphology and the electrical inhomogeneity as well as the field emission results.

3.3.1 AFM results

The best way to study the surface morphology of the implanted samples is AFM. The following three pictures are the AFM images of the Co-SiO_2 samples.

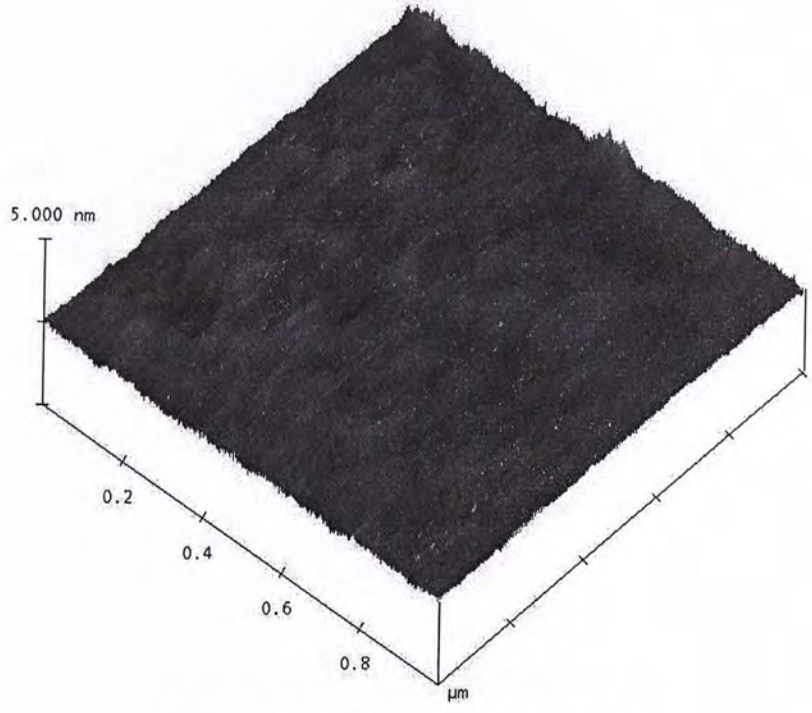

Figure 3.3 The AFM image of LD-Co

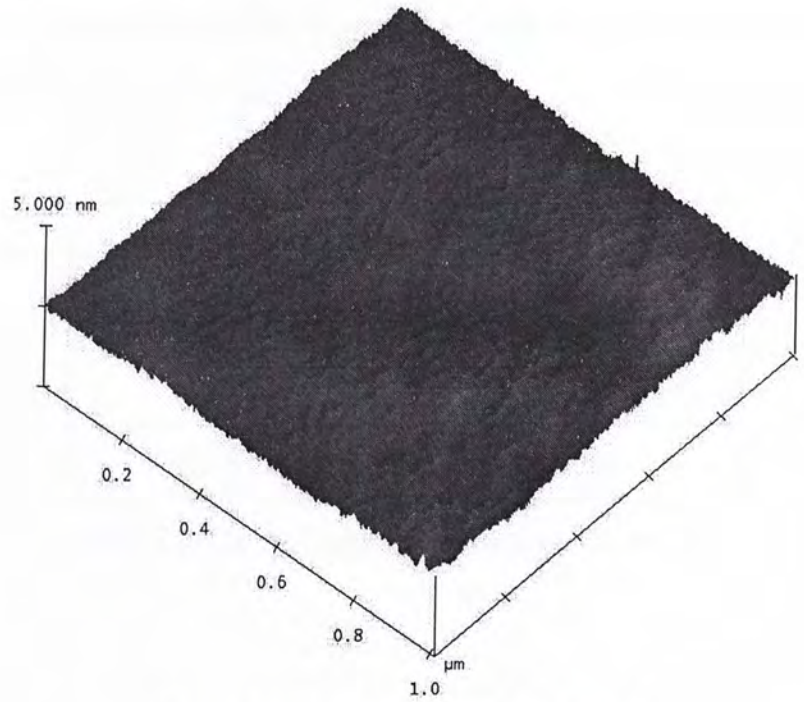

Figure 3.4 The AFM image of MD-Co

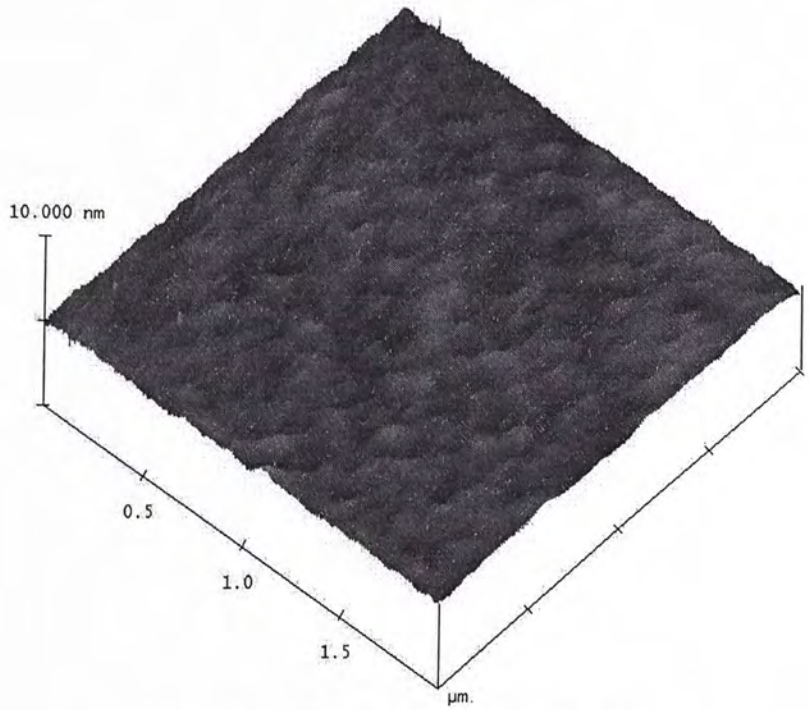

Figure 3.5 The AFM image of HD-Co

All the Co samples are found to be very smooth. As the implanted dose increases, the surface becomes slightly rougher.

Sample code	Roughness (r.m.s.)
LD-Co	0.152nm
MD-Co	0.186nm
HD-Co	0.250nm

Table 3.2 The surface roughness of the Co samples

3.3.2 Field emission properties of as-implanted Co-SiO_2

A pure Co film is prepared by e-beam evaporation for comparison with the Co-SiO_2 nano-composite thin films. The thickness of the Co film is about 200nm. Figure 3.6 shows the *J-E* of the pure Co sample.

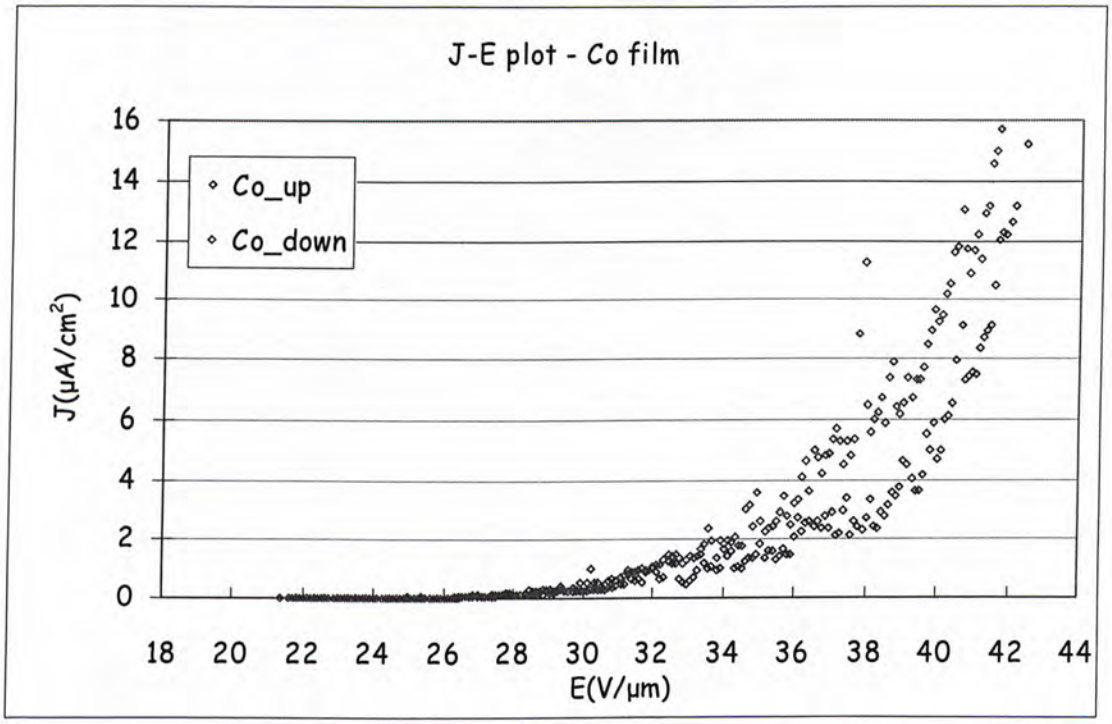

Figure 3.6 The *J-E* plot of a pure Co thin film

The turn-on field of the Co film sample is about 32 V/μm. And the field enhancement factor is about 31.2.

The *J-E* characteristics and the *F-N* plot of the Co-SiO_2 samples are shown in Figures 3.6, 3.7 and 3.8. The turn-on voltage is defined as the applied electric field at which the current density reaches 1μA/cm^2.

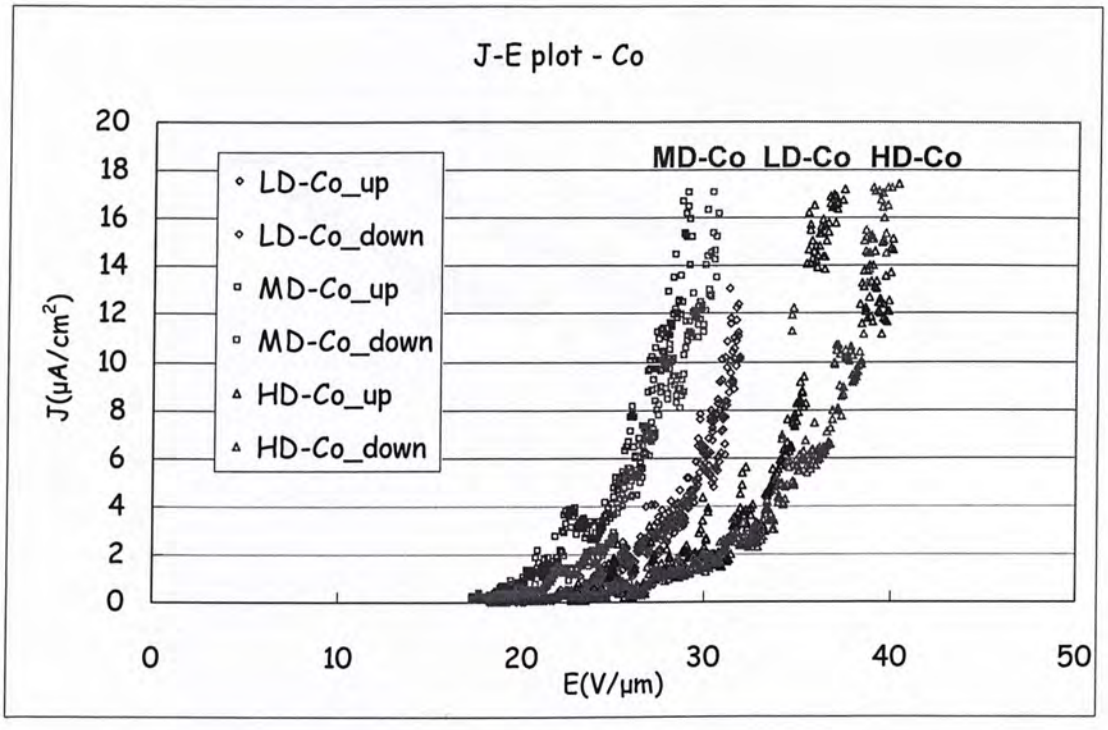

Figure 3.7 The *J-E* plot of Co samples with different implanted dose

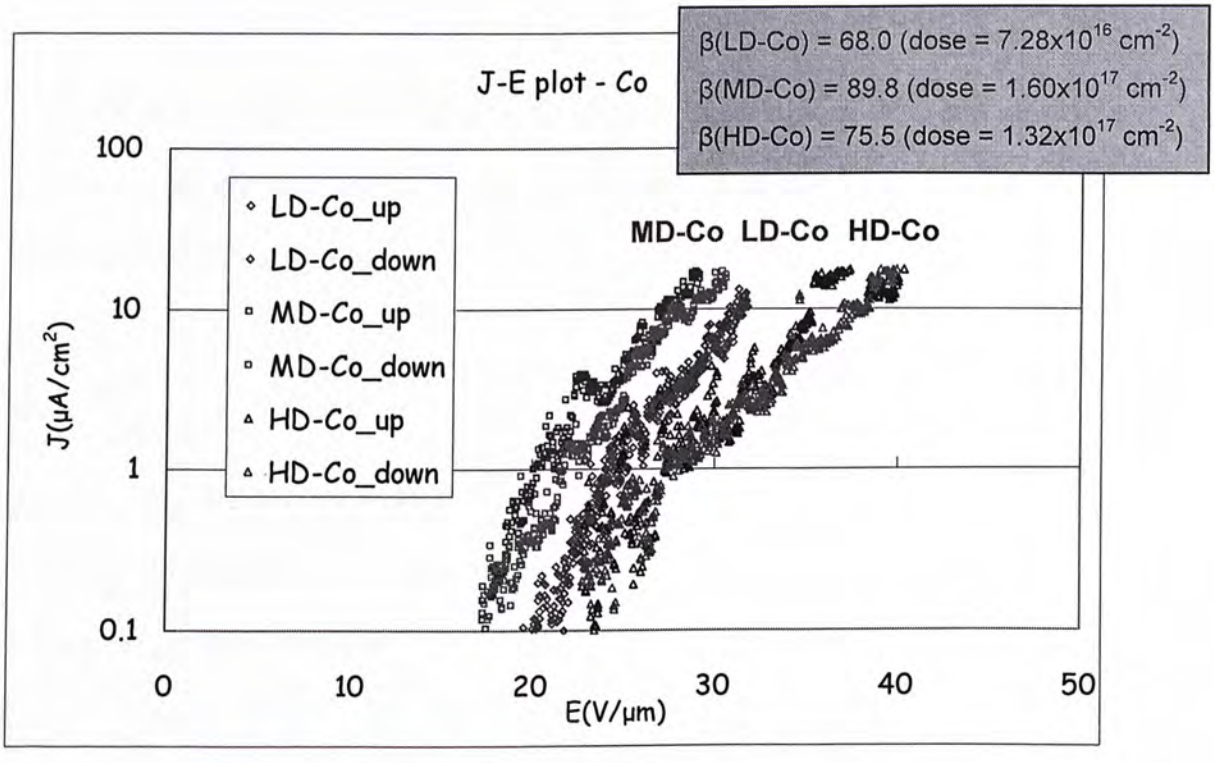

Figure 3.8 The *J-E* plot of Co samples in log scale

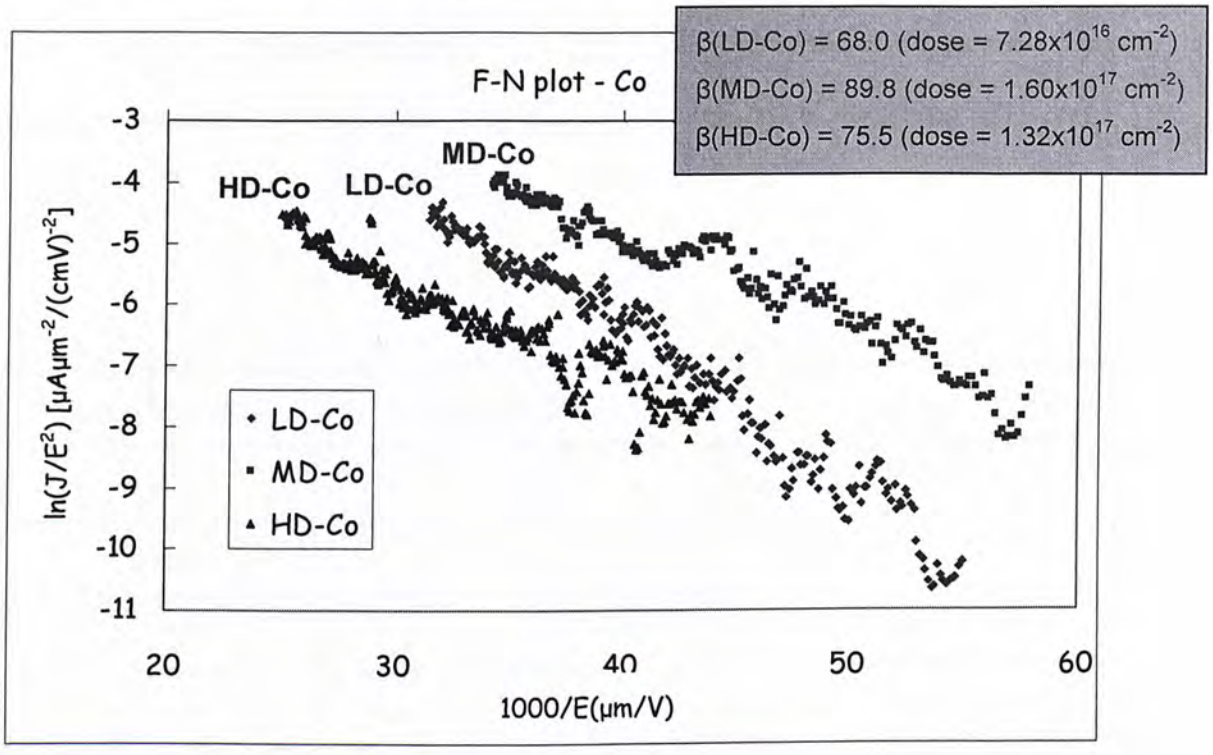

Figure 3.9 The *F-N* plot of Co samples with different implanted dose

From the above *J-E* plots, it is observed that the MD-Co shows the lowest turn-on field among all the as-implanted Co samples.

The field enhancement factor β is directly proportional $\Phi^{3/2}$ and inversely proportional to the slope of the *F-N* plot. Therefore the value of β could be determined from the slope of the *F-N* plot.

$$\beta = k\frac{\Phi^{3/2}}{\text{slope}} \qquad (3.1)$$

β is the field enhancement factor

Φ is the work function of the emission material

k is the proportional constant

By taking k = 1, we can obtain the relative value of β in arbitrary unit. The work function of Co is 5eV [54] and the field emission properties of the Co-SiO_2 are

summarized in the following table with a bare n-Si (100) sample as reference. This reference sample has been cleaned in HF solution and has a resistivity 0.01Ωcm - 0.02Ωcm.

Sample code	Turn-on field (V/μm)	β (a.u.)
Si	26.2-29.5	60.4
Co film	32	31.2
LD-Co	22.1-26.1	68.0
MD-Co	20.1-23.8	89.8
HD-Co	24.8-30.0	75.5

Table 3.3 Summary on field emission properties of as-implanted Co samples

It is found that MD-Co has the lowest turn-on field and largest β. As the implanted dose further increases, i.e. the HD-Co sample, there is a small decrease on the β value while the turn-on field has a big retardation and even worse than LD-Co. All Co implanted samples have better field emission properties than the bare Si and Co film samples.

3.4 Step-like and jump-like features in the *J-E* plots

In the *J-E* measurements, each sample is measured for eight times with up and down in four cycles in order to confirm the reproducibility of the electron field emissions. It is found that there are some step-like and jump-like characteristics in the *J-E* plots as shown in figure 3.9.

These step-like and jump-like features are not repeatable in every measurement but similar step-features might be found throughout the four cycles of measurement. Another property is that the features are more obvious in the high implanted dose samples such as HD-Co. Moreover, the features might vary in position where they appear.

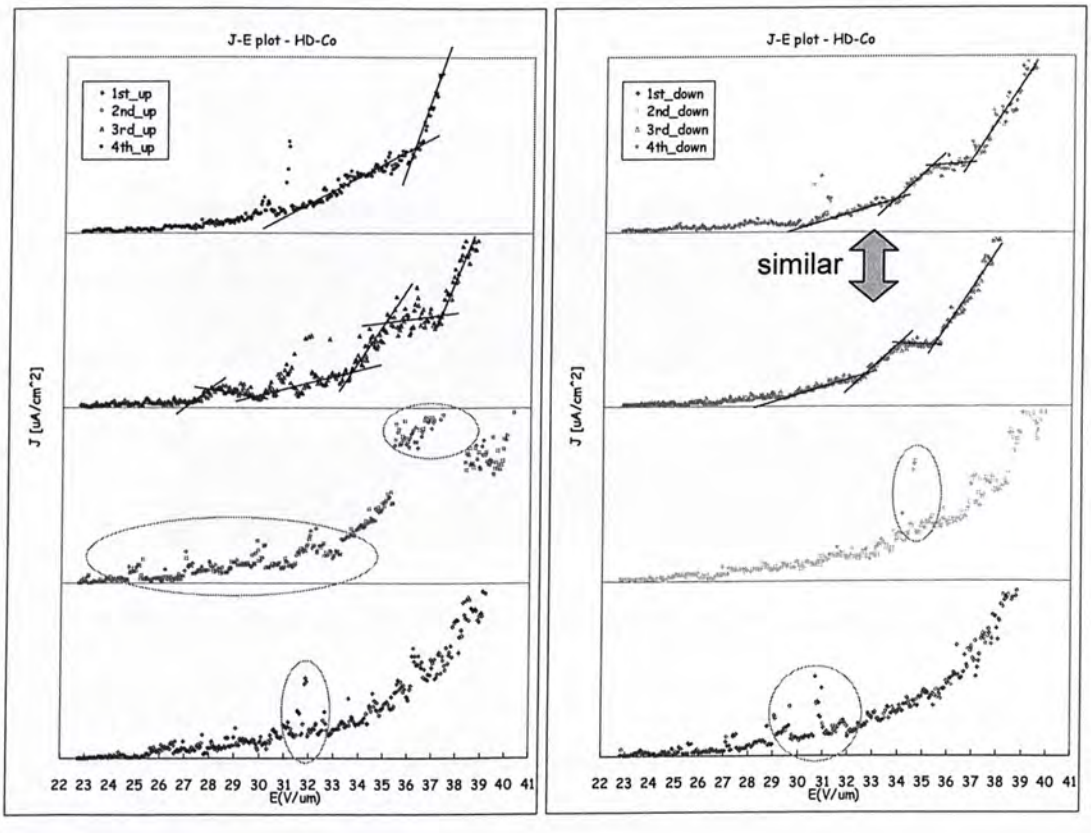

Figure 3.10 Step-like and jump-like features found in HD-Co

Two models are proposed for the step-like and jump-like features found in the *J-E* plots. The first model is that there is formation of new conducting paths due to the conducting grains modification inside the dielectric during the electron field emission. Another model is the local self-annealing caused by the field emission current.

Formation of new conducting paths

After the ion implantation, the implanted atoms would distribute over the dielectric layer in the form of tiny grains and would be in a non-equilibrium stage. The ion distribution profile would follow the Gaussian distribution model with more ions in the middle and less ions at both ends. These ions presence in the form of tiny conducting gains might align together forming a conducting path connecting the n-Si substrate to the grains at the surface of the dielectric where the electron field emission occurs as shown in figure 3.10.

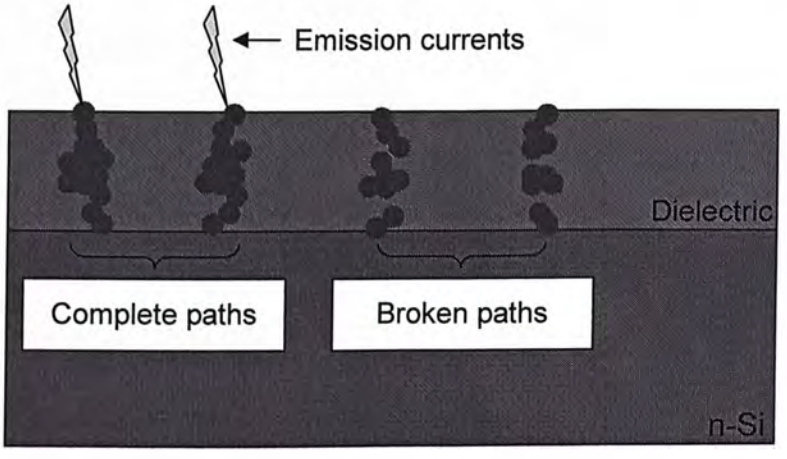

Figure 3.11 The cross profile of an as-implanted nano-composite dielectric

But as long as the external applied electric field is getting higher, the broken paths might be completed as electrons penetrate through the dielectric at the gap and

this is known as the pre-emission events. In some cases, as long as the electrons keep flowing through the gap, heat energy is released and the atomic arrangement might be destroyed. Therefore, the implanted atoms might diffuse into the gap and a complete conducting path is formed.

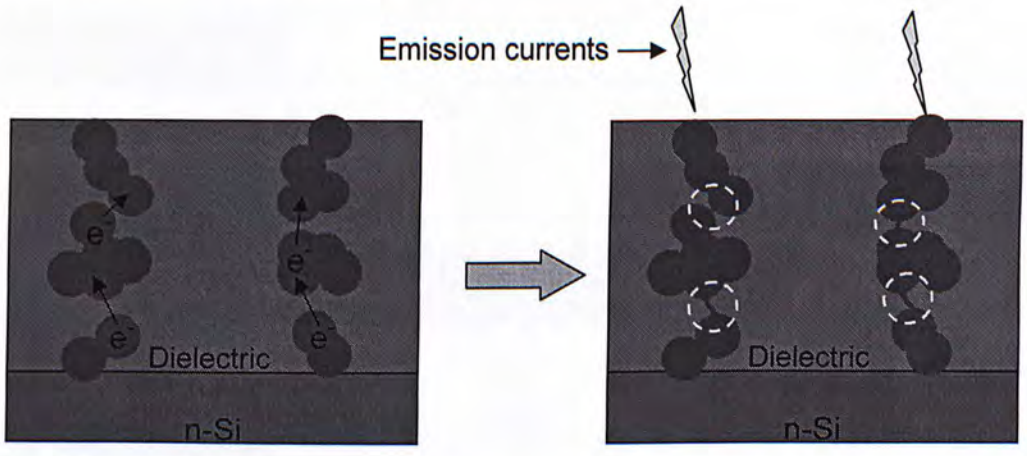

Figure 3.12 The formation of new conducting paths inside the dielectric layer

The formation of new conducting paths is able to account for the slopes become steeper in the *J-E* plots since the number of emission currents increases. But it fails to explain those slope become gentler.

Local self-annealing

This is another possible explanation for the step-like characteristics found in the *J-E* plots. Moreover, it could also accounts for the jump-like features.

During the electron field emission, there would be heat energy given out due to joule heating. The released heat would be either lost to the surroundings or absorbed by the tiny conducting grains. Once it is absorbed, the conducting grains could diffuse and combine to form larger grains. As the conducting grains at the emission surface become larger, they might stop emitting electrons since the electric field lines

are less concentrated at larger grains and this leads to the decrease in current density. On the other hand, new conducting paths might form as the grains inside the dielectric grow larger. The effect is illustrated in the picture below.

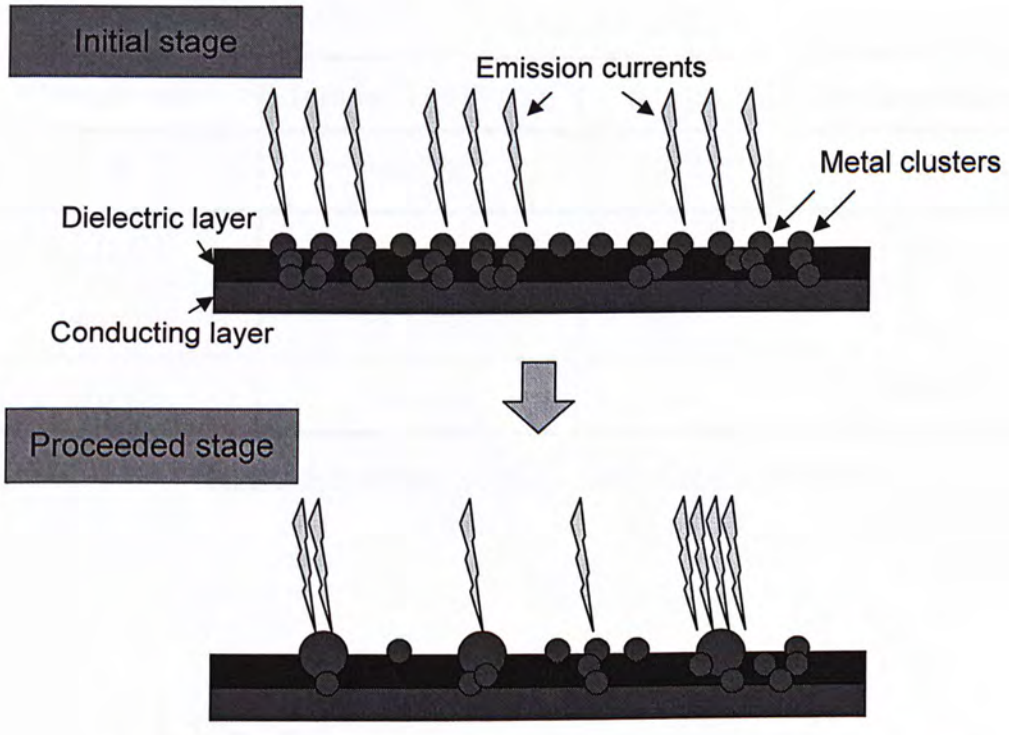

Figure 3.13 The effect of local self-annealing on the dielectric layer

3.5 Chapter summary

In this chapter, the field emission properties of the as-implanted Co-SiO_2 were shown. The following table and graph summarize the experimental results.

Sample code	Turn-on field (V/μm)	β (a.u.)	Roughness (r.m.s.)
Si	26.2-29.5	60.4	0nm
LD-Co	22.1-26.1	68.0	0.152nm
MD-Co	20.1-23.8	89.8	0.186nm
HD-Co	24.8-30.0	75.5	0.250nm

Table 3.4 Summary on all the as-implanted samples

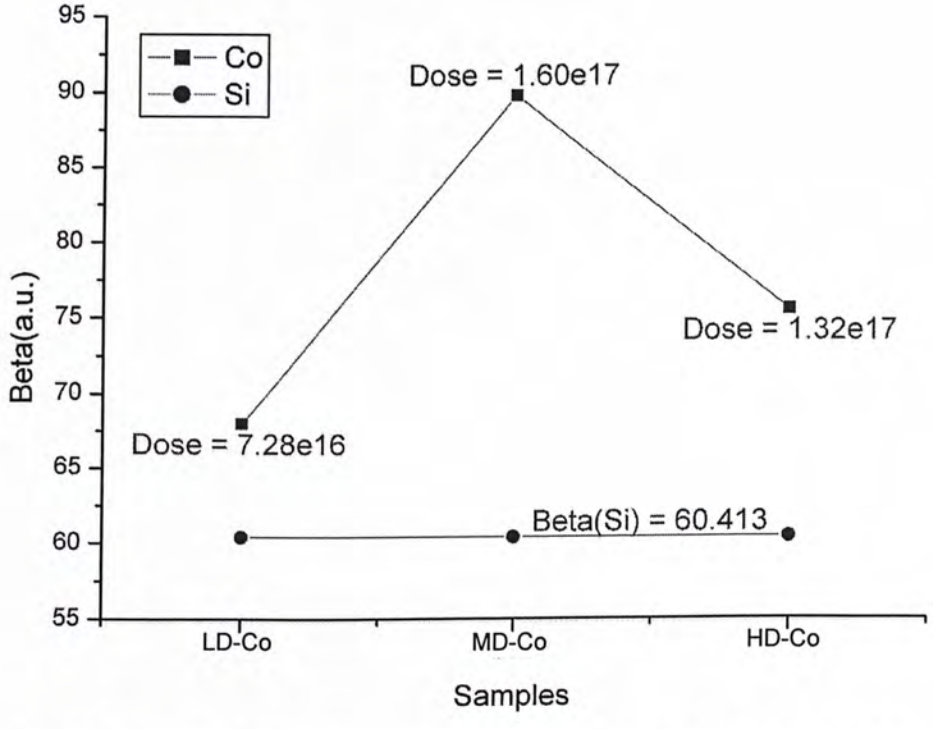

Figure 3.14 The field enhancement factor of the Co implanted samples

Here are some important findings:

1. All the Co implanted samples show a better field emission performance than the bare Si sample.
2. MD-Co shows a larger field enhancement and larger turn-on field.
3. MD-Co shows the lowest turn-on field (20.1-23.8 V/μm) and the largest field enhancement factor β (89.8) which are two times larger than that of bare Si.
4. Compared to MD-Co, HD-Co has a rougher surface but both the turn-on field and the β are smaller than those of MD-Co. This implies that the there exists other factors affecting the field enhancement mechanism.
5. Step-like and jump-like features were found in *J-E* plots. The reasons might be due to the formation of new conducting paths and the local self-annealing.

4.1 Introduction

In this chapter, the field emission properties of as-implanted Fe-SiO_2 and annealed $FeSiO_2$ samples were investigated. Similar to those Co-SiO_2 samples in the last chapter. These samples were prepared by Fe implantation on a 100nm SiO_2 films which were thermally grown by dry oxidation and the oxide thickness was verified by ellipsometry. In addition, some of the samples were treated by Rapid Thermal annealing (RTA) with different annealing temperature. Samples with three different doses were named with prefix LD (low dose = $1x10^{17}cm^{-2}$), MD (middle dose = $2x10^{17}cm^{-2}$) and HD (high dose = $3x10^{17}cm^{-2}$) respectively. Moreover, the suffix (_300, _400 and _500) indicated the annealing temperature.

In the following parts, the RBS results as well as the relationship between the implanted dose and the field emission properties are shown. The AFM and CAFM images would be studied for the surface morphology and the electrical inhomogeneity. The last but not least, the field emission properties are determined from the *J-E* plots and the Fowler-Nordheim plots (*F-N* plot).

4.2 RBS results

Similar to chapter 3, a three layer model is used for the simulation. Here shown the simulation parameters.

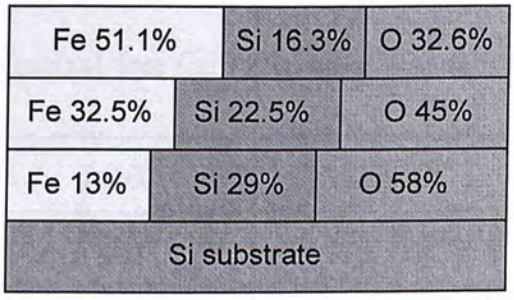

Figure 4.1 The simulation parameters for the HD-Fe sample

The following figure shows the RBS spectrum of the HD-Fe sample.

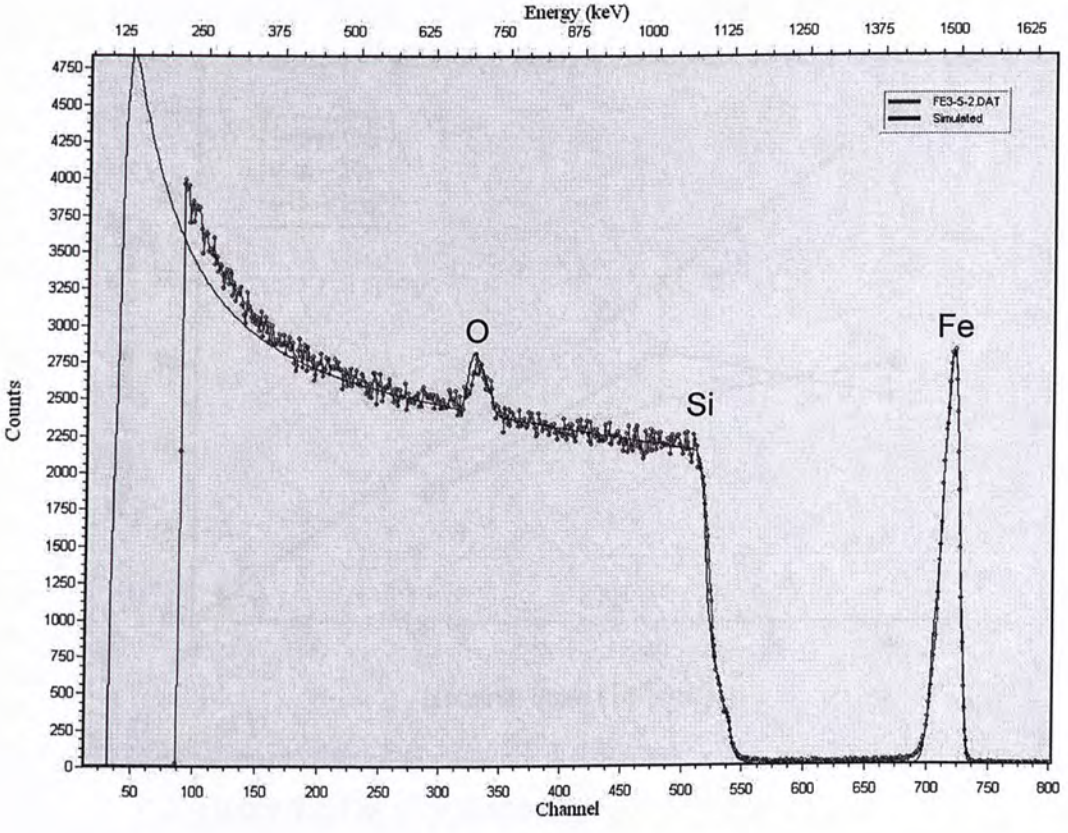

Figure 4.2 RBS spectrum of HD-Fe

Table 4.1 summarizes the RBS results of all Fe the implanted samples. Like the Co implanted samples. The Fe samples are also suffered from the effect of sputtering. The relationship between the nominal dose and the retained dose is shown in figure 4.3.

Sample code	Nominal dose (cm^{-2})	Retained dose (cm^{-2})	Thickness (10^{15} atoms/cm^2)
LD-Fe	$1x10^{17}$	$7.72x10^{16}$	620
MD-Fe	$2x10^{17}$	$1.30x10^{17}$	600
HD-Fe	$3x10^{17}$	$1.52x10^{17}$	525

Table 4.1 Summary on RBS results

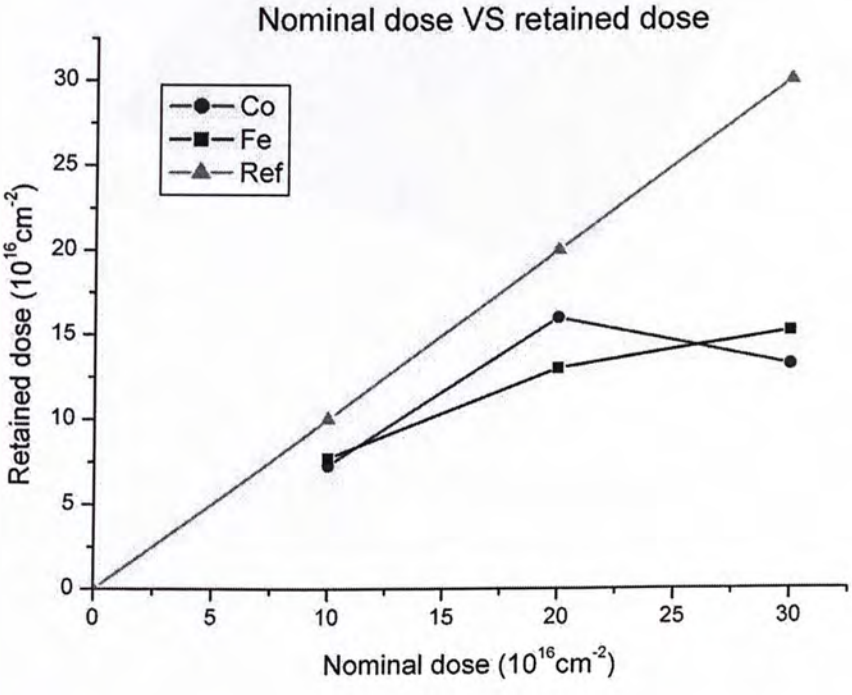

Figure 4.3 The plot of nominal dose VS retained dose

4.3 Experimental results of the Fe-SiO_2 as-implanted samples

Compared to the bare Si sample, the as-implanted Fe-SiO_2 samples also show better field emission properties and the results were shown in the following parts.

4.3.1 AFM results

The AFM images of the Fe-SiO_2 samples are shown in the pictures below.

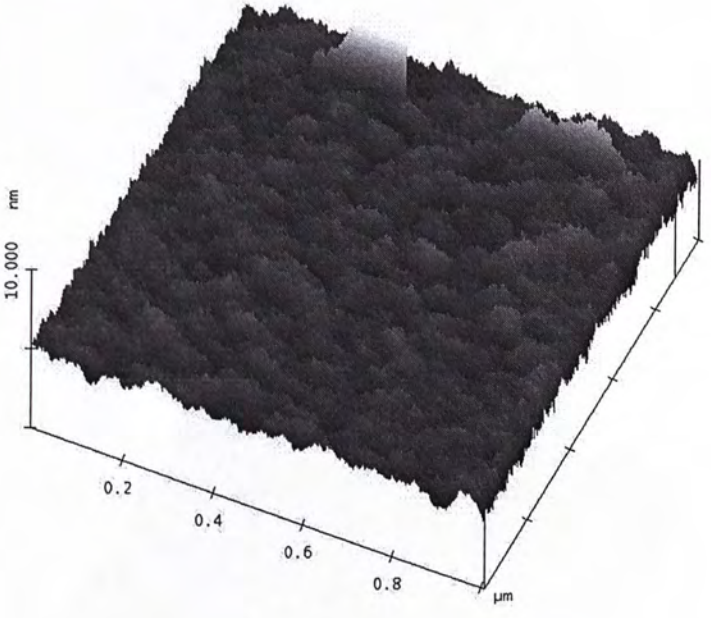

Figure 4.4 The AFM image of LD-Fe

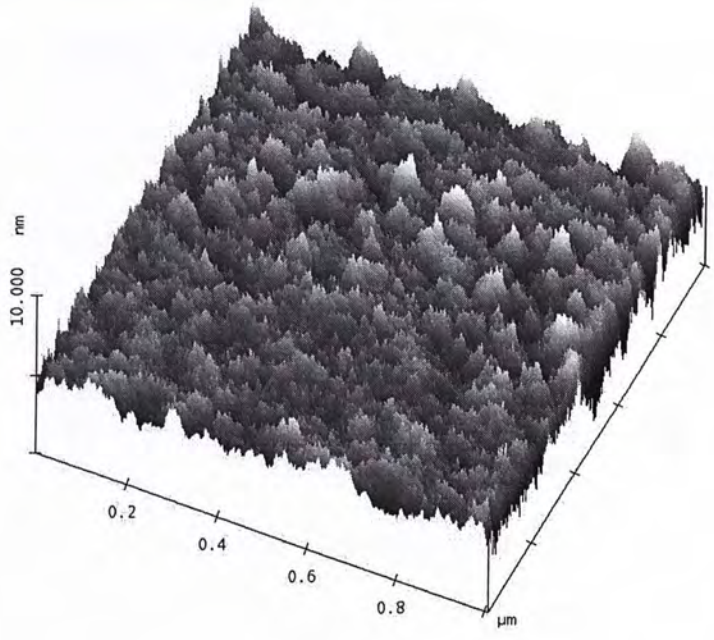

Figure 4.5 The AFM image of MD-Fe

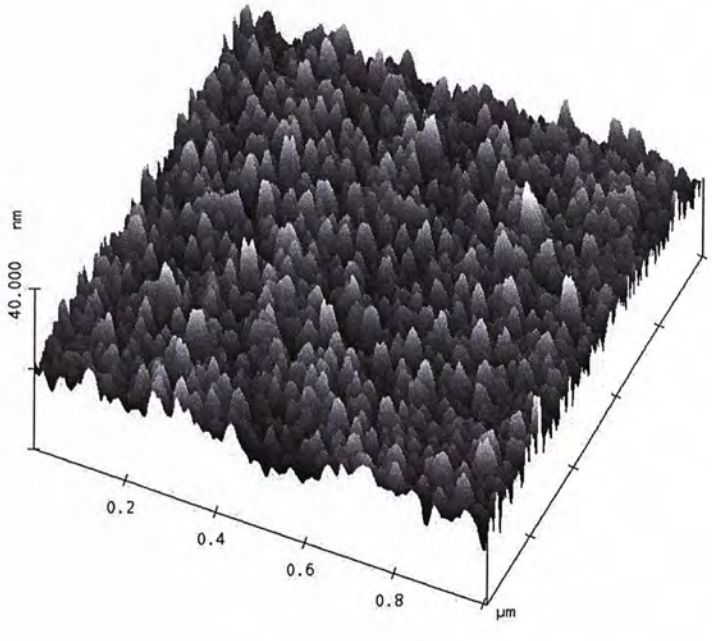

Figure 4.6 The AFM image of HD-Fe

Unlike the Co samples, the Fe samples show a big difference on surface roughness at the implanted dose increases.

Sample code	Roughness (r.m.s.)
LD-Fe	0.372nm
MD-Fe	0.540nm
HD-Fe	2.894nm

Table 4.2 The surface roughness of the Fe samples

4.3.2 Field emission properties of as-implanted Fe-SiO_2

The *J-E* plots and the *F-N* plot of the Fe-SiO_2 samples are shown in figure 4.7, 4.8 and 4.9

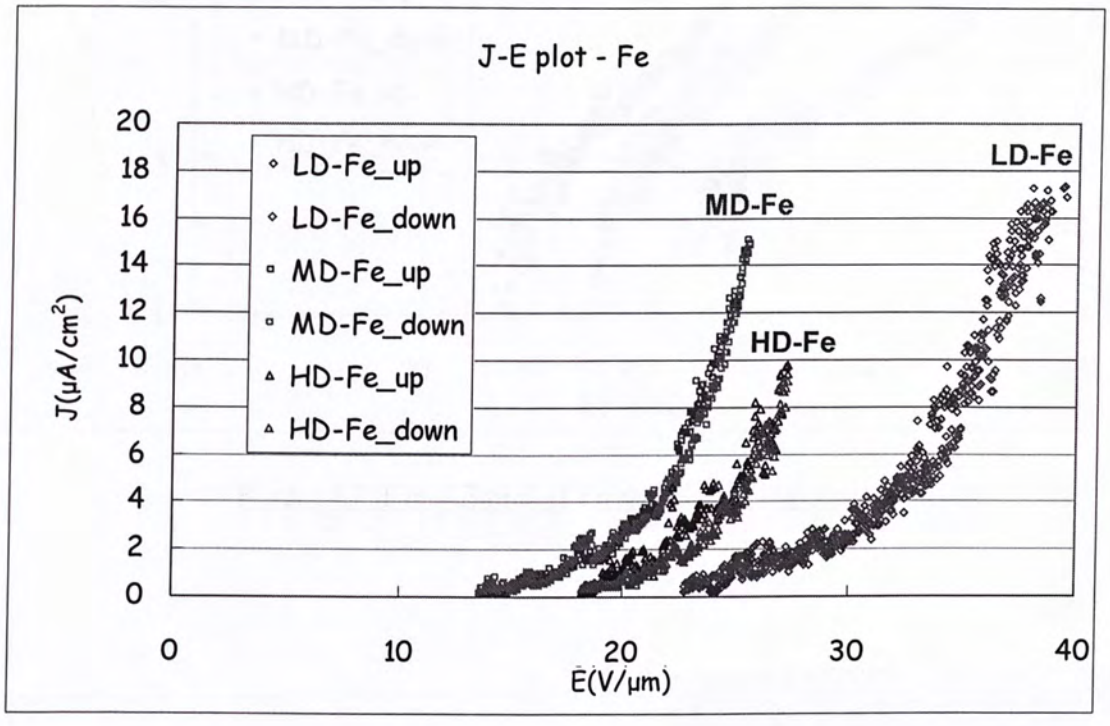

Figure 4.7 The *J-E* plot of Fe samples with different implanted dose

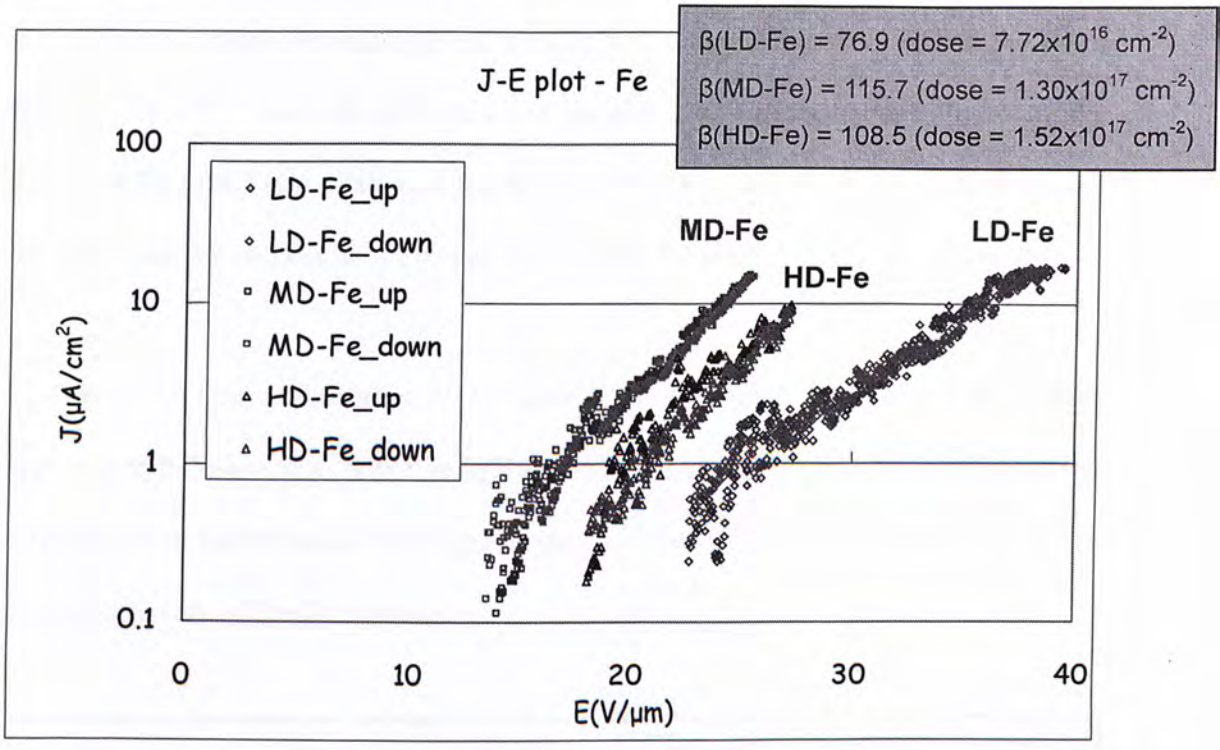

Figure 4.8 The *J-E* plot of Fe samples in log scale

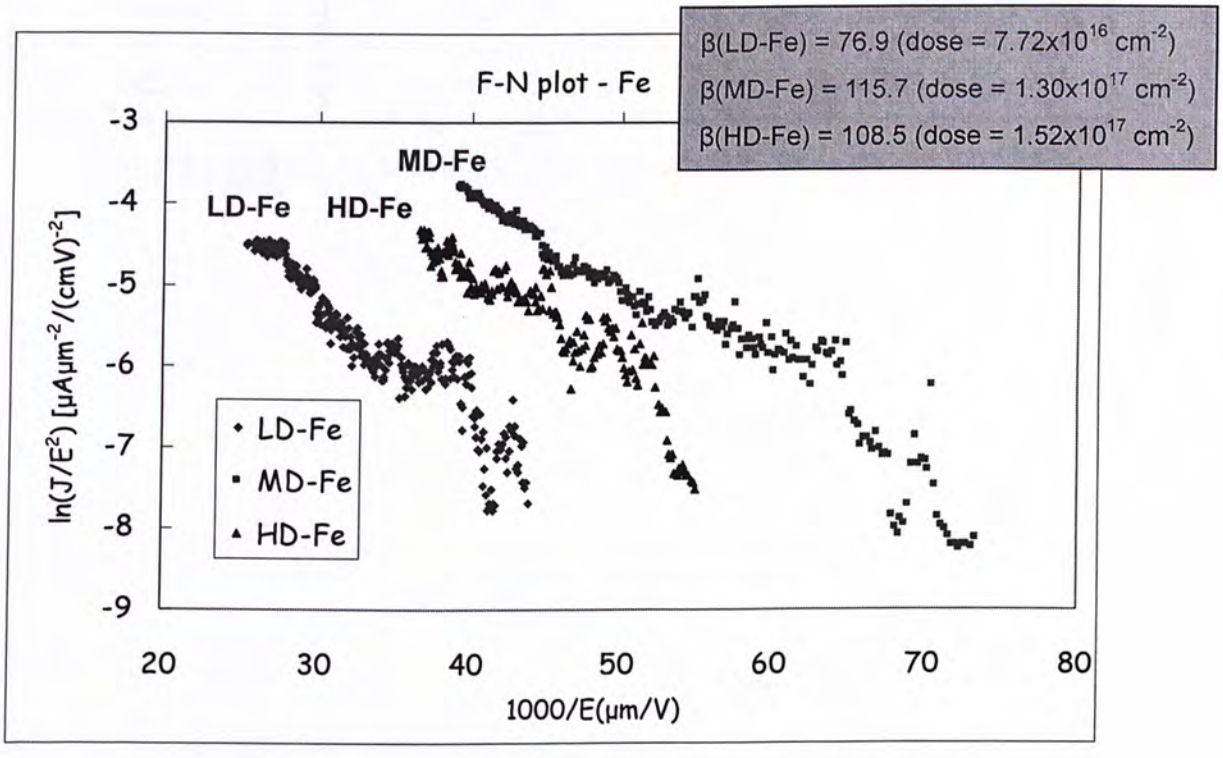

Figure 4.9 The *F-N* plot of Fe samples with different implanted dose

To calculate the β value of the Fe samples, it is necessary to know the work function Φ of Fe. According to the CRC handbook of Chemistry and Physics [54], the Φ of Fe (100) is 4.67eV and the Φ of Fe (111) is 4.81eV. Take the average of these two values and the Φ of Fe is assumed to be 4.74eV.

In the Fe series, similar to the Co series, MD-Fe shows the lowest turn-on field and largest β. There is a reduction in the turn-on field and β value in HD-Fe but the field emission performance is still better than LD-Fe. Table 4.3 summarizes the field emission results of the Fe samples.

Sample code	Turn-on field (V/μm)	β (a.u.)
Si	26.2-29.5	60.4
LD-Fe	24.8-31.6	76.9
MD-Fe	16.9-19.3	115.7
HD-Fe	19.1-22.5	108.5

Table 4.3 Summary on field emission properties of as-implanted Fe samples

4.3.3 Comparison with Co-SiO_2 samples

Compared with the field emission properties of the as-implanted Co-SiO_2, Fe-SiO_2, in general, shows a better field emission performance. The following table and graphs summarize the experimental results.

Sample code	Turn-on field (V/μm)	β (a.u.)	Roughness (r.m.s.)
Si	26.2-29.5	60.4	0nm
LD-Co	22.1-26.1	68.0	0.152nm
MD-Co	20.1-23.8	89.8	0.186nm
HD-Co	24.8-30.0	75.5	0.250nm
LD-Fe	24.8-31.6	76.9	0.372nm
MD-Fe	16.9-19.3	115.7	0.540nm
HD-Fe	19.1-22.5	108.5	2.894nm

Table 4.4 Summary on all the as-implanted samples

	Fe	Co
Electron Configuration	[Ar] $3d^6\ 4s^2$	[Ar] $3d^7\ 4s^2$
Electronegativity	1.83	1.88
1^{st} ionization energy	762.5 $kJ{\cdot}mol^{-1}$	760.4 $kJ{\cdot}mol^{-1}$
2^{nd} ionization energy	1561.9 $kJ{\cdot}mol^{-1}$	1648 $kJ{\cdot}mol^{-1}$

Table 4.5 Physical properties of Fe and Co

Both Fe and Co have two valence electrons at the outermost shell. The reason of better field emission of Fe over Co is that the Fe atoms have a larger tendency to lose

electrons and the 2nd ionization energy is 5.5% lower than that of Co.

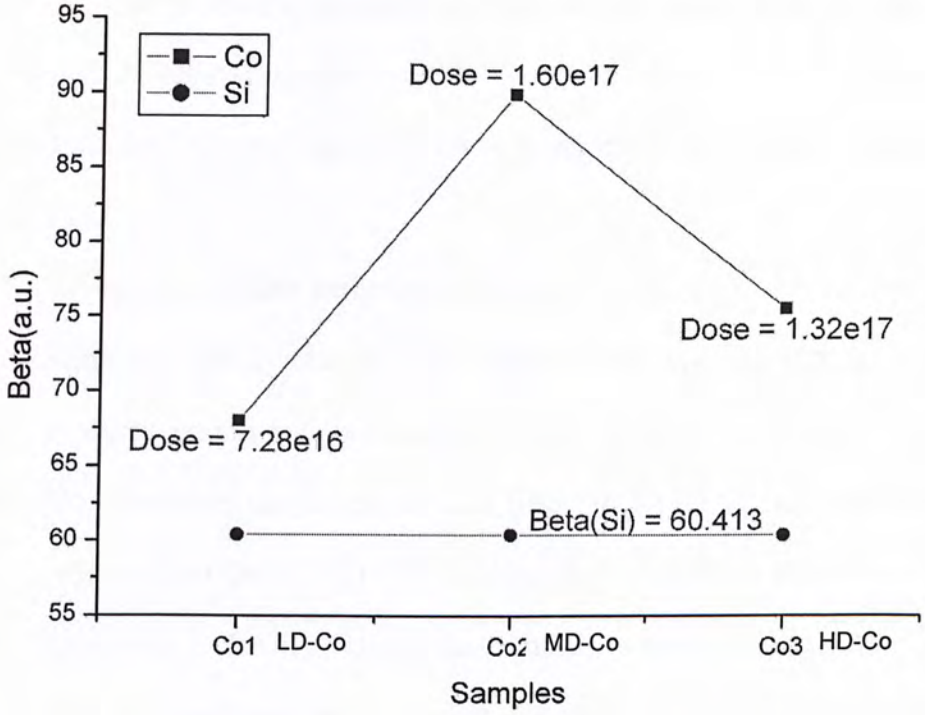

Figure 4.10 The field enhancement factor of the Co implanted samples

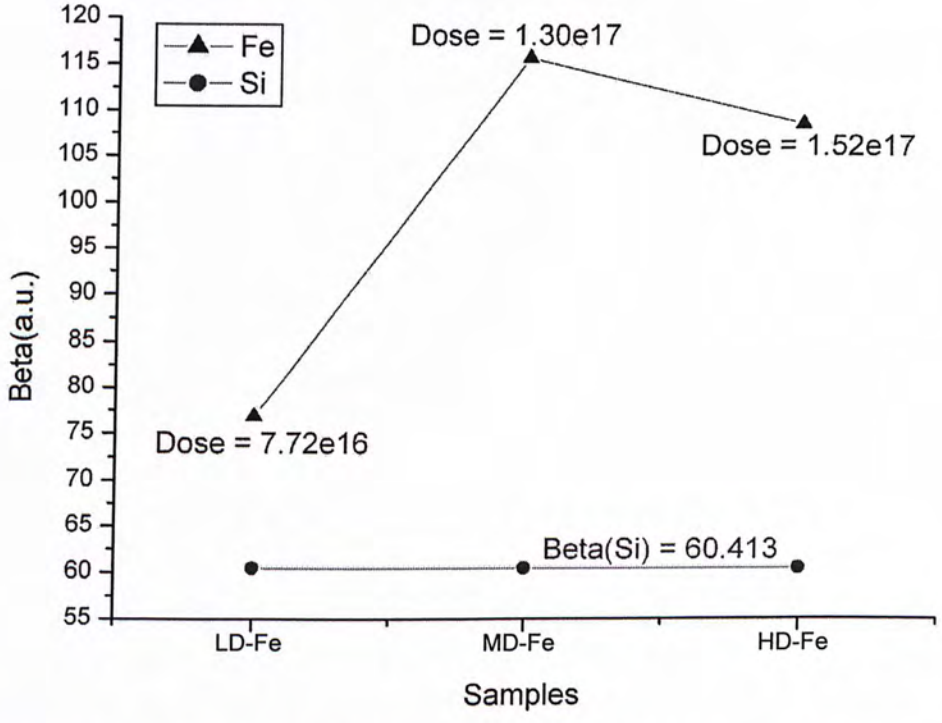

Figure 4.11 The field enhancement factor of the Fe implanted samples

Here are some important findings:

1. All the Co and Fe implanted samples show a better field emission performance than the bare Si sample.
2. Both MD-Co and MD-Fe show a larger field enhancement and larger turn-on field.
3. In general, the field emission performance of Fe samples is better than that of Co samples. This is due to the difference in physical properties such as the electronegativity and the ionization energy between Fe and Co.
4. MD-Fe shows the lowest turn-on field (16.9-19.3 V/μm) and the largest field enhancement factor β (115.7) which are two times larger than that of bare Si.
5. Compared to MD-Fe, HD-Fe has a much rougher surface but both the turn-on field and the β are slightly smaller than those of MD-Fe. This implies that, apart from the surface morphology, there exist other factors affecting the field enhancement mechanism.

4.4 Experimental results of annealed Fe-SiO_2 samples

In this part, the frame will be focused on the effect of annealing on the field emission properties of the Fe-SiO_2 metal dielectric thin films. Due to the supply of heat energy, the tiny metal grains will diffuse, rearrange themselves and aggregate together to form a larger metal grains and this leads to the modification of surface morphology, the conducting paths inside the dielectric layer and, possibly, the electrical inhomogeneity.

4.4.1 Annealing conditions

Each sample set of different doses was treated by RTA at temperature 300°C, 400°C and 500°C in nitrogen ambient for 30 seconds.

4.4.2 AFM and C-AFM results

After the annealing, the AFM images of the Fe samples were taken to investigate the effect of annealing on the surface morphology, the following pictures show the AFM images of HD-Fe samples together with a graph of surface roughness versus annealing temperature.

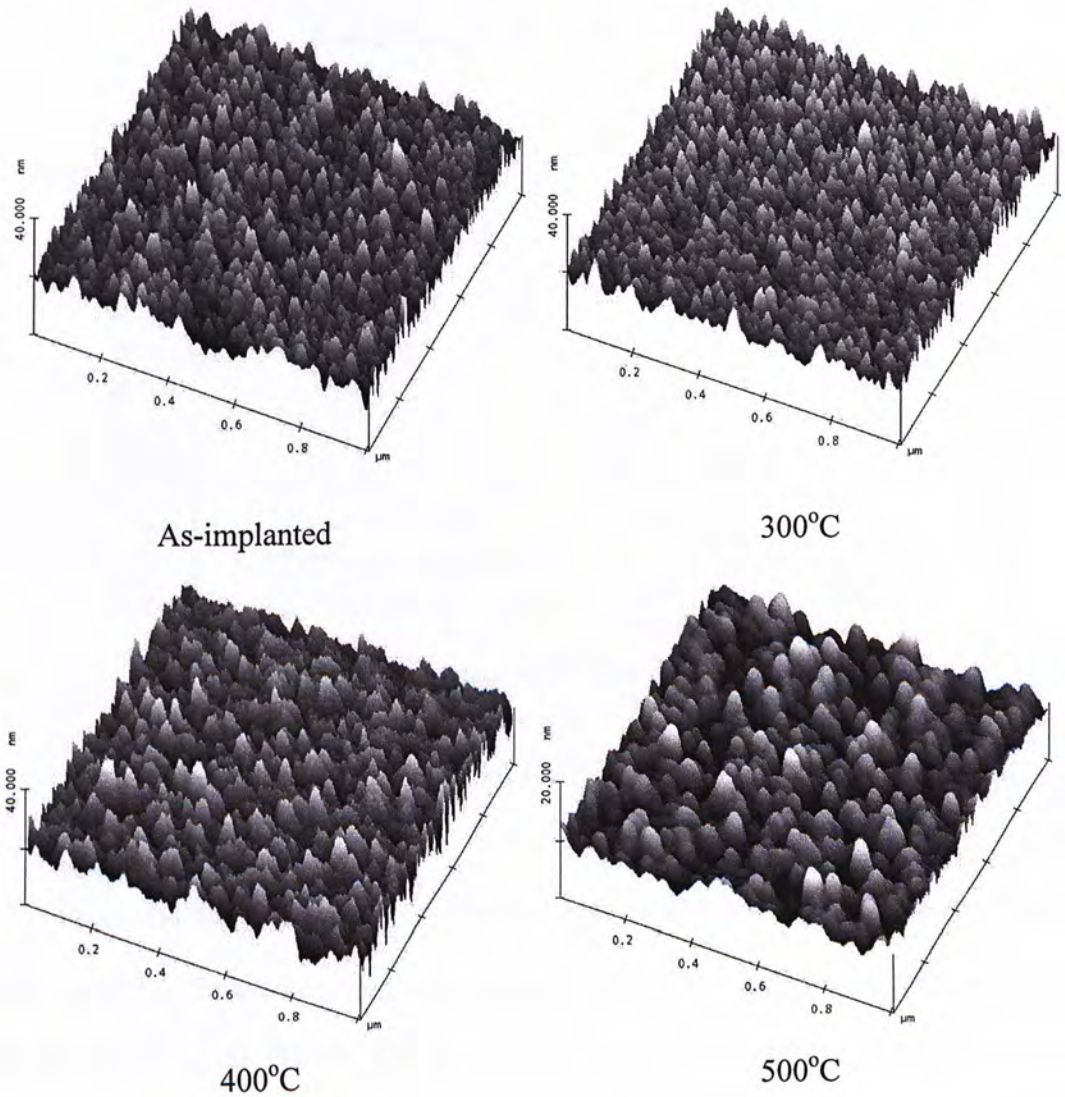

Figure 4.12 Evolution of surface morphology with the increase of annealing temperature

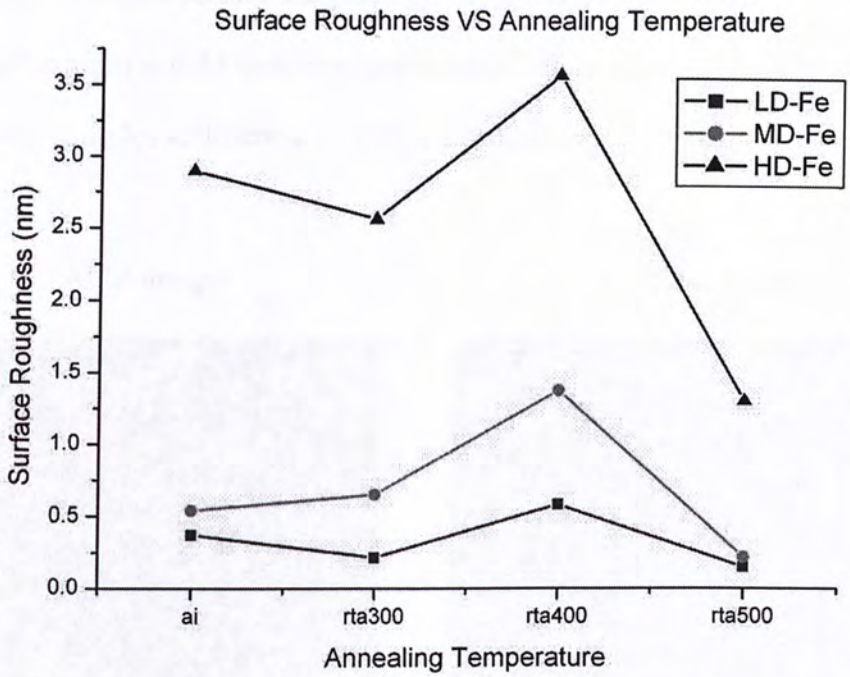

Figure 4.13 Surface roughness VS annealing temperature

From the above figure, it is observed that sample annealing by RTA at 400°C can maximize the surface roughness with the same set of samples. Moreover, among all the samples, the HD-Fe_400 set shows the roughest surfaces. Further increases the temperature to 500°C will reduce the surface roughness since the Fe atoms on the dielectric surface will diffuse towards the Si substrate and leads to s smoother surface..

Apart from the surface morphology, electrical inhomogeneity is also a critical factor affecting the field emission performance. Here shows the C-AFM images of the MD-Fe samples at different annealing temperature.

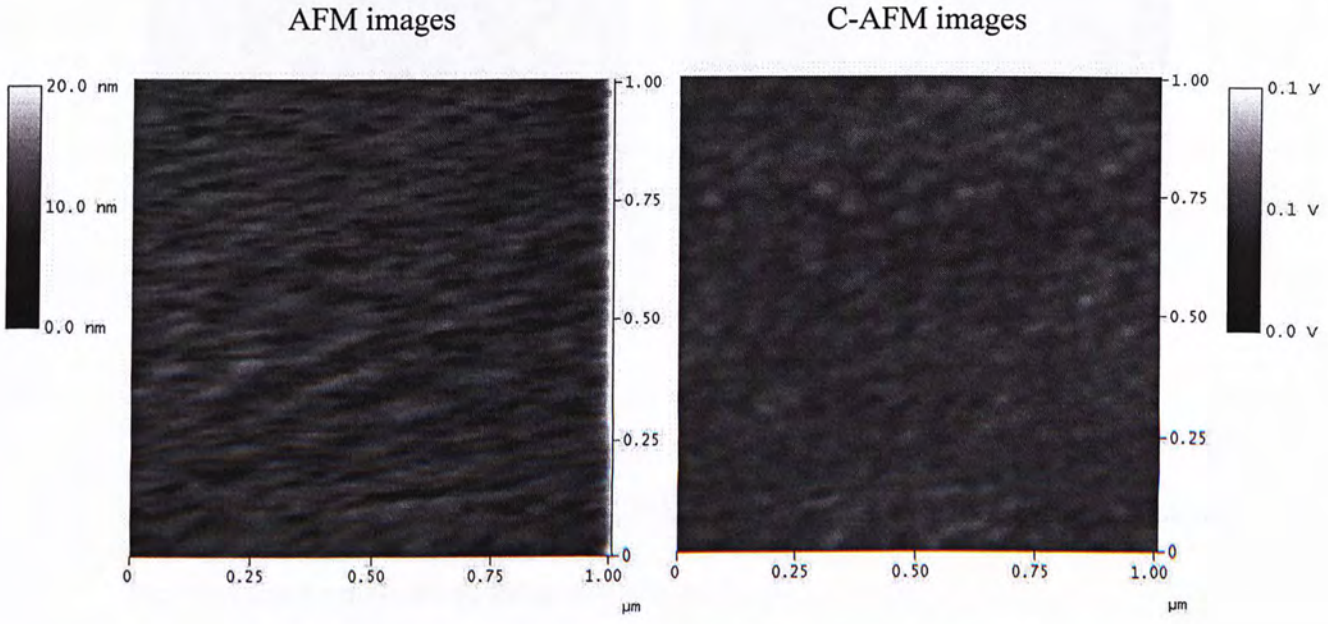

Figure 4.14 AFM and C-AFM images of MD-Fe

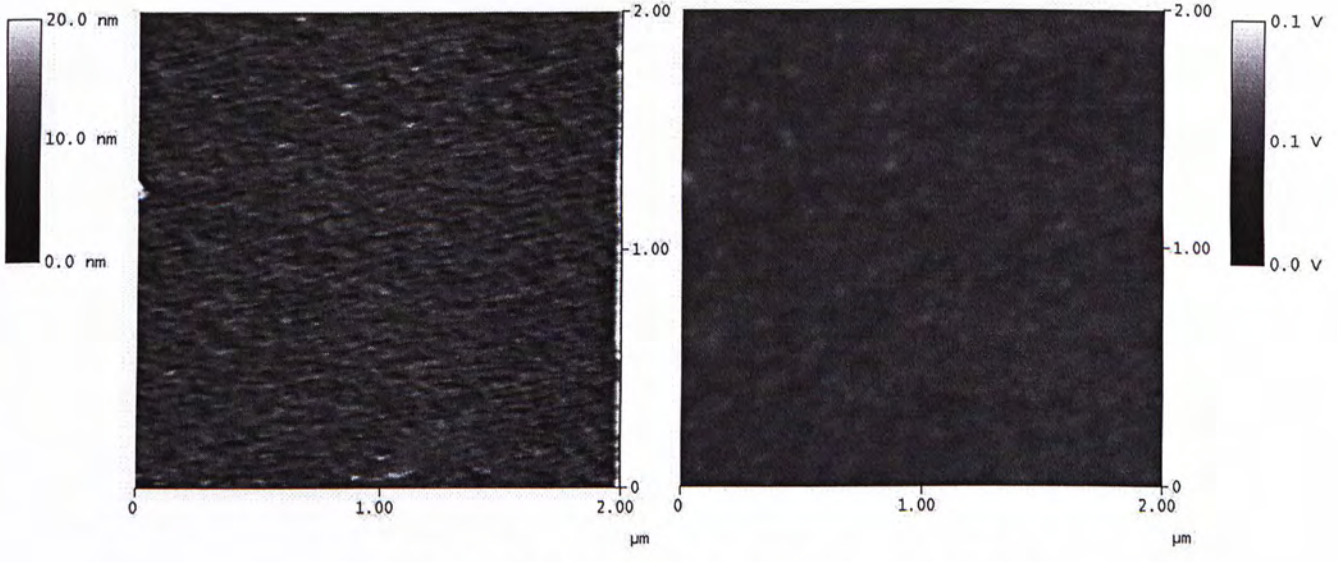

Figure 4.15 AFM and C-AFM images of MD-Fe_400

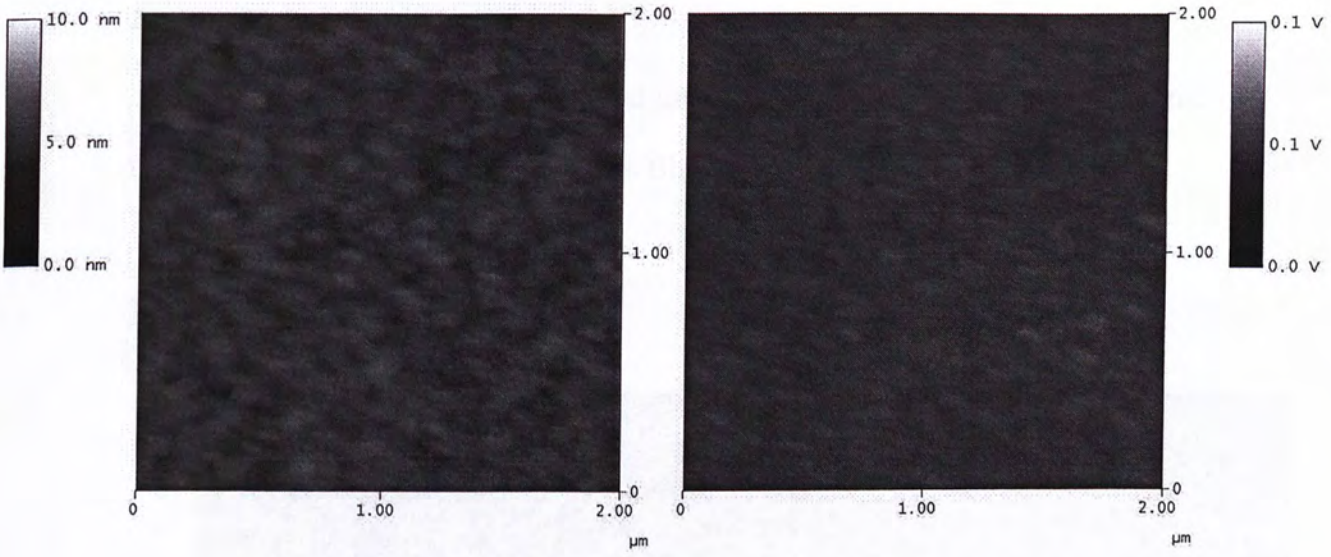

Figure 4.16 AFM and C-AFM images of MD-Fe_500

The as-implanted MD-Fe sample shows a better electrical inhomogeneity compared with the annealing samples. Moreover, a few of the conducting paths or channels can be matched to the protrusion on the AFM images.

But compared with the W-implanted SiC samples made by W. M. Tsang [24], the metal dielectric nano-composite samples prepared in this project do not posses a strong effect of electrical inhomogeneity as shown in the above C-AFM images.

4.4.3 TEM Images

Some of the samples were selected for taking the TEM images in order to study the structure of the nano-composite thin films.

MD-Fe

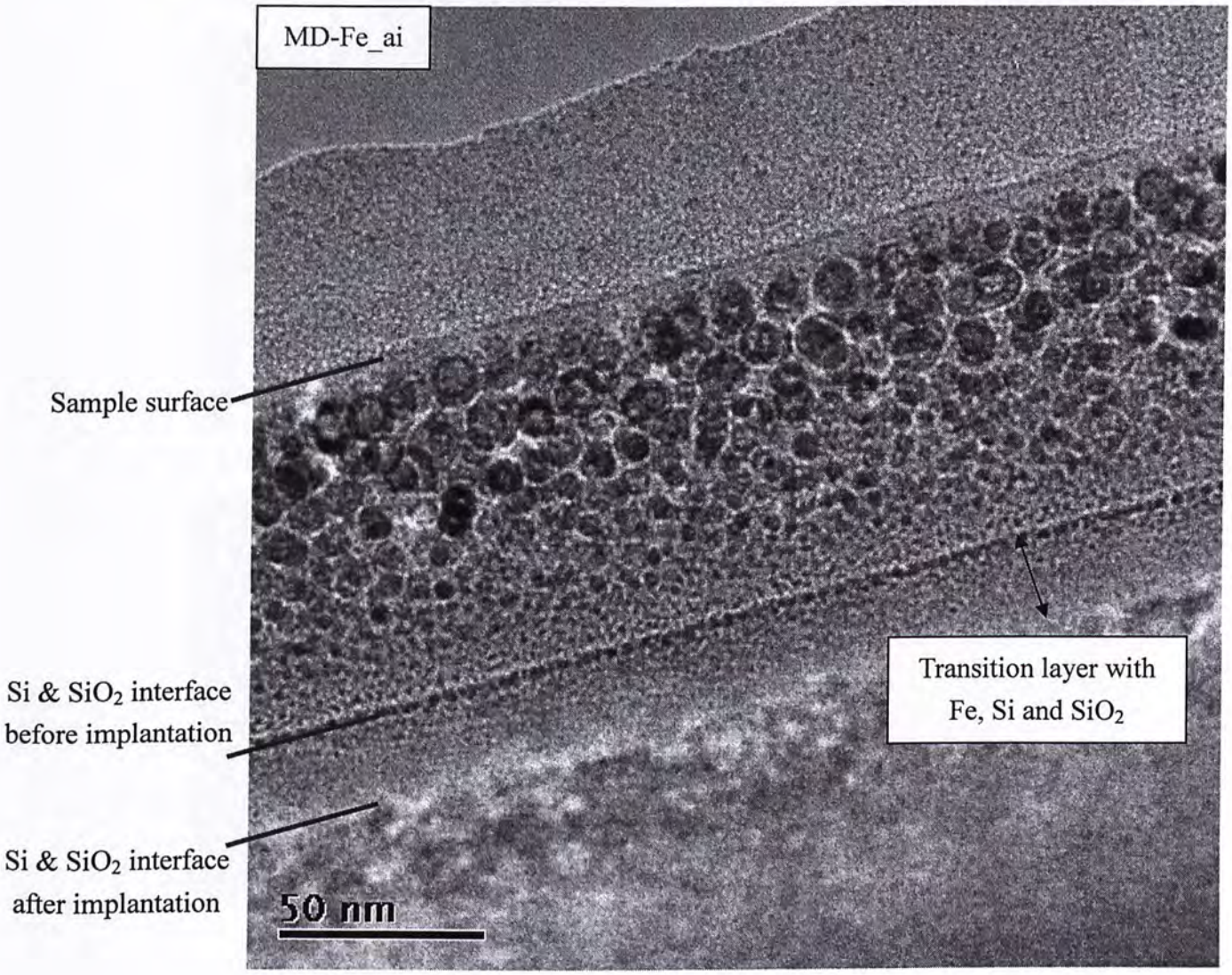

Figure 4.17 TEM image of as-implanted MD-Fe

As shown in the above picture, the Si and SiO_2 interface retreat towards the Si substrate. Although the TRIM simulation confirms that the implantation energy is enough for the implanted atoms to penetrate the SiO_2 layer, it cannot predict the

retreat of the SiO_2 layer. This layer also acts as a transition layer for the C-AFM and the field emission measurement. Moreover, the Fe clusters are embedded under the smooth sample surface. Therefore, the samples are resistive to the C-AFM measurement since the sample surface is not conductive.

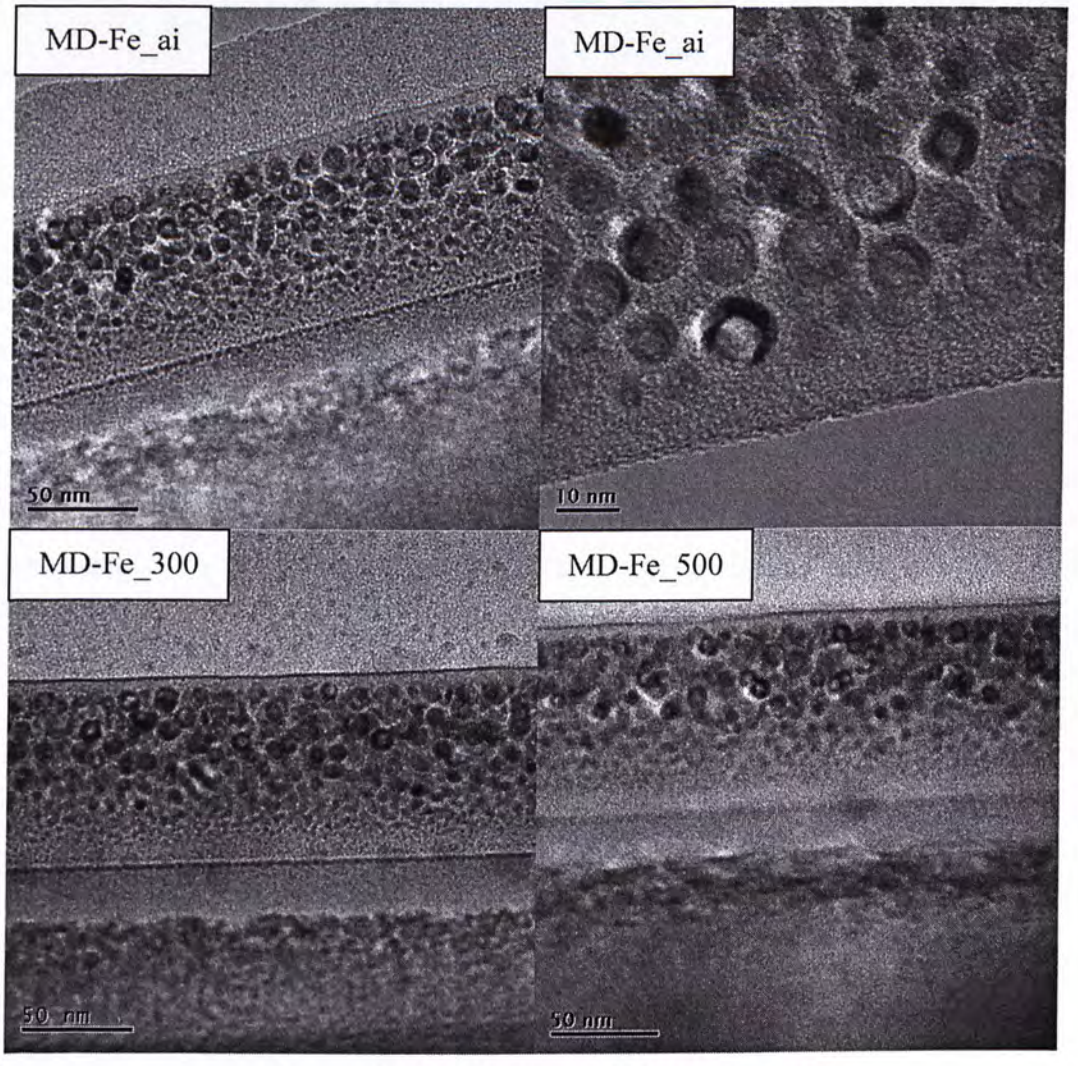

Figure 4.18 TEM images of MD-Fe samples

As the annealing temperature increases, the Fe atoms move towards to the sample surface and this widens the transition layer which is also the transition layer.

HD-Fe

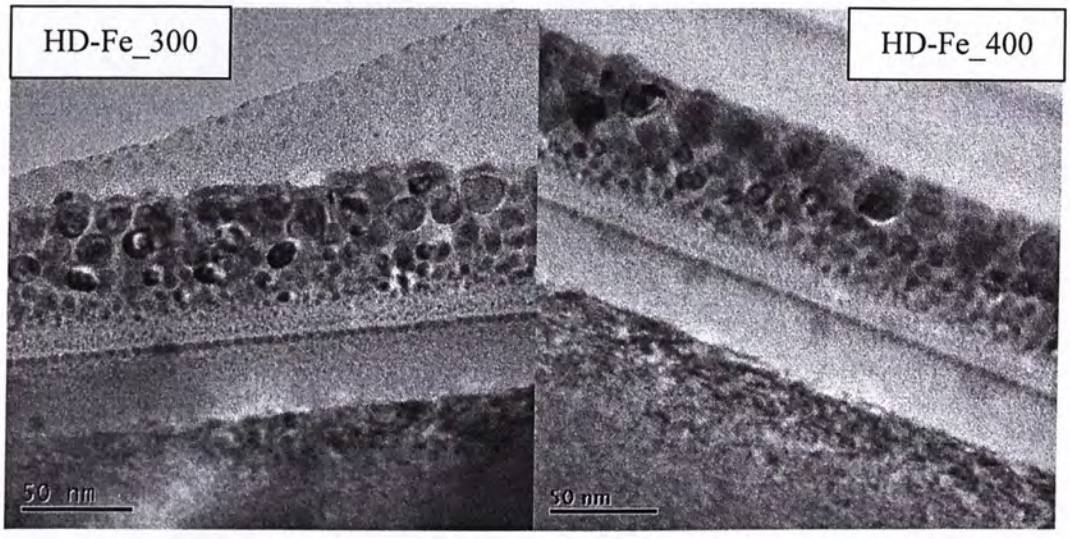

Figure 4.19 TEM images of HD-Fe samples

For the HD-Fe samples, it is found that the Fe clusters expose at the surface of the samples. The surface is much rougher to the MD-Fe samples and this is consistent with the AFM images. In addition, the Fe clusters present in the HD-Fe samples are larger than that of the MD-Fe samples and there also exists a transition layer. This transition layer becomes wider compared with the MD-Fe samples since the HD-Fe samples are implanted with larger dosage and longer implantation time.

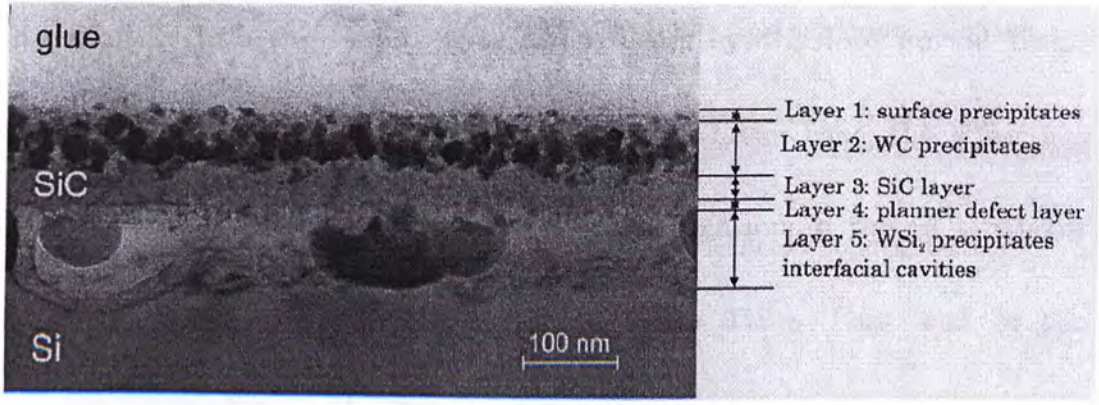

Figure 4.20 TEM images of HD-Fe samples

Figure 4.20 shows the TEM image of a RTA treated tungsten implanted silicon carbide prepared by W. M. Tsang. As shown in the figure, the surface layer contains the small metal cluster with diameter ranging from 2nm to 10nm. Below the topmost layer, it is the polycrystalline WC layer with thickness approximately equals to 50nm and followed by a 50nm thick beta-SiC layer. There are also some large WSi_2 precipitates at the interface between the planner defect layer and the Si substrate. Unlike the SiO_2 in our sample, beta-SiC is electrically conductive with resistivity ranging from 4.4Ωcm to 5.7Ωcm [57]. Moreover, the surface layer is composed of many small metal grains which make the sample surface electrically conductive for the C-AFM measurement.

Apart from the surface morphology and the electrical inhomogeneity, there is another field enhancement mechanism, which is related to the internal structure of the dielectric, proposed by W. M. Tsang. It is called the proximity field enhancement effect which is shown in Figure 4.21.

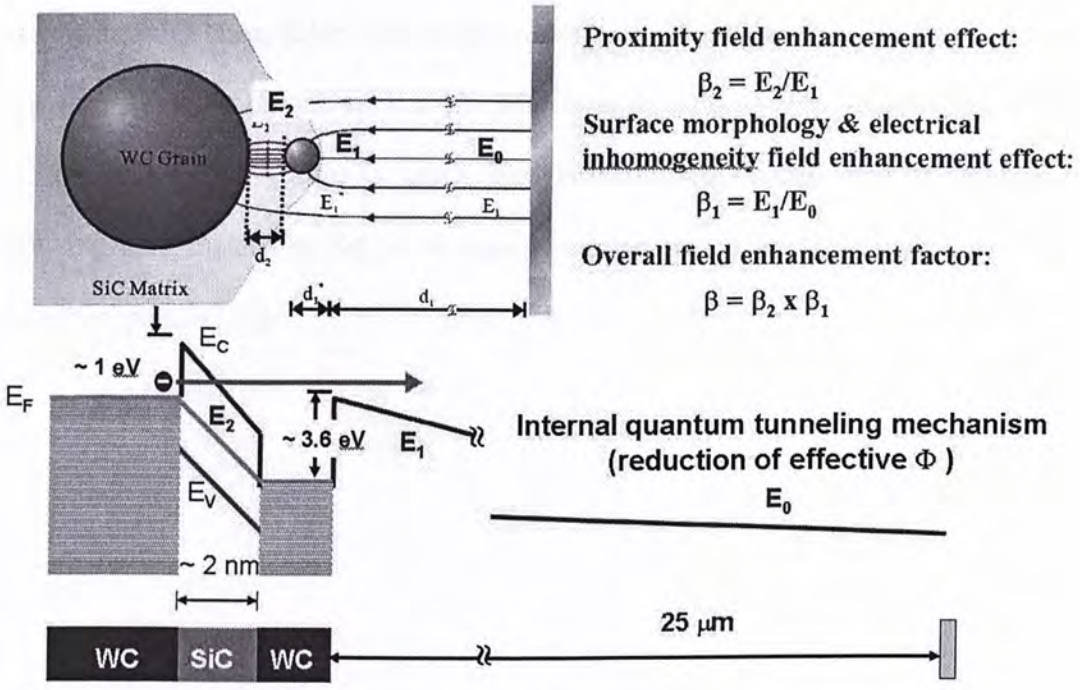

Figure 4.21 Proximity field enhancement effect

This extra enhancement is based on the electric field between the WC clusters. As shown in the TEM image, the WC clusters located at the surface are smaller than those below them. A strong electric field will set up between these WC clusters inside the SiC matrix with thickness approximately equal to 2nm. Consider the electrons on the surface WC clusters, the energy barrier is the work function of the WC which is about 3.6eV with thickness about 25μm. On the contrary, the electrons at the larger WC cluster are more energetic then those on the surface WC clusters and the electrons only need to overcome the energy barrier created by SiC which is about 1eV and the tunneling distance is only 2nm and this kind of internal structure contributes to the field enhancement. A turn-on field of about 0.35V/μm and a field enhancement of 5500 are recorded. Compared to this SiC sample, similar structure is found in the nano-composite samples. But SiO_2 is an insulator with a much wider band gap compared with SiC. Therefore, this model is not applicable to our samples. Nevertheless, SiO_2 is chosen as a dielectric in this project because its fabrication

process is fully compatible with existing integrated circuit technology and this is an important issue for device application. Moreover, compared with SiC, the fabrication of high quality SiO_2 film is much simpler and time saving. Another reason of choosing SiO_2 instead of SiC is to avoid the formation of metal silicides and other undesired phases [58].

4.4.4 Field emission properties of annealed Fe-SiO_2

All the annealed samples were taken for field emission measurements. Among all the samples, MD-Fe_300 showed an ultra low turn-on field and a very large field enhancement factor. But this excellent field emission performance was lost in the third measurement.

MD-Fe_300

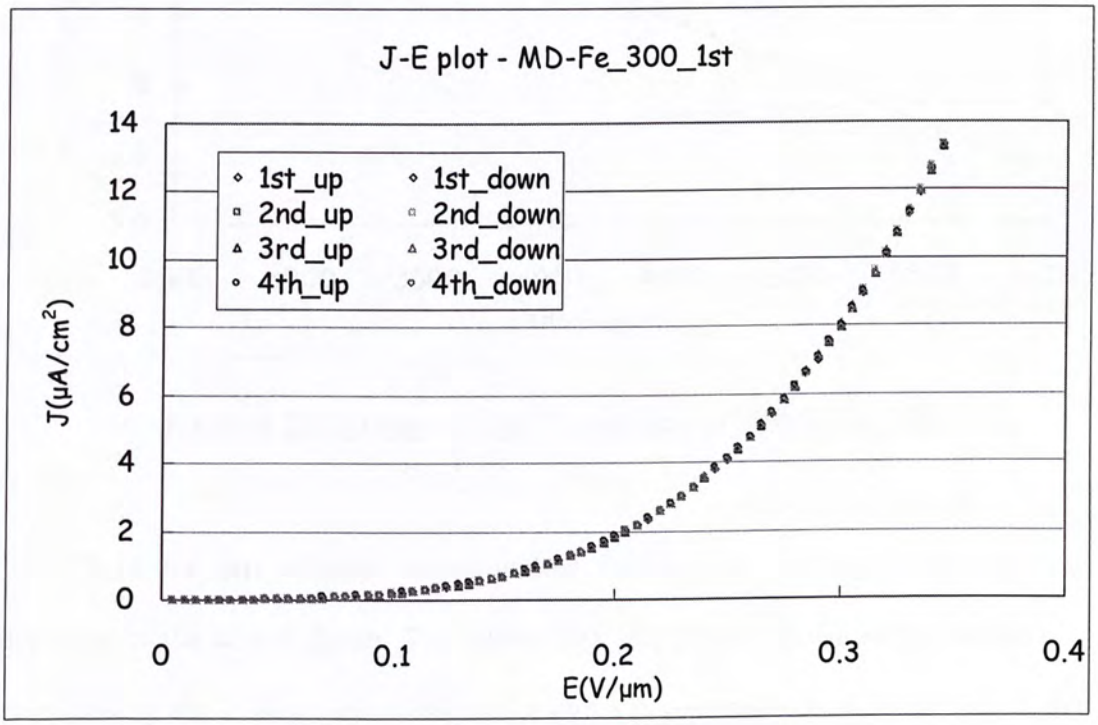

Figure 4.22 *J-E* plots of the 1st measurement of MD-Fe_300

The following figure is the *F-N* plot. It is found that the sample has an average β value equaled to 25800.

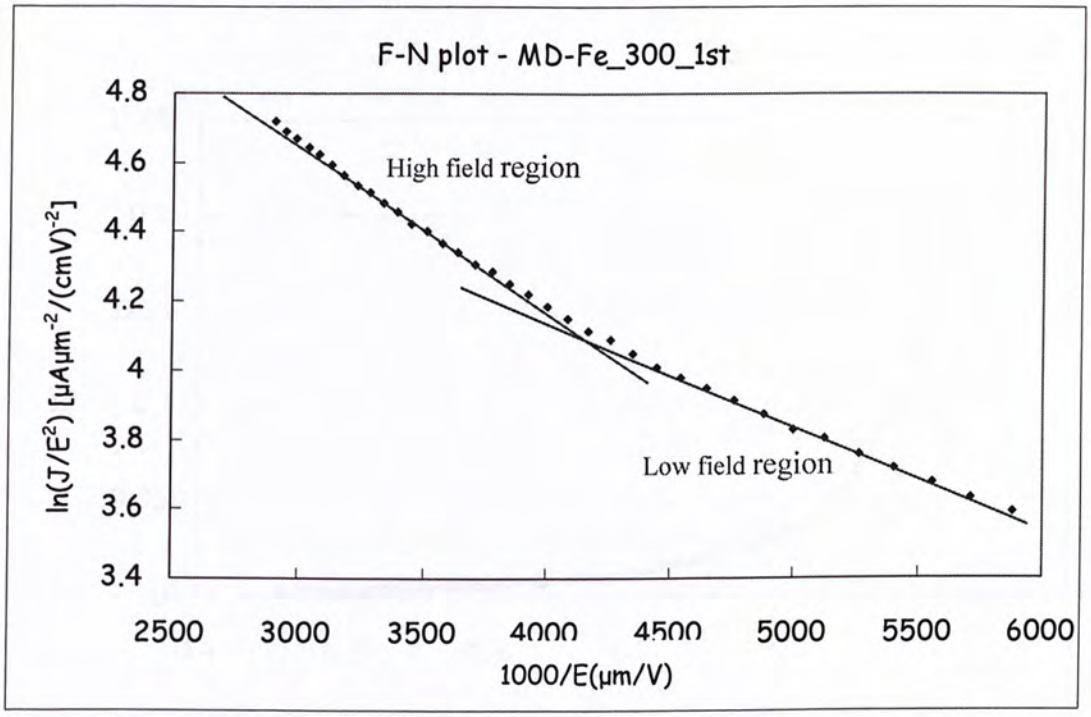

Figure 4.23 *F-N* plots of the 1st measurement of MD-Fe_300

There are two different slopes at low field region and high field region as depicted in the above figure. The curve does not follow the linear dependence as predicted by the F-N model. If the above curve is repeatable with same slopes, that means there is another mechanism which contributes to the electron emission other than the F-N model. One of the possible explanations for the derivation is the surface morphology [59-61].

In the 1st measurement, mica spacers with 20nm and a Cu anode was used. For the 2nd measurement, 44nm mica spacers were used together with an ITO/Glass anode.

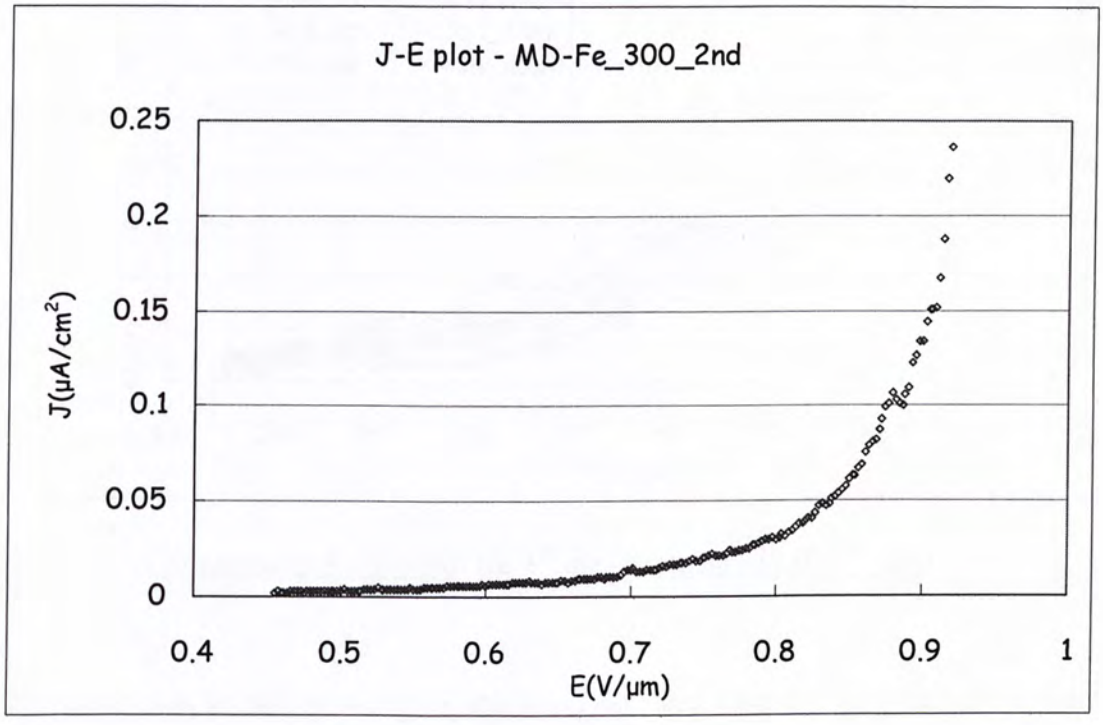

Figure 4.24 *J-E* plots of the 2nd measurement of MD-Fe_300

The 2nd measurement also showed an excellent field emission. Compared with the first measurement, the turn-on field was slightly retarded. To further investigate this sample, a 3rd measurement was taken with 42 nm mica spacers.

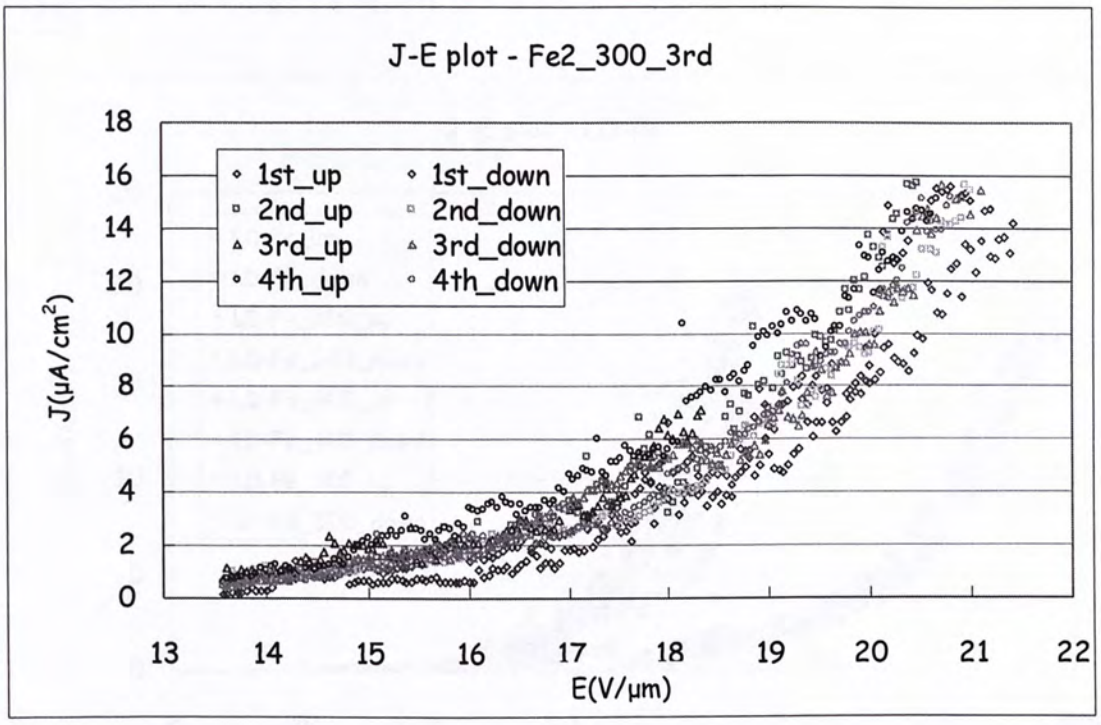

Figure 4.25 *J-E* plots of the 3rd measurement of MD-Fe_300

As shown in the above figure, the excellent field emission performance is lost. This implies that the field emission measurement will affect the sample's properties causing the lost of the excellent performance.

LD-Fe

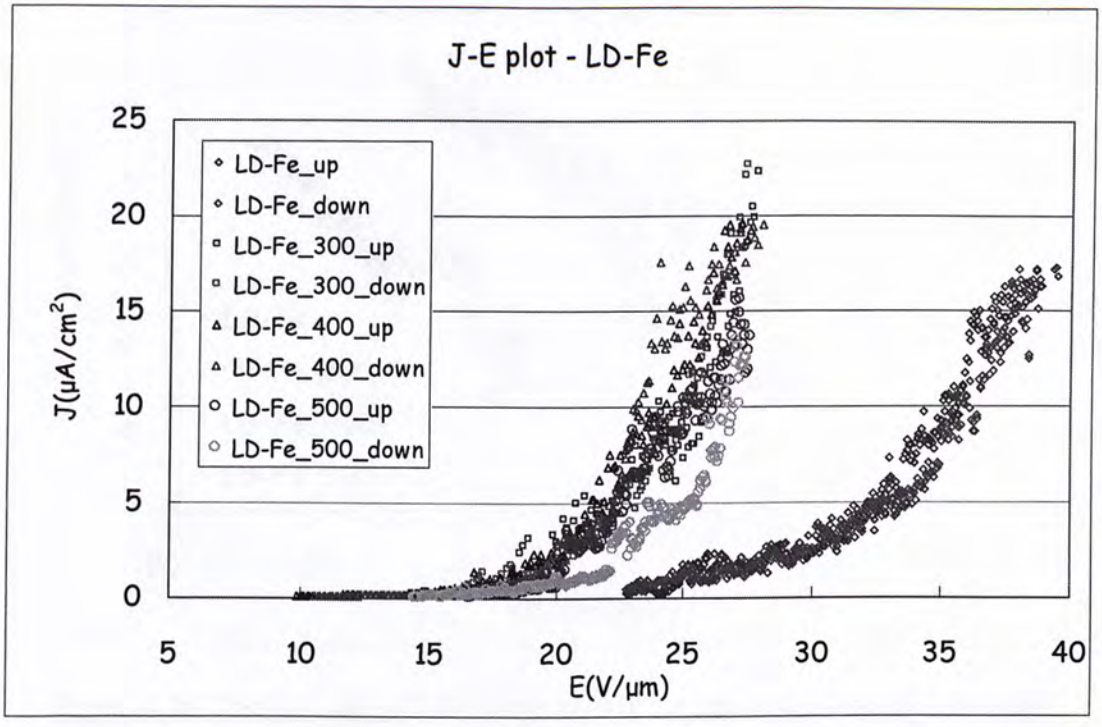

Figure 4.26 The *J-E* plot of LD-Fe samples at various annealing temperatures

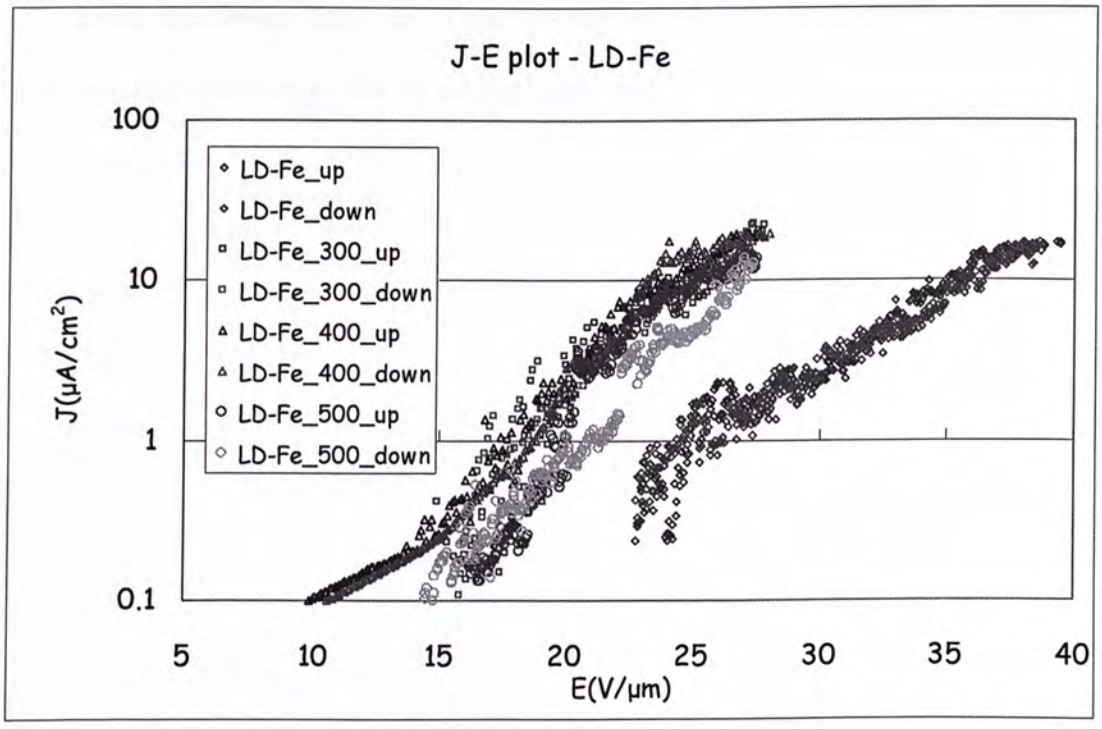

Figure 4.27 The *J-E* plot of LD-Fe samples at various annealing temperatures in log scale

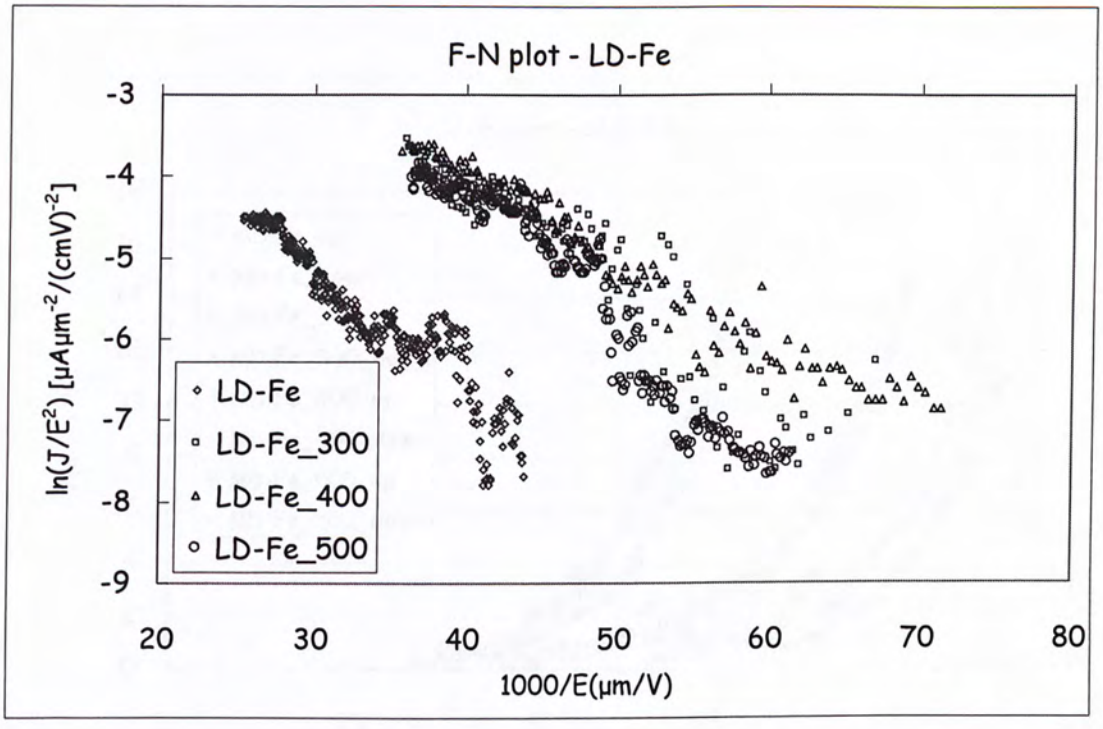

Figure 4.28 The *F-N* plot of LD-Fe samples at various annealing temperatures

From the above figure, RTA can further improve the turn-on field of the low dose samples compared with the as-implanted one.

MD-Fe

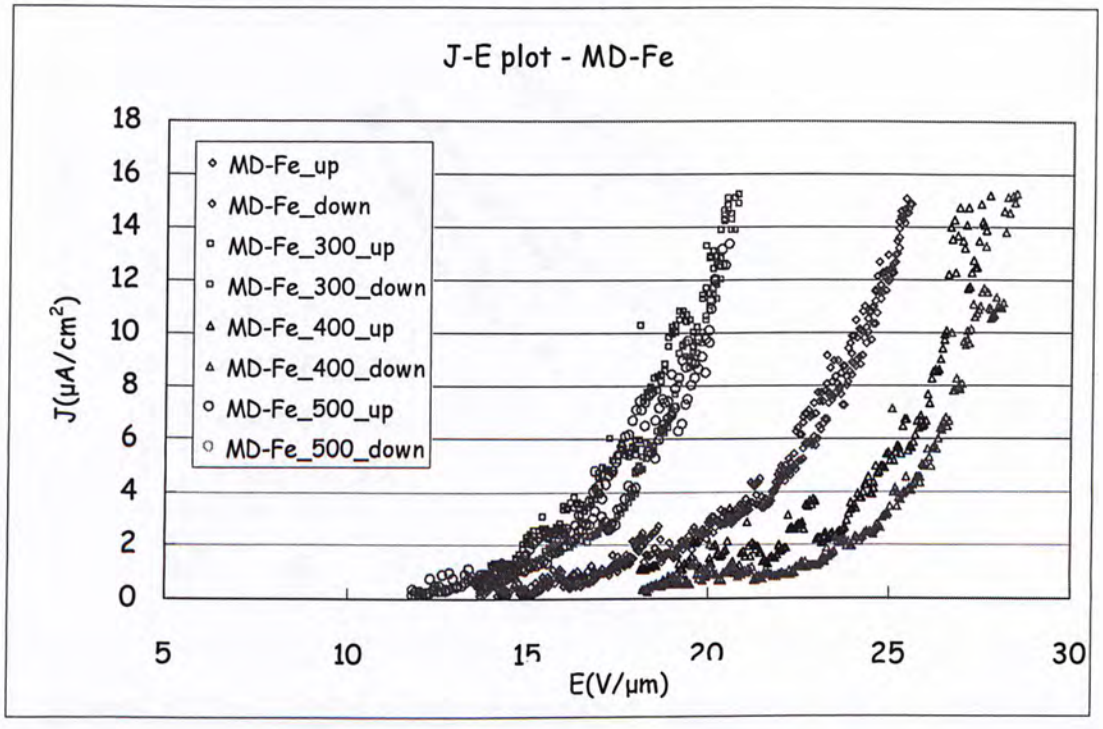

Figure 4.29 The *J-E* plot of MD-Fe samples at various annealing temperatures

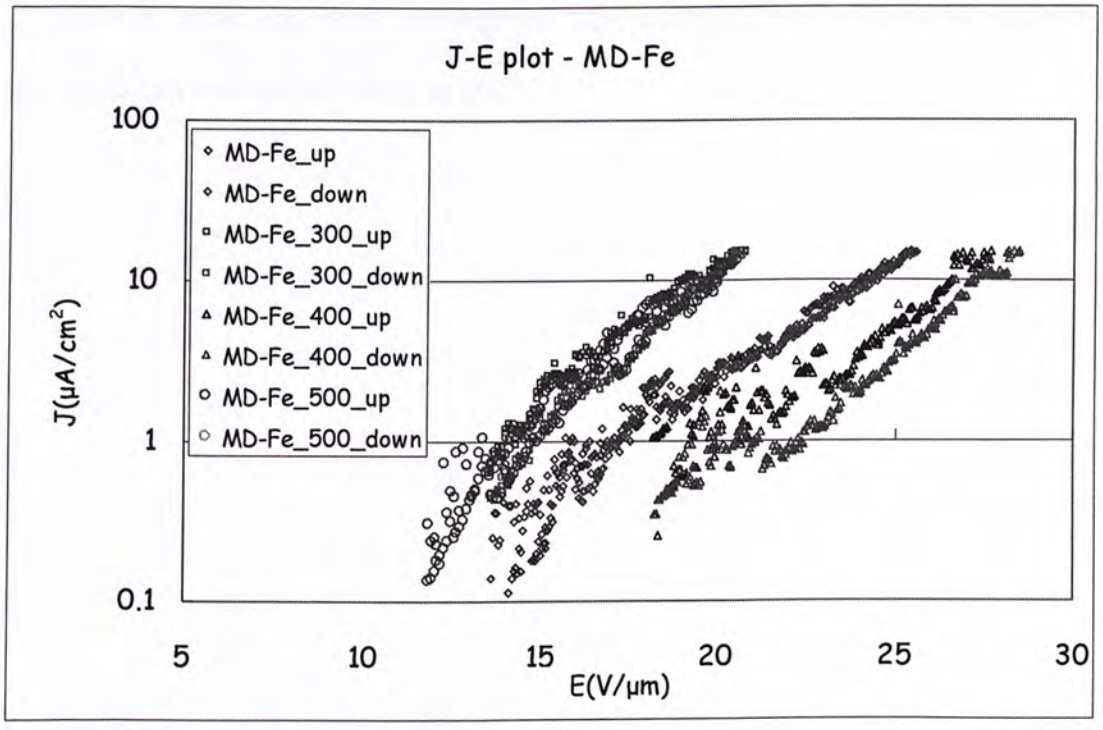

Figure 4.30 The *J-E* plot of MD-Fe samples at various annealing temperatures in log scale

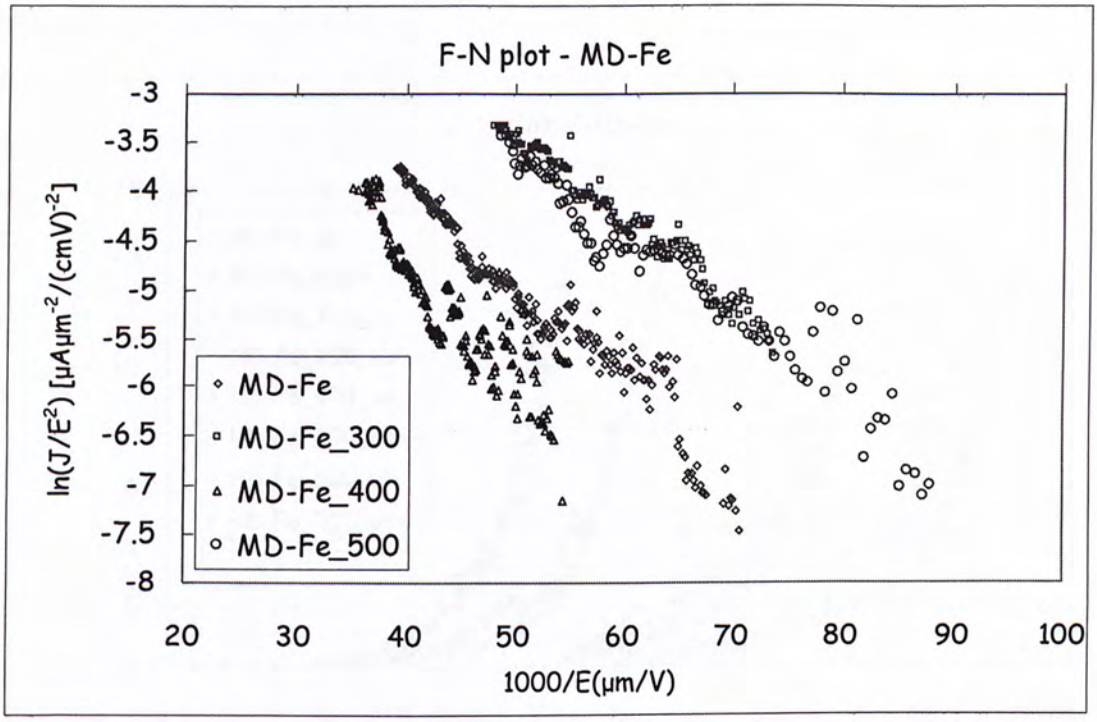

Figure 4.31 The *F-N* plot of MD-Fe samples at various annealing temperatures

RTA at 300°C and 500°C can improve turn-on field of the MD-Fe set of samples. But this is not true for annealing at 400°C.

HD-Fe

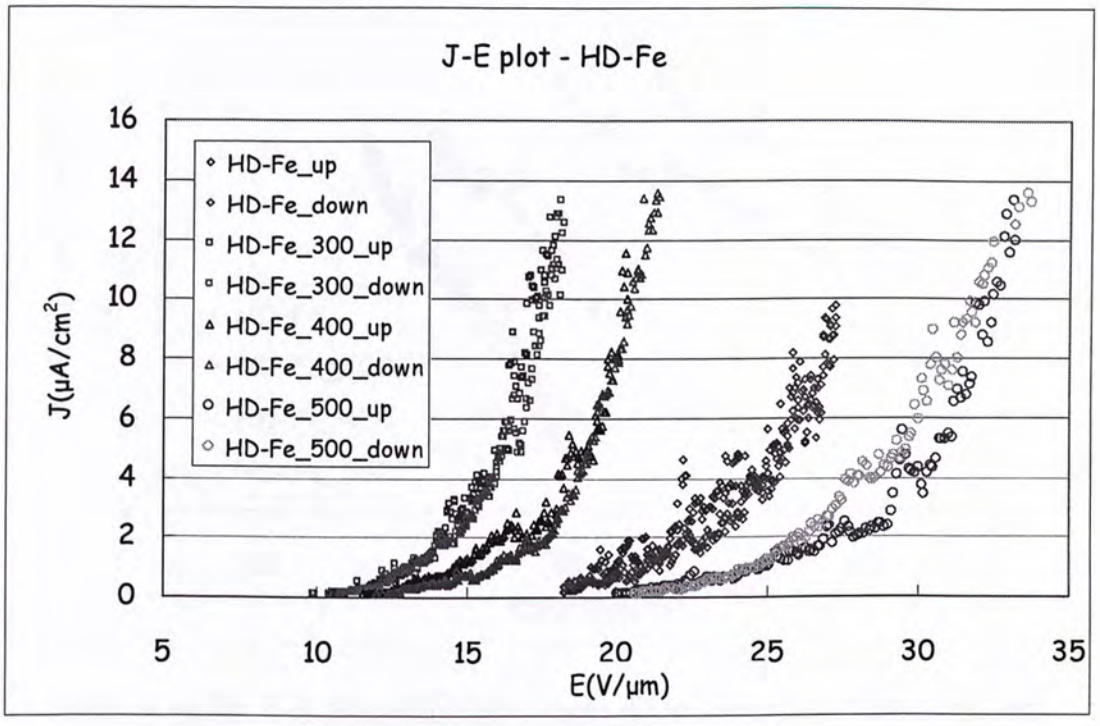

Figure 4.32 The *J-E* plot of HD-Fe samples at various annealing temperatures

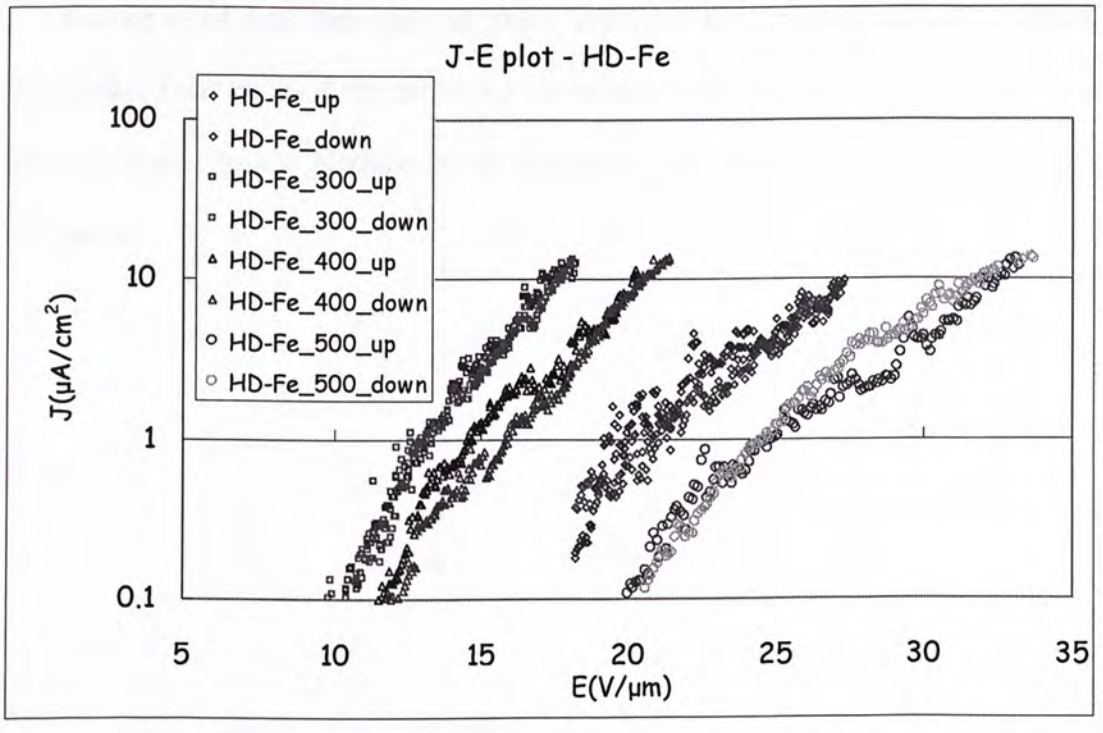

Figure 4.33 The *J-E* plot of HD-Fe samples at various annealing temperatures in log scale

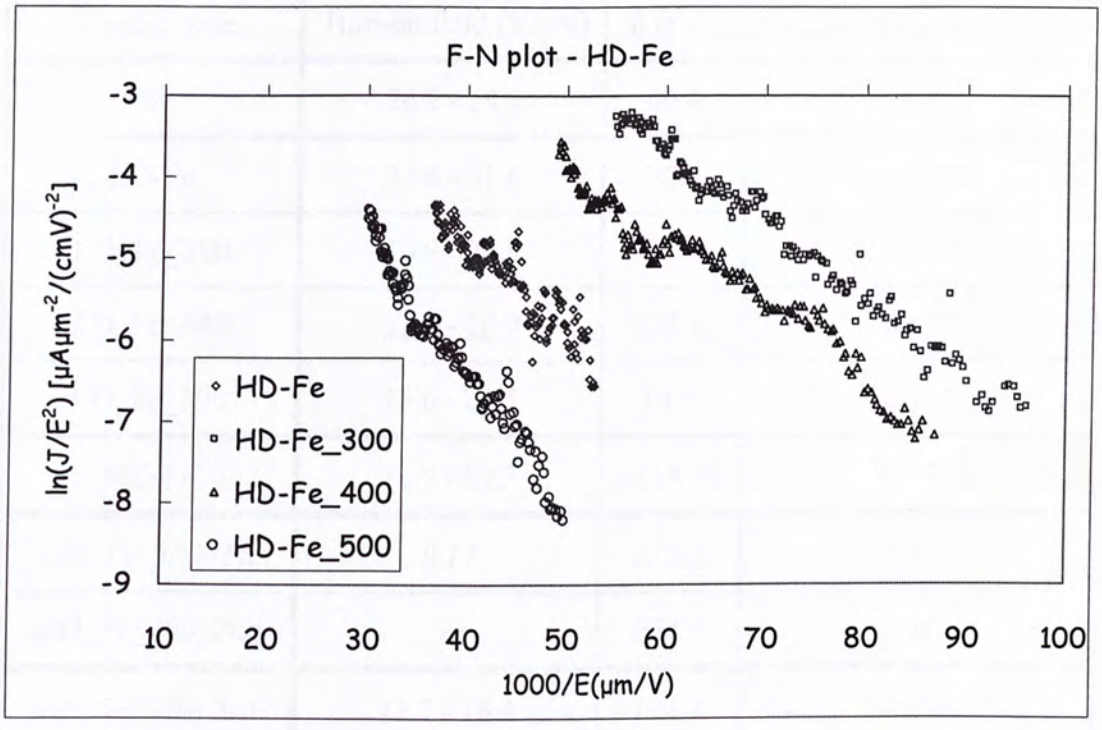

Figure 4.34 The *F-N* plot of HD-Fe samples at various annealing temperatures

For the HD-Fe set, annealing at 300oC can lower the turn-on field to 12.6 V/μm. But further increasing of the annealing temperature will not give better results. This may be caused by the broaden of the transition layer as the annealing temperature increases.

Sample code	Turn-on field (V/μm)	β (a.u.)	Surface roughness (nm)
Si	26.2 - 29.5	60.4	NA
LD-Fe	24.8 - 31.6	76.9	0.372
LD_Fe_300	16.9 - 20.9	76.3	0.213
LD_Fe_400	12.6 - 20.0	100.6	0.579
LD_Fe_500	15.6 - 22.5	61.4	0.147
MD-Fe	16.9 - 19.3	115.7	0.540
MD_Fe_300_1st	*0.17*	*25800*	*0.648*
MD_Fe_300_2nd	*NA*	*964.5*	*0.648*
MD_Fe_300_3rd	13.7 - 16.4	124.2	0.648
MD_Fe_400	18.3 - 23.4	91.6	1.374
MD_Fe_500	13.4 - 15.7	131.0	0.217
HD-Fe	19.1 - 22.5	108.5	2.894
HD_Fe_300	12.6 - 13.9	92.5	2.556
HD_Fe_400	14.1 - 16.3	93.0	3.566
HD_Fe_500	23.1 - 25.1	56.0	1.302

Table 4.6 Field emission results of all the Fe implanted samples

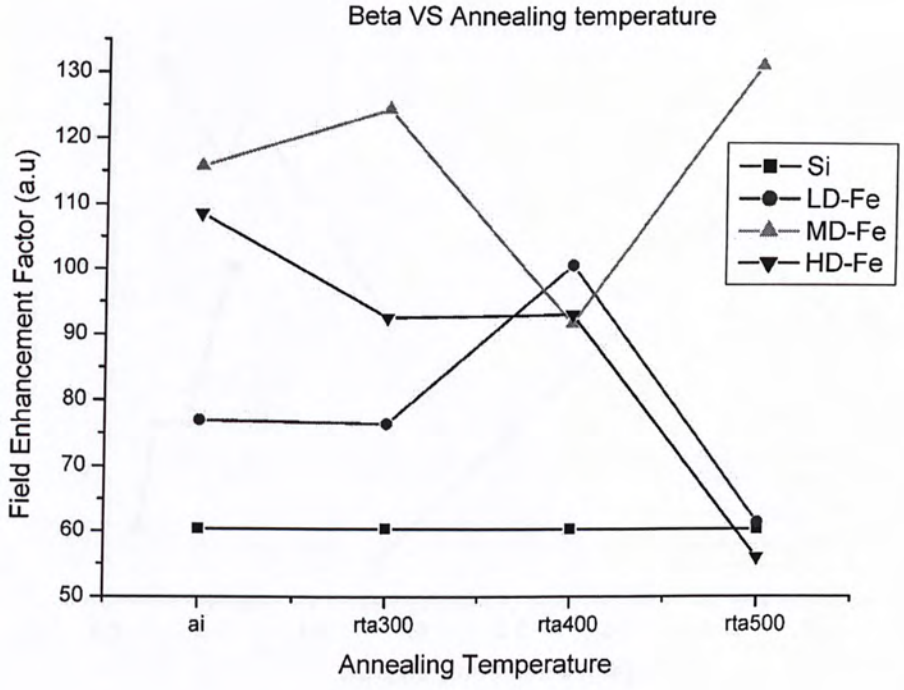

Figure 4.35 Beta VS annealing temperature

Consider only the consistent results, it is found the MD-Fe set of samples shows a generally better field emission properties compared with the others. And for the LD-Fe as well as HD-Fe sets, a too high annealing temperature will lead to a poor field emission performance while the MD-Fe_500 shows the best result.

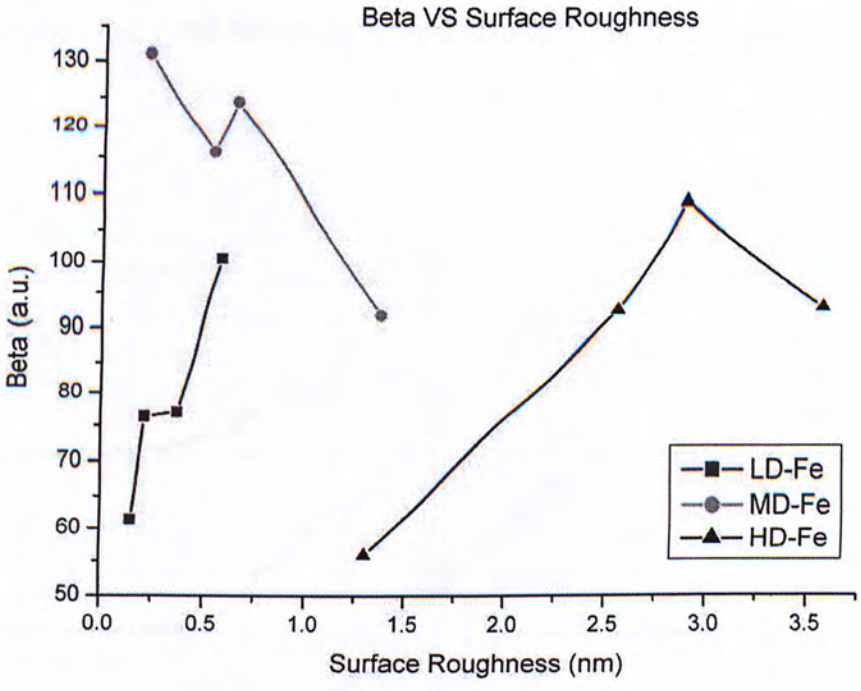

Figure 4.36 Beta VS surface roughness

Figure 4.31 shows the relationship between the field enhancement factor and the surface roughness. It clearly indicates that the beta value does not depend on the surface roughness and so there should be other factors controlling the field enhancement mechanism.

4.5 Step-like and jump-like features in the *J-E* plots

Step-like and jump-like features were also found in the *J-E* plots of the Fe-SiO_2 samples.

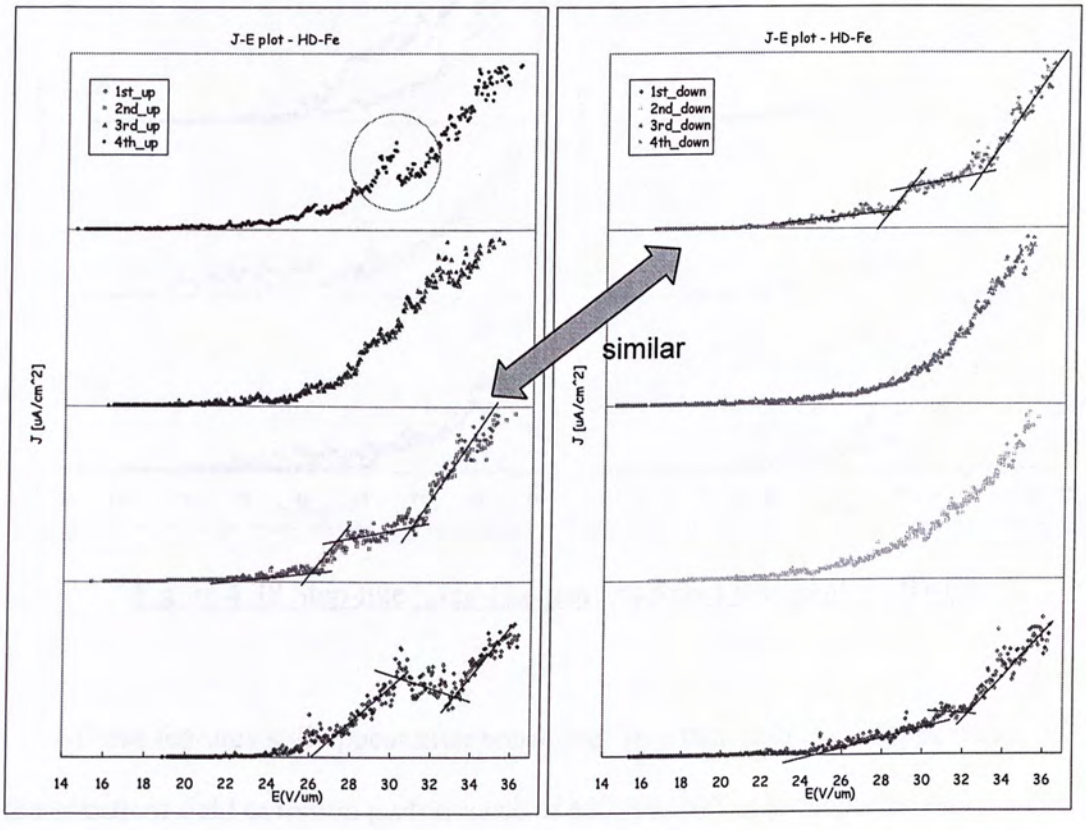

Figure 4.37 Step-like jump-like features found in HD-Fe

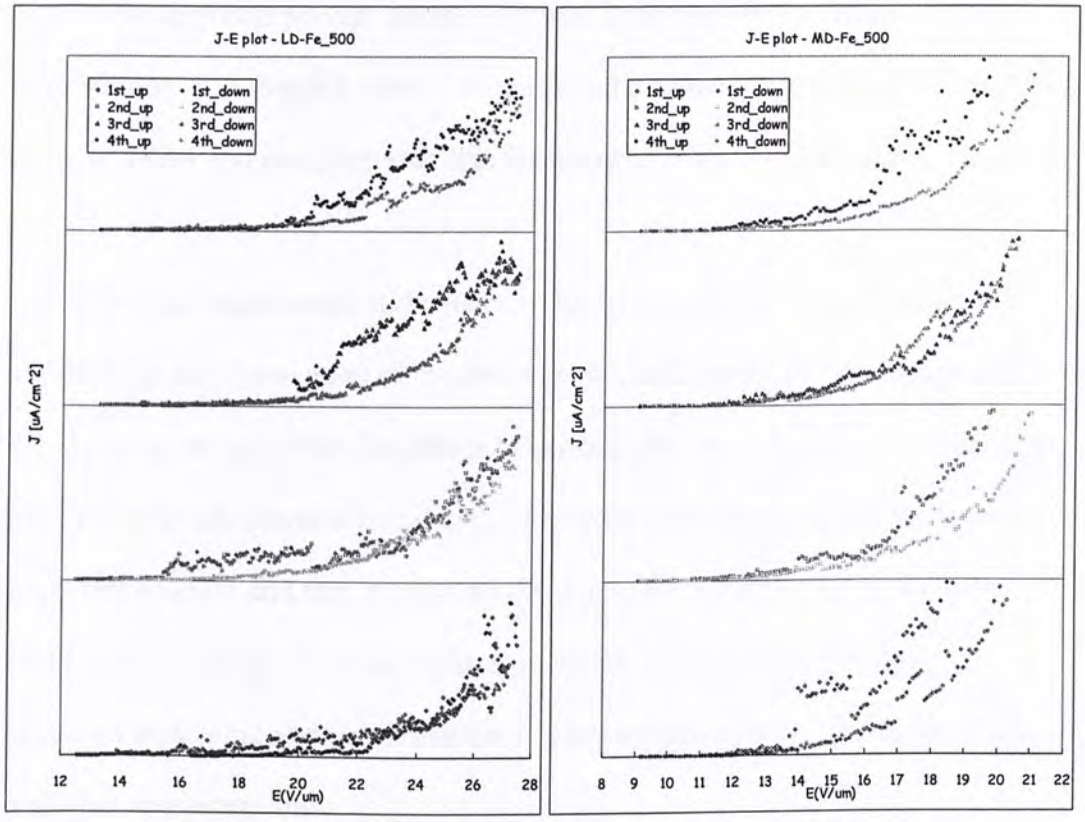

Figure 4.38 Step-like jump-like features found in annealed HD-Fe

These features still appear after annealing. Together with the disappearance of the excellent field emission performance of MD-Fe_300, it is suspected that the field emission properties might be modified by the local self- annealing or other effects during the field emission measurement.

Another speculation for the step-like features is the coulomb blockade [55]. Coulomb blockade is the increase in resistance of a tunnel junction due to a single electron charge up. In a nano-composite thin film, each nano-cluster acts as a small tunnel junction with a very small capacitance. Microscopically, the current flow is a series of events of an electron passing through those small tunnel junctions. If the capacitance of the tunnel junction is small enough, the voltage builds up at the junction will be significant even only it is charged by one single electron. This

buildup voltage will prevent another electron from tunneling and leads to an increase in resistance. The flowing current is suppressed because the resistance of the device is not constant and results in step-like features present in the *J-E* characteristics.

Since the capacitance of the junction has to be very small, the temperature required for the observation of the coulomb blockade has to be low enough such that the charging energy at the junction is larger than the thermal energy. According to ref. [55], the step-like features found in the *J-E* characteristics are poorly observable in room temperature and they are not regular due to the instability of the emission process and burning out of the emitting material. This matches with the local-self-annealing and the formation of new conducting paths during the field emission measurement.

4.6 Field Emission Images

The following images show the discharge of electrons during the field emission. The sample was the MD-Fe_400.

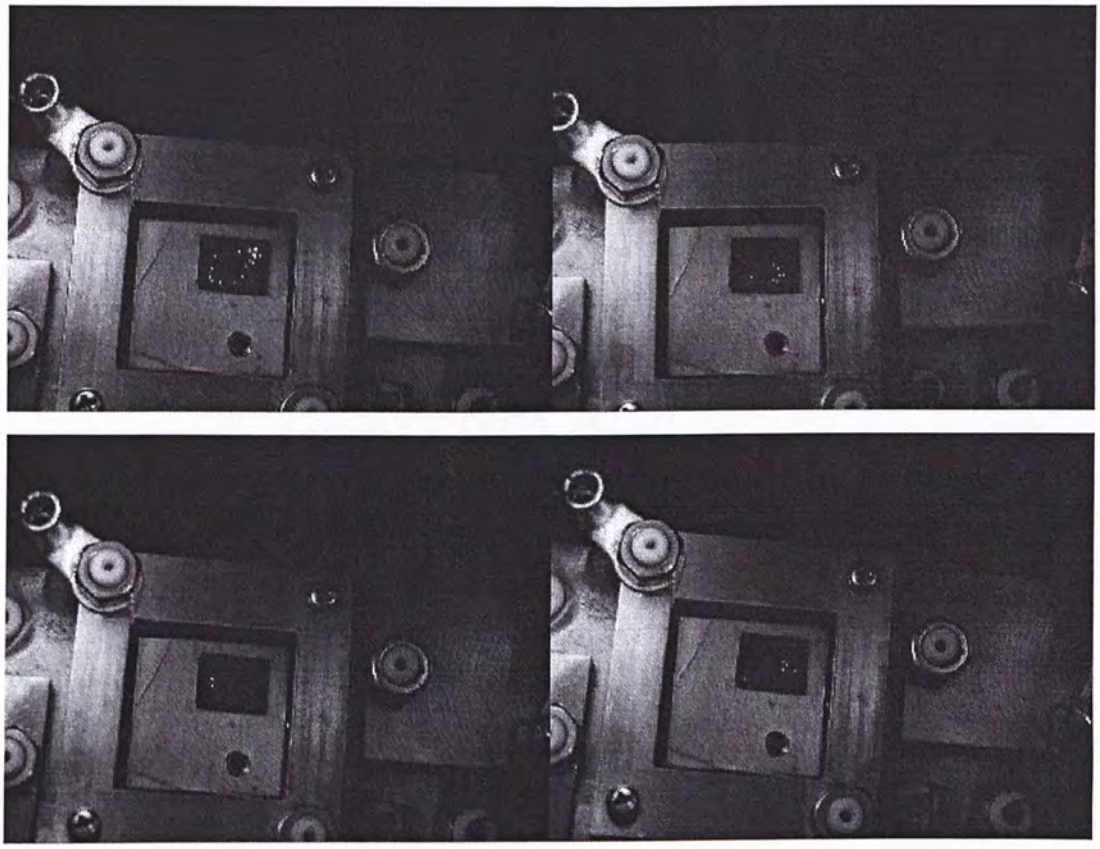

Figure 4.39 Field emission images of MD-Fe 400

As shown in the above images, it is found that the emission sites were localized and not coherent over the sample surface. This indicates that there are changes on the emission sites during the field emission measurements. These changes are the evidences to support the local self-annealing and the formation of new conducting paths which were proposed in chapter 3.

4.7 Chapter summary

In this chapter, the field emission properties of the Fe-SiO_2 samples were studied. The RTA treatment modified the field emission properties of the. From the C-AFM images, it indicated that the preparation of the metal dielectric nano-composite thin films in this project did not posses any observable difference in electrical inhomogeneity among the MD-Fe samples. In fact, all the samples were quite "resistive" to as shown in the CAFM images. The reason was clearly shown from the TEM micrographs. It is because the Fe clusters were embedded under the sample surface. Moreover, there existed a transition layer between the nano-composite thin film and the Si substrate this implied that the surface of the sample was not well connected to the Si substrate and the electrons need to tunnel through this layer before emitted from the sample surface.

Besides, the field emission images showed that the emission sites were localized and not coherent over the sample surface. This implied that the sample was being modified during the field emission measurement. The possible reasons were the local self-annealing and the formation of new conducting paths caused by the emission current during the measurement. And these can also account for the step-like and jump-like features found in the *J-E* plots.

For the field emission properties, the 1st measurement of MD-Fe_300 showed an ultra low turn-on field which was about 0.17 V/μm and an extreme large field enhancement factor equaled to 25800. But these excellent properties were lost gradually as the sample underwent more measurements.

The above results also showed that rapid thermal annealing can be a modification on the metal dielectric nano-composite materials in order to enhance the field emission performance. But the implantation dose, the annealing temperature and the implantation energy should be optimized to avoid the formation of the transition layer.

Conclusion

In this project, the metal dielectric nano-composite thin films were prepared by MEVVA ion implantation and the samples were then treated by RTA. An ultra low turn-on field which was 0.17 V/μm and an extreme large field enhancement which equaled 25800 were obtained in one of the annealed samples. Compared with the ion beam synthesized SiC samples [24], the turn-on field of the samples with doses equaled to $0.75\times10^{18}cm^{-2}$, $1\times10^{18}cm^{-2}$and $1.2\times10^{18}cm^{-2}$ were 28, 12 and 15 respectively. These values were close to the typical values obtained for the metal-dielectric nano-composite thin films prepared in this project with much less implantation dosage. Furthermore, the field emission properties can be improved by reducing the thickness of the transition layer or even remove the transition layer.

Step-like and jump-like features were found in the *J-E* plots and this indicated that there were changes occurred in the samples during the field emission measurement.

Refer to the AFM images, RTA had a strong influence on the surface roughness of the samples.

From the CAFM images, a few of the conducting grains can be matched to the protrusions found on the corresponding AFM images. But in general, all the samples including the as-implanted and the annealed samples were all resistive to the CAFM. This is because the Fe clusters were embedded under the sample surface.

From the TEM micrographs, it was clearly shown that there were nano-size Fe metal clusters and there existed a transition layer between the sample surface and the Si substrate. These metal atoms moved towards the sample surface and the transition layer was broadened as the annealing temperature increased. This effect was more obvious at the high dose samples due to the larger nominal dose and longer implantation time. The formation of the transition layer and its thickness will definitely affect the field emission properties of the samples.

The field emission projection images showed that there were tiny emissions sites which were not sustainable to the field emission measurement. In addition, these emission sites varied in position as the measurement proceed. Two models were proposed and they were the local self-annealing and the formation of new conducting paths due to the field emission current.

To conclude, the implantation dose, the implantation energy and the annealing conditions are very important to the field emission performance of the metal-dielectric nano-composite thin film and should be optimized. By fine tuning and controlling these factors, an ultra low and extreme large field enhancement could be achieved for ultra fast vacuum microelectronic devices and display applications.

Future Plan

Several modifications can be made in order to improve the field emission performance of the metal-dielectric nano-composite thin film. First of all, the extraction voltage for the metal ion implantation should be increased to guarantee the implanted atoms can penetrate the dielectric layer. Secondly, the SiO_2 dielectric layer can be replaced by other materials with smaller band gap such that the proximity field enhancement can be applied. Possible candidate is ZnO which has a band gap equaled to 3.37eV [62]. Boron nitride is another promising material as it possesses negative electron affinity [63]. Other materials such as GaN [64], TiO_2 [65] and diamond like carbon film [66] are all versatile dielectric materials. Finally, since both Fe and Co are magnetic materials, the application of a magnetic field during the field emission, which may lead to the emission of spin-polarized electrons, would be an interesting topic for further study.

[1] W. Zhu, Vacuum Microelectronics, John Wiley & Sons Inc., 2001.

[2] K. B. K. Teo, E. Minoux, L. Hudanski, F. Peaguer, J. P. Schnell, L. Gangloff, P. Legagneux, D. Dieumegard, G. A. J. Amaratunga, and W. I. Milne, Nature (London) 437, 968 (2005).

[3] M. Geis, J. C. Twichell, J. Macaulay, and K. Okano, Appl. Phys. Lett. 67, 1328 (1995).

[4] A. T. Sowers, B. L. Ward, S. L. English, and R. J. Nemanich, J. Appl. Phys. 86, 3973 (1999).

[5] X. Z. Ding, Y. J. Li, Z. Sun, B. K. Tay, S. P. Lau, G. Y. Chen, W. Y. Cheung, and S. P. Wong, J. Appl. Phys. 88, 6842 (2000).

[6] J. D. Carey, R. D. Forrest, R. U. A. Khan, and S. R. P. Silva, Appl. Phys. Lett. 77, 2006 (2000).

[7] J. D. Carey, R. D. Forrest, and S. R. P. Silva, Appl. Phys. Lett. 78, 2339 (2001).

[8] A. Ilie, A. C. Ferrari, T. Yagi, and J. Robertson, Appl. Phys. Lett. 76, 2627 (2000).

[9] W. I. Milne, A. Ilie, J. B. Cui, A. Ferrari, J. Robertson, Diamond Relat. Mater. 10, 260 (2001).

[10] J. Robertson, Mater. Sci. Eng.., R. 271, 1 (2002).

[11] W. M. Tsang, S. J. Henley, V. Stolojan, and S. R. P. Silva, Appl. Phys. Lett. 89, 193103 (2006)

[12] Y. J. Li, Z. Sun, S. P. Lau, G. Y. Chen, and B. K. Tay, Appl. Phys. Lett. 79, 1670 (2001).

[13] Y. Chen, D. T. Shaw, and L. Guo, Appl. Phys. Lett. 76, 2649 (2000).

[14] D. Chen, S. P. Wong, W. Y. Cheung, W. Wu, E. Z. Luo, J. B. Xu, and I. H. Wilson, Appl. Phys. Lett. 72, 1926 (1998).

[15] D. Chen, W. Y. Cheung, S. P. Wong, Y. M. Fung, J. B. Xu, I. H. Wilson, and R. W. M. Kwok, J. Vac. Sci. Technol. A. 17, 2019 (1999)

[16] D. Chen, S. P. Wong, W. Y. Cheung, and J. B. Xu, Solid State Commun. 128 (2003), p.435-439.

[17] W. M. Tsang, S. P. Wong, and J. K. Lindner, Appl. Phys. Lett. 81, 3942 (2002).

[18] W. M. Tsang, S. P. Wong, and J. K. Lindner, Appl. Phys. Lett. 84, 3193 (2004).

[19] W. M. Tsang, V. Stolojan, S. P. Wong, B. J. Sealy, S. R. P. Silva, Mater. Sci. Eng. B 124-125 (2005) p.453-P.457.

[20] W. M. Tsang, V. Stolojan, C. Giusca, C. H. P. Poa, B. Sealy, and S. R. P. Silva, J. Vac. Sci. Technol. B. 24(2), 958 (2006).

[21] Funaki Y, Mochizuki Y, Flat panel market to 10 trillion yen by 2010. Mikkei Microdevices, Flat panel display yearbook, InterLingua, Redondo Beach, California USA, 1999, p.75.

[22] R. H. Fowler and L. W. Nordheim, Proc. R. Soc (London) A119, 173 (1928).

[23] B. H. Bransden and C. J Joachain, Quantum Mechanics, 2nd ed., Prentice Hall, 2000.

[24] W.M. Tsang, MPhil. Thesis, Department of Electronic Engineering, The Chinese University of Hong Kong, 2002.

[25] S. M. Sze, Physics of Semiconductor Devices, 2nd ed., Wiley: New York, 1981.

[26] C. A. Spindt, I. Brodile, L.Humphery, and E. R. Westerberg, J. Appl. Phys. 47, 5248 (1976).

[27] C. Wang, A. Garcia, D. C. Ingram, M. Lake, and M. E. Kordesch, Electronic Letters, 1991, 27, 1459-1461.

[28] S. R. P. Silva, R. D. Forrest, D. A. Munindradasa, and G. A. J. Amaratunga, Diamond and Rel. Mater., 1998, 7, 645-650.

[29] G. A. J. Amaratunga, and S. P. R. Silva, Appl. Phys. Lett., 1996, 68, 2529-2531.

[30] B. S. Satyanarayana, A. Hart, W. I. Milne, and J. Robertson, Appl. Phys. Lett., 1997, 71, 1430-1432.

[31] J. Robertson, Pure & Appl. Chem., 1994, 66, 1789-1796.

[32] J. U. Thiele, P. Kania, and P. Oelhafen, J. Vac. Sci. Technol. B, 1997, 15, 1739-1744.

[33] Y. L. Li, S. P. Lau, B. K. Tay, Z. Sun, G. Y. Chen, J. S. Chen, X. Z. Ding, and X. Shi, Appl. Phys. Lett., 2000, 77, 2021-2023

[34] S. Iijima, Nature, 1991, 354, 56-58.

[35] T. W. Ebbesen, and P. M. Ajayan, Nature, 1992, 358, 220-222.

[36] A. G. Rinzler, J. H. Hafner, P. Nikolaev, L. Lou, S. G. Kim, D. Tomanek, P. Nordlander, D. T. Colbert, and R. E. Smalley, Science, 1995, 269, 1550-1553.

[37] I. G, Brown, J. E. Gavin, and R. A. MucGill. Appl. Phys. Lett. 47, 358 (1985).

[38] G. Brown, B. Feibery and J. E. Gavin, J. Appl. Phys. 63, 4889 (1988).

[39] Jun Saaki and I. G. Brown, Rev. Sci. Instrum. 61, 586 (1990).

[40] G. Brown, Rev. Sci. Instrum. 65, 3061 (1994).

[41] J. Lindhard, M. Schariff, and H. E. Schiott, Kgl. Danske Videnskab., Selskab., Mat. Phys. Medd. 33, No. 14 (1963).

[42] J. F Ziegler, J. P. Biersack, and O. Littmark., "The stopping and Range of Ions in Solids", Vol. 1, Pergamon Press, Oxford, (1985).

[43] Operation Manual of the MEVVA ion source system in our lab.

[44] G. Binning, H. Rohrer, C. Gerber, and E. Weibel, Phys. Rev. Lett. 49, 57 (1982).

[45] G. Binning, C, Quate and C. Gerber, Phys. Rev. Lett. 56, 930 (1986).

[46] S. N. Magonov, M. H. Whangbo, "Surface analysis with STM and AFM: experimental and theoretical aspects of image analysis Wienhiem", N. Y.: VCH, (1996).

[47] W. K. Chu, J. W. Mayer, and M. A. Nicolet, Backscattering Spectroscopy, New York, Academic Press, 1978.

[48] M. Nastasi, J. W. Mayer, and J. K. Hirvonen, Ion Solid Interactions Fundaments and Applications, Cambridge solid state science series, New York, Cambridge University Press, 1996.

[49] M. Mayer, SIMNRA User;s Guide, Report IPP 9/133, Max-Planck-Institut fur plasmaphysik, Garching, Germany, 1997.

[50] P. R. Buseck, J. M. Cowely, and L. Eyring, "High-resolution transmission electron microscopy and associated techniques", Oxford University Press, (1998).

[51] P. B. Hirsch, A. Howie, R. B. Nicholson, D. W. Pashely, "Electron Microscopy of Thin Crystal", Butterworths, 1965.

[52] T. T. Sheng, in Analytical Techniques for Thin Film, eds. K. N. Tu, and R. Rosenberg, p.252, Academic Press, New York, 1988.

[53] J. C. Braoman and R. Sinclair, J. Electron Microscopy Tech. 1, 53 (1984).

[54] David R. Lide, CRC handbook of Chemistry and Physics, 79th ed., CRC Press, 1998-1999.

[55] O. E. Raichev, Phys. Rev. B 73 (2006), 195328.

[56] O. Groning, O. M. Kuttel, C. Rmmrnrggrt, P. Groning, and L. Schlapbach, J. Vac. Sci. Technol. B., 2000, 18, 665-678.

[57] Y. H. C. Cha, H. J. Doerr, and R. F. Bunsha, surf. coat. Tech. 62 (1-3), 697-701 (1993).

[58] J. Romanek, A. P. Kobzev, M. Kulik, T. Tsvetkova, and J. Zuk, Vacuum 70 (2003), 457-465.

[59] D. H. Chen, S. P. Wong, W. Y. Cheung, J. B. Xu, Solid State Commun. 128 (11): 435-439, Dec 2003.

[60] A. N. Obraztsov, O. Gröning, A. A. Zolotukhin, Al. A. Zakhidov and A. P. Volkov, Diam. Relat. Mater. 15 (4-8), 838-841, 2006.

[61] V. M. Anishchik, V. V. Uglov , A. K. Kuleshov, A. R. Filipp, D. P. Rusalsky, M. V. Astashynskaya, M. P. Samtsov, T. A. Kuznetsova, F. Thiery, and Y. Pauleau, Thin Solid Films, Vol. 482, 248-252, 2005.

[62] S. T. Tan, B. J. Chen, X. W. Sun, and W. J. Fan, J. Appl. Phys. 98, 013505 (2005).

[63] K. P. Loh, I. Sakaguchi, M. Nishitani-Gamo, et al., Diam. Relat. Mater. 8 (2-5): 781-784.1999.

[64] F. Ye, E. Q. Xie, X. J. Pan, H. Li, H. G. Duan, and C. W. Jia, J. Vac. Sci. Technol. B 24 (3), 1358-1361, 2006.

[65] H. Kiyota, M. Higashi, T. Kurosu, M. Iida, J. Appl. Phys. 99 (9), - May 2006.

[66] Y. Abdi, J. Koohshorkhi, S. Mohajerzadeh, S. Darbari, and Z. Sanaee, J. Vac. Sci. Technol. B 25 (3), 822-828, 2007.

A. Derivation of the F-N equation

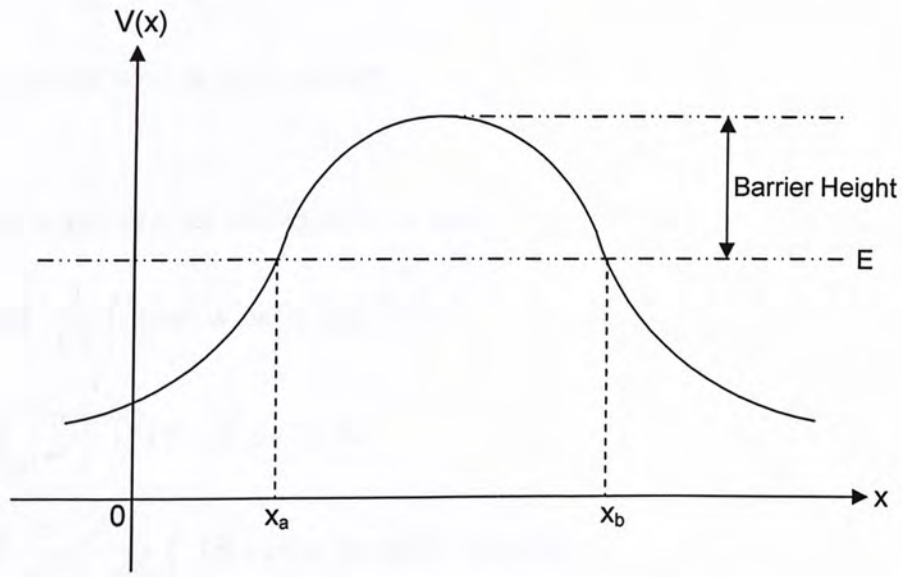

Figure A.1 A one-dimensional potential barrier

According to WKB approximation, the transmission coefficient T of a one dimensional potential barrier is [23],

$$T = \exp\left[-\frac{2}{h^*}\int_{x_a}^{x_b}\{2m[V(x)-E]\}^{\frac{1}{2}}dx\right] \qquad (1.1)$$

h* is the Dirac's constant

m is the free electron mass

V(x) is the potential energy seen by the electrons

E is the energy of the electrons

Consider the energy band diagram in field emission (Figure 1), the potential barrier is very closed to the emission surface, therefore, $x_a = 0$ and $x_b = x_2$. Moreover, $eF_0x_2 = W-E$, so $x_2 = W-E/eF_0$.

The potential energy V(x) equals to [24],

$$V(x)=\begin{cases}0 & x\le 0\\ W-eF_0x & x\ge 0\end{cases} \qquad (1.2)$$

F_0 is the applied electric field strength

Substitute equation (1.2) into equation (1.1),

$$T=\exp\left[-\frac{2}{h^*}\int_0^{x_2}\{2m[W-eF_0x-E]\}^{\frac{1}{2}}dx\right]$$

$$\ln T=-2\left(\frac{2m}{h^{*2}}\right)^{\frac{1}{2}}\int_0^{x_2}(W-eF_0x-E)^{\frac{1}{2}}dx$$

$$=-2\left(\frac{2m}{h^{*2}}\right)^{\frac{1}{2}}\frac{1}{eF_0}\int_0^{x_2}(W-eF_0x-E)^{\frac{1}{2}}d(W-eF_0x-E)$$

$$=-2\left(\frac{2m}{h^{*2}}\right)^{\frac{1}{2}}\frac{1}{eF_0}\frac{3}{2}\left[(W-eF_0x-E)^{\frac{3}{2}}\right]_0^{x_2}=\frac{W-E}{eF_0}$$

$$=-\frac{4}{3}\left(\frac{2m}{h^{*2}}\right)^{\frac{1}{2}}\frac{(W-E)^{\frac{3}{2}}}{eF_0}$$

$$T=\exp\left[-\frac{4}{3}\left(\frac{2m}{h^{*2}}\right)^{\frac{1}{2}}\frac{(W-E)^{\frac{3}{2}}}{eF_0}\right] \qquad (1.3)$$

This equation is known as Fowler Nordheim formula.

On the other hand, one of the assumptions in the F-N Model is that electron tunneling occurs at a constant energy E and those electrons are traveling in the x direction.

$$E=\frac{1}{2}m^*v^2=\frac{m^{*2}v_x^{\ 2}}{2m^*}=\frac{p_x}{2m^*} \qquad (1.4)$$

m^* is the effective electron mass in metal

The carrier density n in the momentum space is $(2/m^*h^3)dp_xdp_ydp_z$ and the current density is J = nqv where q is the electron charge and v is the velocity of the electron. Hence the tunneling current density during field emission is:

$$J = \frac{2e}{m^*h^3}\iiint p_x T(p_x)dp_x dp_y dp_z \qquad (1.5)$$

$T(p_x)$ is the transmission coefficient

The integration is carried out for all electrons in the conduction band. This requires,

$$p_x^2 + p_y^2 + p_z^2 \le p_0^2 \quad \text{and} \quad p_0^2 = 2m^*E_f$$

Therefore,

$$\iint dp_y dp_z = \pi(p_0^2 - p_x^2)$$

And the tunneling current density is,

$$J = \frac{2e\pi}{m^*h^3}\int_0^{p_0} T(p_x)p_x(p_0^2 - p_x^2)dp_x \qquad (1.6)$$

Let $\theta = p_0 - p_x$, then $T(p_0-\theta)$ decreases rapidly with increasing θ, therefore only contributions for small θ are significant. So we could write in good approximation such that,

$$p_0 \approx p_x$$
$$p_0^2 - p_x^2 = (p_0 + p_x)(p_0 - p_x) \approx 2p_0\theta \qquad (1.7)$$

$$(W-E)^{\frac{3}{2}} = (\Phi + \frac{p_0{}^2}{2m^*} - \frac{p_x{}^2}{2m^*})^{\frac{3}{2}} = \Phi^{\frac{3}{2}}\left(1+\frac{p_0{}^2 - p_x{}^2}{2m^*\Phi}\right)^{\frac{3}{2}}$$

$$= \Phi^{\frac{3}{2}}\left(1+\frac{p_0\theta}{m^*\Phi}\right)^{\frac{3}{2}}$$

$$\approx \Phi^{\frac{3}{2}} + \frac{3}{2}\frac{p_0\theta\Phi^{\frac{1}{2}}}{m^*} \qquad \because \frac{p_0\theta}{m^*\Phi} << 1$$

So we have,

$$(W-E)^{\frac{3}{2}} = \Phi^{\frac{3}{2}} + \frac{3}{2}\frac{p_0\theta\Phi^{\frac{1}{2}}}{m^*} \tag{1.8}$$

Substitute equation (1.7) and (1.8) into equation (1.6) and (1.3) respectively,

(1.7)+(1.6),

$$J = \frac{4e\pi}{m^*h^3}\int_0^{p_0} T(p_x)p_x p_0\theta dp_x \tag{1.9}$$

(1.8)+(1.3)

$$T = \exp\left[-\frac{4}{3}\left(\frac{2m}{h^{*2}}\right)^{\frac{1}{2}}\frac{\Phi^{\frac{3}{2}} + \frac{3}{2}\frac{p_0\theta\Phi^{\frac{1}{2}}}{m^*}}{eF_0}\right] \tag{1.10}$$

Combining equation (1.9) and (1.10) with $\theta = p_0 - p_x$ and $p_0 \approx p_x$,

$$J = \frac{4e\pi}{m^* h^3} \int_0^{p_0} \exp\left[-\frac{4}{3}\left(\frac{2m}{h^{*2}}\right)^{\frac{1}{2}} \frac{\Phi^{\frac{3}{2}} + \frac{3}{2}\frac{p_0\theta\Phi^{\frac{1}{2}}}{m^*}}{eF_0} \right] p_x p_0 \theta dp_x$$

$$= \frac{4e\pi}{m^* h^3} \int_0^{p_0} \exp\left[-\frac{4}{3}\left(\frac{2m}{h^{*2}}\right)^{\frac{1}{2}} \frac{\Phi^{\frac{3}{2}} + \frac{3}{2}\frac{p_0\theta\Phi^{\frac{1}{2}}}{m^*}}{eF_0} \right] p_0^{\,2} \theta d\theta$$

$$= \frac{4p_0^{\,2}e\pi}{m^* h^3} \exp\left[-\frac{4}{3}\left(\frac{2m}{h^{*2}}\right)^{\frac{1}{2}} \frac{\Phi^{\frac{3}{2}}}{eF_0} \right] \int_0^{p_0} \exp\left[-2\left(\frac{2m}{h^{*2}}\right)^{\frac{1}{2}} \frac{p_0\Phi^{\frac{1}{2}}}{m^* eF_0}\theta \right] \theta d\theta$$

Let $a = 2\left(\frac{2m}{h^{*2}}\right)^{\frac{1}{2}} \frac{p_0\Phi^{\frac{1}{2}}}{m^* eF_0}$, then

$$J = \frac{4p_0^{\,2}e\pi}{m^* h^3} \exp\left[-\frac{4}{3}\left(\frac{2m}{h^{*2}}\right)^{\frac{1}{2}} \frac{\Phi^{\frac{3}{2}}}{eF_0} \right] \int_0^{p_0} \theta \exp(-a\theta) d\theta$$

Since $T(p_0-\theta)$ decreases rapidly with increasing θ, the upper limit p_0 of the above integral could be extended to infinity and by the standard formula of definite integral,

$$\int_0^{\infty} \theta \exp(-a\theta) d\theta = \frac{1}{a^2} \qquad (1.11)$$

So we have,

$$J = \left[\frac{\frac{4p_0^{\,2}e\pi}{m^* h^3}}{4\left(\frac{2m}{h^{*2}}\right)\frac{p_0^{\,2}\Phi}{m^{*2} e^2 F_0^{\,2}}} \right] \exp\left[-\frac{4}{3}\left(\frac{2m}{h^{*2}}\right)^{\frac{1}{2}} \frac{\Phi^{\frac{3}{2}}}{eF_0} \right]$$

$$J = \frac{m^*}{m} \frac{e^3 F_0^{\,2}}{\pi 8 h \Phi} \exp\left[-\frac{4}{3}\left(\frac{2m}{h^{*2}}\right)^{\frac{1}{2}} \frac{\Phi^{\frac{3}{2}}}{eF_0} \right] \qquad (1.12)$$

This is known as the Fowler Nordheim equation describing the field emission behavior.

However, one of the assumptions of the F-N model is that the emission surface is perfectly smooth but this is not the case in reality. The surface morphology is one of the factors which would affect the field emission performance. Therefore, a field enhancement factor β is introduced in the F-N equation such that $F_0 = \beta F$, where F_0 is the local field strength while F is the nominal field. Assuming the m* = m, the tunneling current density becomes,

$$J = \frac{e^3 \beta^2 F_0^{\ 2}}{\pi 8 h \Phi} \exp\left[-\frac{4}{3} \left(\frac{2m}{h^{*2}} \right)^{\frac{1}{2}} \frac{\Phi^{\frac{3}{2}}}{\beta F e} \right] \qquad (1.13)$$

And evaluate all the known values,

$$J = \frac{A \beta^2 F_0^{\ 2}}{\Phi} \exp\left[-B \frac{\Phi^{\frac{3}{2}}}{\beta F} \right] \qquad (1.14)$$

$A = 1.54 \times 10^{-6} A e V V^{-2}$

$B = 6.83 \times 10^{7} (eV)^{-3/2} cm^{-1}$

In order to have a clear picture on the field enhancement factor, equation (1.14) would be modified to,

$$\ln\left(\frac{J}{F^2} \right) = \ln\left(\frac{A \beta^2}{\Phi} \right) - B \frac{\Phi^{\frac{3}{2}}}{\beta} \bullet \frac{1}{F} \qquad (1.15)$$

The left hand side term $\ln(J/F^2)$ varies linearly with 1/F and by plotting this linear relationship, the field enhancement factor β could be obtained by calculating the slope of the graph which equals to,

$$\text{slope} = -B\frac{\Phi^{\frac{3}{2}}}{\beta}$$

On the other hand, the energy of electrons inside the metal is not constant but follows the Fermi-Dirac distribution [25].

$$\rho(E) = N_c \frac{2}{\sqrt{\pi}} F_{1/2}\left(\frac{E}{k_B T}\right) \tag{1.16}$$

N_c is the density of electron in conduction band

$F_{1/2}$ is the Fermi-Dirac Integral

k_B is the Boltzman's constant

T is the temperature

The image charge potential would become,

$$V(x) = \begin{cases} 0 & x \le 0 \\ E + \Phi - eF_0 x - \dfrac{e^2}{16\pi 6_0 x} & x \ge 0 \end{cases} \tag{1.17}$$

Then equation (1.11) would change to,

$$J(T,F) = \frac{m^* e^3}{2\pi^2 h^{*3} c_{FN}{}^2} \exp\left(-\frac{b_{FN}}{F}\right) \left[\frac{\pi}{\frac{1}{k_B T}\sin(k_B T c_{FN} \pi)}\right] \tag{1.18}$$

Where,

$$a_{FN}(F) = \frac{1}{16h^{*}\Phi\pi^{2}t(y)^{2}} \qquad b_{FN}(F) = \frac{4}{3h^{*}}\sqrt{2m^{*}\Phi^{3}}v(y)$$
$$c_{FN}(F) = \frac{2}{h^{*}F}\sqrt{2m^{*}\Phi^{3}}t(y) \qquad y^{2} = \frac{e^{2}F}{4\Phi^{2}\pi\varepsilon_{0}} \tag{1.19}$$

In the above equations, v(y) and t(y) are the Nordheim elliptic functions.

Moreover, the term in the square bracket in equation (1.18) is close to unity at room temperature. So,

$$J(F) = \frac{e^{3}}{16\pi^{2}h^{*}\Phi t(y)^{2}}\exp\left(-\frac{4}{3h^{*}}\sqrt{2m^{*}\Phi^{3}}v(y)\frac{1}{F}\right)$$

$$J(F) = a_{FN}F^{2}e^{3}\exp\left(-\frac{b_{FN}}{F}\right) \tag{1.20}$$

Since all the coefficients in equations (1.18) are either explicitly or implicitly related to the applied electric field, the linearity might lost in the *F-N* plot. One of the possible ways to recover the linearity is to linearize the v(y) in F and treat t(y) as a constant term. Another alternative way is assuming T = 0K and making the approximation suggested by Spindt, Brodile and the co-workers [26],

$t(y) \approx 1.1$

$v(y) \approx v_{0} - v_{1}y^{2} \approx 0.95 - y^{2}$

The approximation of the quadratic term v(y) is reasonable for the intermediate values of y. This method is useful and convenient in estimating the value of the $\beta/\Phi^{3/2}$ from the slope of the *F-N* plot. If a quadratic v(y) is used, the exponential term v_1 could be included into the a_{FN} term while the b_{FN} term could be redefined and exclude v_1. This would give an identical linear *F-N* plot.